University of Kentucky
UKnowledge

University of Kentucky Doctoral Dissertations | Graduate School

2008

A PRECISION INSTRUMENT FOR RESEARCH INTO NANOLITHOGRAPHIC TECHNIQUES USING FIELD-EMITTED ELECTRON BEAMS

King-Fu Hii
University of Kentucky, kfhii01@uky.edu
Click here to let us know how access to this document benefits you.

Recommended Citation

Hii, King-Fu, "A PRECISION INSTRUMENT FOR RESEARCH INTO NANOLITHOGRAPHIC TECHNIQUES USING FIELD-EMITTED ELECTRON BEAMS" (2008). *University of Kentucky Doctoral Dissertations*. 675.
https://uknowledge.uky.edu/gradschool_diss/675

This Dissertation is brought to you for free and open access by the Graduate School at UKnowledge. It has been accepted for inclusion in University of Kentucky Doctoral Dissertations by an authorized administrator of UKnowledge. For more information, please contact UKnowledge@lsv.uky.edu.

ABSTRACT OF DISSERTATION

King-Fu Hii

The Graduate School

University of Kentucky

2008

A PRECISION INSTRUMENT FOR RESEARCH INTO NANOLITHOGRAPHIC TECHNIQUES USING FIELD-EMITTED ELECTRON BEAMS

ABSTRACT OF DISSERTATION

A dissertation submitted in partial fulfillment of the
requirements for the degree of Doctor of Philosophy
in the College of Engineering at the University of Kentucky

By

King-Fu Hii

Lexington, Kentucky

Co-Directors: Dr. R. Ryan Vallance, Professor of Mechanical Engineering
and Dr. M. Pinar Menguc, Professor of Mechanical Engineering

Lexington, Kentucky

2008

Copyright © King-Fu Hii 2008

ABSTRACT OF DISSERTATION

A PRECISION INSTRUMENT FOR RESEARCH INTO NANOLITHOGRAPHIC TECHNIQUES USING FIELD-EMITTED ELECTRON BEAMS

Nanomanufacturing is an active research area in academia and industry due to the ever-growing demands for precision surface modifications of thin films or substrates with nanoscale features. Conventional lithographic techniques face many challenges as they approach their fundamental limits. Consequently, new nanomanufacturing tools, fabrication techniques, and precision instruments are being explored and developed to meet these challenges. It has been hypothesized that direct-write nanolithography might be achieved by using a field-emitted electron beam for nanomachining. This dissertation moves this research one step closer by developing a precision instrument that can enable the integration of direct-write nanolithography by a field-emitted electron beam with dimensional metrology by scanning tunneling microscopy. First, field emission from two prospective electron sources, a carbon nanotube field emitter and a sharp tungsten field emitter, is characterized at distances ranging from sub-micrometer to a few micrometers. Also, the design and construction of a low thermal drift piezoelectric linear motor is described for tip-sample approach. Experiments indicate that: the step size is highly repeatable with a standard deviation of less than 1.2 nm and the thermal stability is better than 40 nm/°C. Finally, the design and construction of the instrument are presented. Experiments indicate that: the instrument is operating properly in scanning tunneling microscope mode with a resolution of less than 2 Å.

KEYWORDS: Precision Instrument, Nanomachining, Nanolithography, Scanning Tunneling Microscope, Electron Field Emission

King-Fu Hii

December 18, 2008

A PRECISION INSTRUMENT FOR RESEARCH INTO NANOLITHOGRAPHIC TECHNIQUES USING FIELD-EMITTED ELECTRON BEAMS

By

King-Fu Hii

Dr. R. Ryan Vallance

Co-Director of Dissertation

Dr. M. Pinar Menguc

Co-Director of Dissertation

Dr. L. Scott Stephens

Director of Graduate Studies

December 18, 2008

RULES FOR THE USE OF DISSERTATIONS

Unpublished dissertations submitted for the Doctor's degree and deposited in the University of Kentucky Library are as a rule open for inspection, but are to be used only with due regard to the rights of the authors. Bibliographical references may be noted, but quotations or summaries of parts may be published only with the permission of the author, and with the usual scholarly acknowledgments.

Extensive copying or publication of the dissertation in whole or in part requires also the consent of the Dean of the Graduate School of the University of Kentucky.

DISSERTATION

King-Fu Hii

The Graduate School

University of Kentucky

2008

A PRECISION INSTRUMENT FOR RESEARCH INTO NANOLITHOGRAPHIC TECHNIQUES USING FIELD-EMITTED ELECTRON BEAMS

DISSERTATION

A dissertation submitted in partial fulfillment of the requirements of the degree of Doctor of Philosophy in the College of Engineering at the University of Kentucky

By

King-Fu Hii

Lexington, Kentucky

Co-Directors: Dr. R. Ryan Vallance, Professor of Mechanical Engineering
and Dr. M. Pinar Menguc, Professor of Mechanical Engineering

Lexington, Kentucky

Copyright © King-Fu Hii 2008

ACKNOWLEDGMENTS

I would like to sincerely thank Dr. R. Ryan Vallance at The George Washington University and Dr. M. Pinar Menguc at the University of Kentucky for all of their guidance and assistance of this research. Dr. Vallance taught me every important aspect of Precision Engineering, knowledge which provides me with all of the opportunities that I have today and I am forever grateful. He helped me throughout this research from a long distance and kept me motivated all the time. This dissertation would not have been possible without his help.

I would also like to thank my Ph.D. committee members Dr. L. S. Stephens and Dr. J. T. Hastings, and my outside examiner Dr. L. G. Hassebrook, for all their critical review of my work. Also, I would like to thank Dr. K. Ng and Mr. John Nichols from the Department of Physics at the University of Kentucky for their big help in testing my instrument.

Also, I would like to thank my colleagues and friends Dr. Basil T. Wong, Dr. Chris J. Morgan, Dr. P.-L. Ong, and Mr. T.-M. Yee for all their help and support. Finally, I would like to thank my parents, Y. S. Hii and S. P. Tu, and my brothers and sisters, their guidance and support were the best in the world that I could have ever asked for. Their strength and integrity inspired me.

Table of Contents

Acknowledgments iii

List of Tables vi

List of Figures vii

1 Introduction and Thesis Overview 1
- 1.1 Introduction . . . 1
- 1.2 Background to the Dissertation . . . 2
  - 1.2.1 Electron Beam Lithography . . . 2
  - 1.2.2 Threshold Heating and Emission from Nanotubes . . . 3
  - 1.2.3 Scanning Tunneling Microscopy . . . 4
  - 1.2.4 Scanning Tunneling Microscope Lithography . . . 5
  - 1.2.5 Carbon Nanotubes as An Electron Source . . . 8
- 1.3 Dissertation Overview . . . 9
  - 1.3.1 Hypothesis . . . 11
  - 1.3.2 Dissertation Contributions . . . 11
  - 1.3.3 Dissertation Contents Overview . . . 12

2 Field Emission Characterization 13
- 2.1 Introduction to the Chapter . . . 13
- 2.2 Theoretical Background . . . 14
  - 2.2.1 Electrons Inside Metals and the Work Function . . . 14
  - 2.2.2 Emission of Electrons . . . 15
  - 2.2.3 Emission Current Density: The General Case . . . 18
  - 2.2.4 Approximation of Current Density at Low Temperatures and High Fields . . . 21
- 2.3 Electric Field Enhancement and Emission Area . . . 23
  - 2.3.1 Generalized Fowler-Nordheim Equation . . . 23
  - 2.3.2 Electric Field Enhancement . . . 25
  - 2.3.3 Extraction of FN Parameters . . . 29
- 2.4 Preparation of Electrodes . . . 33
  - 2.4.1 Sharp Tungsten Field Emitter . . . 33
  - 2.4.2 Carbon Nanotube Field Emitter . . . 33
  - 2.4.3 Electron Collector . . . 38
- 2.5 Experimental Methods and Apparatus . . . 38

2.5.1 Ultra-High Vacuum Chamber 40
2.5.2 Apparatus and Instrumentation 41
2.5.3 Experimental Procedure 44
2.6 Characterizing Field Emission at Small Separation Distances 46
2.6.1 Carbon Nanotube Field Emitter 46
2.6.2 Sharp Tungsten Field Emitter 55
2.7 Chapter Summary 59

3 Piezoelectric Linear Motor as Coarse Positioner for Tip-Sample Approach 62
3.1 Introduction to the Chapter 62
3.2 Background 62
3.3 Design and Construction 65
3.4 Operation 71
3.5 Experimental Setup 81
3.6 Calibration of Actuators 83
3.7 Motion Characteristics 85
3.7.1 Axial Motion 85
3.7.2 Lateral Motion 95
3.8 Thermal Stability 99
3.9 Chapter Summary 103

4 Instrument for Nanolithographic Techniques Using Field-Emitted Electron Beams 104
4.1 Introduction to the Chapter 104
4.2 Piezoelectric Scanner 104
4.2.1 Tube Scanner Displacement 107
4.2.2 Tube Scanner Calibration 111
4.3 Design and Construction of Instrument 124
4.4 Vibration Isolation 134
4.5 Preliminary Test of Instrument in STM mode 139
4.6 Chapter Summary 151

5 Conclusions and Future Work 152
5.1 Conclusions 152
5.2 Future Work 154

Bibliography 156

Vita 177

List of Tables

1.1 Studies of field emission from an individual CNT or CNF at small distances 9

2.1 Numerical parameters β_v, α_t, and β_t for carbon nanotube and tungsten . 23

3.1 Parameters of belleville disc spring 70
3.2 Physical parameters of the piezoelectric linear motor 80
3.3 Expected and experimental threshold voltages for various preload forces 93

4.1 Specifications and dimensions of the piezoelectric tube scanner 113
4.2 The values of K_z^s, d_{31}^{zs}, α_z, and β_z, of the z scanner for a triangular waveform input at 2 Hz 116
4.3 Polynomial coefficients and calculated values of $K_{x_t}^s$, α_{x_t}, β_{x_t}, and d_{31}^{xs}, of the xy scanner in the x-direction for a triangular waveform input at various input frequencies 121
4.4 Polynomial coefficients and calculated values of $K_{y_t}^s$, α_{y_t}, β_{y_t}, and d_{31}^{ys}, of the xy scanner in the y-direction for a triangular waveform input at various input frequencies 122
4.5 Physical parameters of the instrument's eddy current damper 128
4.6 Dimensional parameters and coefficients of thermal expansion (CTE) . . 133

List of Figures

1.1 Conceptual illustration of nanomachining process by threshold heating and emission from nanotubes (THEN). 3

1.2 Schematic of scanning tunneling microscope (STM). 4

1.3 Material removal by low-energy electron stimulated reaction and thermal desorption (LEESR/TD): (a) schematic of decomposition of SiO_2 layer by an STM tip and (b) concentric ring pattern SiO_2/Si fabricated using STM tip by LEESR/TD process [19]. 6

1.4 Holes created on a thin silver (Ag) film: (a) at room temperature with an electron-beam of 120 eV and 1 μA for 100 s, and (b) at 400 řC with an electron-beam of 100 eV and 716 nA for 60 s (at the center of the ellipse) [18]. 7

1.5 Schematic of techniques for direct-write nanolithography by a field-emitted electron beam with dimensional metrology by scanning tunneling microscopy: (a) scan sample surface before writing in STM mode, (b) write or pattern using a field-emitted electron beam in field emission mode, and (c) scan sample surface after writing in STM mode. 10

2.1 Potential energy (in eV) of an electron near a metal surface. A work function of ϕ = 4.5 eV is assumed. $x_2 - x_1$ represents the local barrier width encountered by a tunneling electron. 17

2.2 Field amplification factors computed by finite element analysis for a hemisphere on post with tip radius $r = 10$ nm and height $h = 1$ μm and fit with the modified Miller equation. 28

2.3 Comparison of empirical models for field enhancement factor γ and field amplification factor λ as a function of separation distance s for an emitter with a tip radius r = 10 nm and height h = 2 μm. 30

2.4 Comparison of approximate forms with exact solutions for the Fowler-Nordheim field emission functions $v(y)$ and $t^2(y)$ for ϕ = 4.5 eV. 32

2.5 Electrochemical etching apparatus for preparing sharp tungsten tips [80]. 34

2.6 Time progression of electrochemical etching process of a tungsten wire [80]. 34

2.7 Sample images of sharp tungsten field emitters. 35

2.8 Procedures for attaching a carbon nanotube (CNT) to a tungsten tip. (a) A CNT protruding from a thin substrate containing many CNTs is selected and (b) is aligned and attached to a tungsten tip, and (c) the CNT is broken by Joule heating after flowing an electrical current through it. . . . 36

2.9 Apparatus for preparing carbon nanotube (CNT) field emitters. 37
2.10 A measurement of the electrical current that flows through a CNT as a function of applied voltage during the cutting process. 37
2.11 Sample images of CNT field emitters. 39
2.12 Sample images of anode. 39
2.13 Photograph of the ultra-high vacuum chamber system for experimental studies. 40
2.14 Apparatus and instrumentation for field emission measurement at small anode-cathode distances. 42
2.15 Photograph of the experimental setup inside the UHV chamber used for field emission experiments. 43
2.16 Displacement of the nanopositioning stage as a function of the applied voltage to the piezoelectric (PZT) actuator. 43
2.17 Surface detection for establishing datum and initial separation displacement of electrodes (home position). 45
2.18 $I(V)$ characteristics of the CNT field emitter shown in Fig. 2.11(b) at five separation distances. Solid lines are Fowler-Nordheim (FN) fits. 47
2.19 FN plots of the $I(V)$ curves shown in Fig. 2.18. 48
2.20 Turn-on voltage as function of separation distance. 49
2.21 Turn-on field as function of separation distance. 50
2.22 Field amplification factor as function of separation distance. 51
2.23 Current density versus local electric field at the tip of the carbon nanotube. 54
2.24 $I(V)$ characteristics of the sharp tungsten emitter shown in Fig. 2.7(c) at eleven separation distances s = 0.13, 0.65, 1.17, 1.70, 2.22, 2.74, 3.26, 3.79, 4.31, 4.83, and 5.35 μm.. Solid lines are Fowler-Nordheim (FN) fits. 56
2.25 Turn-on voltage as function of separation distance. 57
2.26 Turn-on field as function of separation distance. 58
2.27 Field amplification factor as function of separation distance. 59
2.28 Axisymmetric model of the sharp tungsten emitter (cathode) and the metal coated fiber (anode). 60

3.1 Common approaches for using small displacement of piezoelectric actuators to achieve long travel ranges, (a) stick-slip motion, (b) wormlike motion, and (c) walking motion. 64
3.2 (a) Section cut-away view of piezoelectric linear motor and (b) driving mechanism. 66
3.3 Schematic diagram of preload mechanism with lever reduction. 69
3.4 Preload force P generated by the disc spring for an adjustment of δ_s at one of the screws. 70
3.5 Photograph of the piezoelectric linear motor. 72
3.6 Block diagram of electronic circuit for the linear motor. 73
3.7 Circuit diagram of the triangular waveform generator and the voltage clipper. 73
3.8 Circuit diagram of Block A. 74
3.9 Circuit diagram of Block B and triacs. 76

3.10 Schematic diagram of the bidirectional electronic switch and waveform shaping. 77
3.11 (a) Six synchronized waveforms used to move the alumina prism one step forward and (b) order of piezoelectric actuators. 78
3.12 A simplified spring-mass model of the linear motor. 79
3.13 Arrangements for measuring the motion(s) in the (a) axial direction, (b) lateral directions, and (c) both axial and lateral directions. Photographs of experimental setups for (d) axial motion measurement and (e) axial and lateral motion measurements. 82
3.14 Photograph of the experimental setup for measuring the static holding force of the motor. 83
3.15 (a) Displacement of the actuactors versus applied voltage and (b) piezoelectric coefficient d_{15} versus applied voltage. 85
3.16 Motion characteristics of the motor for a 10 Hz square-wave input signal. The darker lines are the filtered data. (a) 5 nm stroke with cutoff at 500 Hz, (b) 2 nm stroke with cutoff at 275 Hz, and (c) 1 nm stroke with cutoff at 250 Hz. 86
3.17 Hysteresis loops of the motor for a 10 Hz sinusoidal input with voltage sweeps of 40 V, 80 V, 120 V, 160 V, and 200 V. 87
3.18 An example of the axial motion of the linear motor in the stepping mode. Step motions in the (a) forward and (b) backward directions. The preload force applied on the alumina prism is 24.5 N and the applied voltage is 196 V for both directions. 88
3.19 (a) Step Motion and (b) determination of step size. 89
3.20 Step motions for various applied voltages. 90
3.21 Voltage dependent mean step size of various preload forces for all three orientations of the piezoelectric linear motor. 92
3.22 Probability plot of step size variation for applied voltage and preload force of 100 V and 8.7 N, respectively. 93
3.23 Mean step size versus standard deviation for preload force of 8.7 N. . . . 94
3.24 Linearity of the motor in the forward (arrow pointed to the right) and backward (arrow pointed to the left) directions for a mean step size of about 100 nm under various preload conditions. 95
3.25 Lateral motions for preload force of 15 N (a) X direction (b) Y direction. The dots and solid lines are the lateral motions for voltage steps of 60 V and 196 V, respectively. 96
3.26 Lateral motions for preload force of 28 N (a) X direction (b) Y direction. The dots and solid lines are the lateral motions for voltage steps of 90 V and 196 V, respectively. 97
3.27 Lateral motions in the (a) X direction and (b) Y direction due to reversal in the (c) stepping direction. The darker lines are the filtered data with a cutoff frequency of 58 Hz. 98
3.28 Experimental setup for measuring thermal stability in the X direction. . . 100
3.29 Schematic for thermal stability measurement in the X direction. 100
3.30 Cancellation technique for determining the thermal drift. 101

3.31 Short-term thermal stability of the motor in the X direction over a period of 20 minutes. . . . 102
3.32 Long-term thermal stability of the motor in the X direction over a period of 26 hours. . . . 103

4.1 (a) A single piezoelectric tube for axial motion and (b) A single piezoelectric tube for lateral motions (x, y). . . . 108
4.2 Generation of the lateral displacement in the x direction by bending within a piezoelectric tube scanner. . . . 109
4.3 Piezoelectric tube scanner used in the instrument. (a) Directional assignment of the outer electrodes and (b) Photograph of the tube scanner. 113
4.4 Experimental setup for measuring the displacements of the piezoelectric tube scanner in the (a) axial z-direction, (b) lateral x-direction, and (c) lateral y-direction. . . . 114
4.5 Displacement (forward hysteresis curve) of the z scanner for a triangular waveform input at 2 Hz. . . . 116
4.6 Nonlinearity correction with a preshaped waveform: (a) without correction, (b) with correction, and (c) residual plots. . . . 118
4.7 Hysteresis curves of the xy scanner in the x-direction for a triangular waveform input at various input frequencies. . . . 120
4.8 Lateral displacement (forward hysteresis curve) of the xy scanner in the x-direction for a triangular waveform input at various input frequencies. . 121
4.9 Residual plot of the lateral displacement (forward hysteresis curve) of the xy scanner in the x-direction for a triangular waveform input at 5 Hz. . . 122
4.10 Hysteresis curves of the xy scanner in the y-direction for a triangular waveform input at various input frequencies. . . . 123
4.11 Lateral displacement (forward hysteresis curve) of the xy scanner in the y-direction for a triangular waveform input at various input frequencies. . 123
4.12 Assembly of the entire system. . . . 125
4.13 Single-stage vibration isolation with eddy current damping. . . . 126
4.14 Floated (springs suspended) stage assembly. . . . 127
4.15 Loadable instrument assembly. . . . 127
4.16 Assembly of the instrument: (a) exploded view, (b) exploded view with the piezoelectric tube scanner assembly mounted, and (c) unexploded of the instrument assembly. . . . 130
4.17 Photograph of the instrument assembly with tip or field emitter mounted but without the sample holder. . . . 131
4.18 Axial thermal stability of the instrument using a compensating structure. . 132
4.19 Bending mode of the piezoelectric tube scanner assembly. . . . 133
4.20 Model of the instrument in STM mode: (a) axial (z) direction and (b) lateral (x, y) directions. The system has been reduced to a simple damped harmonic oscillator. . . . 134
4.21 Frequency response of the instrument to external mechanical vibrations. 136

4.22 Model of a single-stage vibration isolation system. The vibration isolation system shown in Fig. 4.13 can be represented by (a) a translation system and (b) a pendulum system. 137
4.23 Vibration attennuation of the instrument combined with a single-stage vibration isolation system. 139
4.24 A photograph of a commercial universal SPM controller from RHK Technology. 140
4.25 Block diagram of STM feedback control system. 141
4.26 Feedback oscillation in the tunneling current due to improper gain and time constant settings at 1.3 and 6 ms, respectively. 142
4.27 STM images of the HOPG surface for a scan area of about 500 x 500 nm^2. (a) Image recorded while scanning the tungsten tip to the right ($+x$ direction), (b) image recorded while scanning the tungsten tip to the left ($-x$ direction), (c) the corresponding three-dimensional image of the image in (a), and (d) the corresponding three-dimensional image of the image in (b). 144
4.28 STM images of the HOPG surface for a smaller scan area of about 250 x 250 nm^2. (a) Image recorded while scanning the tungsten tip to the right ($+x$ direction), (b) image recorded while scanning the tungsten tip to the left ($-x$ direction), (c) the corresponding three-dimensional image of the image in (a), and (d) the corresponding three-dimensional image of the image in (b). 145
4.29 Surface corrugation (profile) between point A and point B of the HOPG surface (refer to Fig. 4.28(b)). 146
4.30 STM images of the holography grating surface for a scan area of about 260 x 260 nm^2. (a) Image recorded while scanning the tungsten tip to the right ($+x$ direction), (b) image recorded while scanning the tungsten tip to the left ($-x$ direction), (c) the corresponding three-dimensional image of the image in (a), and (d) the corresponding three-dimensional image of the image in (b). 148
4.31 STM images of the holography grating surface for a scan area of about 660 x 660 nm^2. (a) Image recorded while scanning the tungsten tip to the right ($+x$ direction), (b) image recorded while scanning the tungsten tip to the left ($-x$ direction), (c) the corresponding three-dimensional image of the image in (a), and (d) the corresponding three-dimensional image of the image in (b). 149
4.32 STM images of the holography grating surface for a scan area of about 2.09 x 2.09 μm^2. (a) Image recorded while scanning the tungsten tip to the right ($+x$ direction), (b) image recorded while scanning the tungsten tip to the left ($-x$ direction), (c) the corresponding three-dimensional image of the image in (a), and (d) the corresponding three-dimensional image of the image in (b). 150
4.33 Profiles of the grating surface (refer to Fig. 4.32(a)). 151

Chapter 1

Introduction and Thesis Overview

1.1 Introduction

Nanomanufacturing has become a very active research area in academia and in industry. The current demands, and perhaps more to come, require the precise modification of surfaces or thin films to create holes, lines, circles, arrays, and etc., that can be used in a diverse number of applications such as nanoelectronics and nanodevices [1]. To meet such a challenge and the demand of constantly and continuously shrinking devices, manufacturing tools and techniques will have to evolve. Thus, the ability to pattern at the nanoscale is the main driver behind the development of new nanomanufacturing tools, precision instruments, and fabrication techniques.

Nanofabrication techniques are constantly being explored and developed using precision instruments to build structures with nanoscale features, which can be used as components, devices, or systems in massive quantities and at potentially low costs. Nanoscale features in general refer to any physical characteristic that is between 0.1 and 100 nm in size. Most current technologies used in industry for nanofabrication have evolved from conventional lithographic processes such as photolithography, which were developed for the semiconductor industry to make microelectronic devices. These conventional lithographic techniques face many challenges as they approach their fundamental limits. Fabrication strategies are therefore required to secure cost-efficiency and technical feasibility.

1.2 Background to the Dissertation

1.2.1 Electron Beam Lithography

Electron beam lithography (EBL) is an established technology that has existed for more than twenty years. It is a promising technology to meet the challenge of continuously shrinking devices and it is commonly used to fabricate nanostructures. Many textbooks give extensive details of EBL [2, 3], but a brief review is given here. EBL works by scanning a high-energy electron beam in a patterned fashion across a surface covered with a film of electron-sensitive material (electron-beam resist). The resist is later developed using chemical etching in solvents to produce a 2D pattern on the surface by selectively removing either the exposed or non-exposed regions of the resist.

Electron-beam resists are usually polymers and they are classified into two groups, positive tone and negative tone electron-beam resists. For positive tone resists, the regions exposed to the electron beam become soluble to solvents. Whereas, for negative tone resists, the regions exposed to the electron beam become insoluble to solvents. Polymethyl methacrylate (PMMA) is an example of a positive tone resist and its solvent is typically MIBK:IPA developer (MIBK is methyl isobutyl ketone and IPA is isopropyl alcohol).

Dedicated electron-beam patterning systems such as EBL systems used in commercial applications are very expensive. It is also common to convert a scanning electron microscope (SEM) into an EBL system using relatively low-cost accessories [3]. Feature resolution is not limited by the beam spot size, which is as small as 5 nm, but by the scattering of electrons and secondary electrons within the electron-beam resist [3]. Since the EBL is a serial process, it takes a long time to expose a given 2D pattern, especially when writing dense patterns over large areas. Low throughput is the key limitation of EBL when compared to parallel techniques like photolithography. Therefore, EBL is not suitable for high-volume manufacturing, and it is typically reserved for the production of masks or in producing low-quantity of nanostructures for research purposes.

The primary advantage of EBL is that electrons have a wavelength that is on the

order of the atomic distance or smaller (e.i., wavelength of electrons equals to 8 pm at 25 keV [3]) and it is one of the ways to overcome the diffraction limit of light, which causes a limit on the minimum feature size that can be produced by photolithography. EBL has found a diverse number of usages in mask-making for photolithography, low-volume production of semiconductor components, and research and development.

1.2.2 Threshold Heating and Emission from Nanotubes

A few years ago, Vallance *et al.* [4] envisioned a new nanomachining process called Threshold Heating and Emission from Nanotubes (THEN). A conceptual illustration of the THEN process is shown in Fig. 1.1.

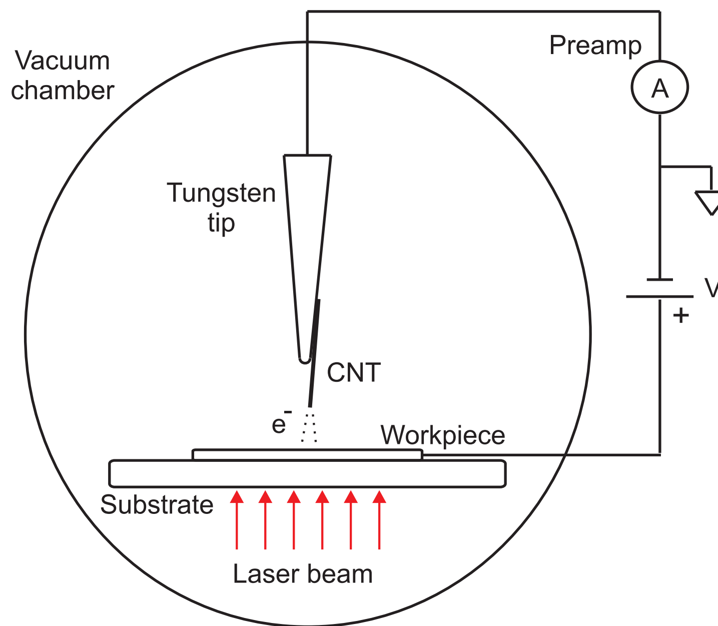

Figure 1.1: Conceptual illustration of nanomachining process by threshold heating and emission from nanotubes (THEN).

The THEN process is a hybrid process that utilizes two sources of energy to remove clusters of atoms from workpiece surfaces. The process requires laser heating, resistive heating, or radiative heating to raise the temperature of the workpiece to near an evaporative threshold temperature, and then field-emitted electrons from a carbon nan-

otube (CNT) can provide the additional energy necessary to locally evaporate atoms from the workpiece surface. Considerable research in the modeling of this process has been done by Wong and Menguc [5]. Computational simulations by Wong *et al*. [6] and Sanchez *et al*. [7] suggest the feasibility of nanomachining by this process.

1.2.3 Scanning Tunneling Microscopy

The first scanning tunneling microscope (STM) was invented in 1981 by Binnig *et al*. [8]. As illustrated in Fig. 4.1, an STM uses a sharp conducting tip with a bias voltage applied between the tip and the sample. Sharp metallic tips such as tungsten tips are usually prepared by electrochemical etching. When the tip is within the tunneling range of the sample, typically on the order of a few angstroms or up to 1 nm [9], electrons can tunnel through the gap from the tip to the sample or vice versa, depending on the sign of the bias voltage.

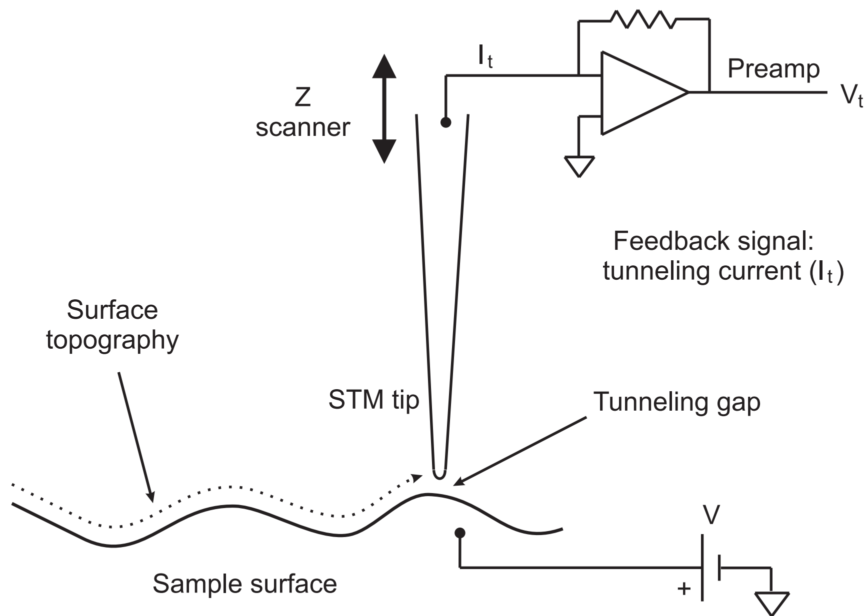

Figure 1.2: Schematic of scanning tunneling microscope (STM).

The proximity of the tip and the sample, combined with the exponential dependence of the tunneling current on the gap distance [10, 11, 12, 13] gives STMs remarkable

sensitivity with sub-angstrom resolution vertically and sub-nanometer resolution laterally. Two modes of operation are used in STM, namely constant-height and constant-current modes. In the constant-height mode, the STM tip moves in a horizontal plane (x, y) above the sample surface. And, the induced tunneling current constitutes the STM image, commonly known as a current image, which depends on the topography and the local surface electronic properties. This mode is applicable only for atomically flat surfaces, and it gives the ultimate resolution for an STM.

In the constant-current mode, the tip height is adjusted by feedback with a signal applied to the vertical (z) scanner to maintain the tunneling current constant during lateral (x, y) scanning, and the variation in the tip height produces an STM image that represents the topography of the sample surface. STM is a very powerful tool that has a diverse number of applications in many fields. One can find many textbooks today that give extensive overviews of the details of STM [9, 14, 15].

In addition to its well-known capabilities in atomic imaging and spectroscopy [9], STM has recently shown potential as a lithographic tool for nanoscale patterning of material structures. Scanning tunneling microscope lithography (STML) is one of the scanning probe microscopy (SPM)-based technologies, and another is the atomic force microscope lithography (AFML), which has become increasingly popular in the fabrication of nanoscale structures due to its low cost and great technical potential. A comprehensive review of the nanofabrication by SPM-based lithography was given by Tseng *et al.* [16], and here, only the most relavant aspects of STML are summarized in the following section.

1.2.4 Scanning Tunneling Microscope Lithography

The application of an STM for nanoscale lithography involves direct writing on resists or substrates, with or without chemical reactions, which result in material modification (resist exposure and oxidation), material deposition, material removal, and manipulation of materials. Of these, only material removal and material modification by resist exposure are discussed here.

In resist exposure, the current, voltage, and writing speed of the electron-beam are

typically on the order of 1 nA, 20 V, and 1 μm/s, respectively. The resist exposure process is similar to EBL except that the tunneling current of STM is used as a miniature electron beam. As in EBL, the latter process involves resist pattern development, which is suitable for pattern transfer by the liftoff approach or the subsequent etching and deposition processes [16]. By using STM to pattern a 20 nm thick PMMA resist, followed by subsequent deposition or etching process, McCord and Pease [17] have demonstrated that a 22 nm wide and 12 nm thick gold-palladium (Au-Pd) line on a Si substrate can be obtained with an electron-beam of 20 eV in energy and 100 pA in current at a writing speed of 1 μm/s.

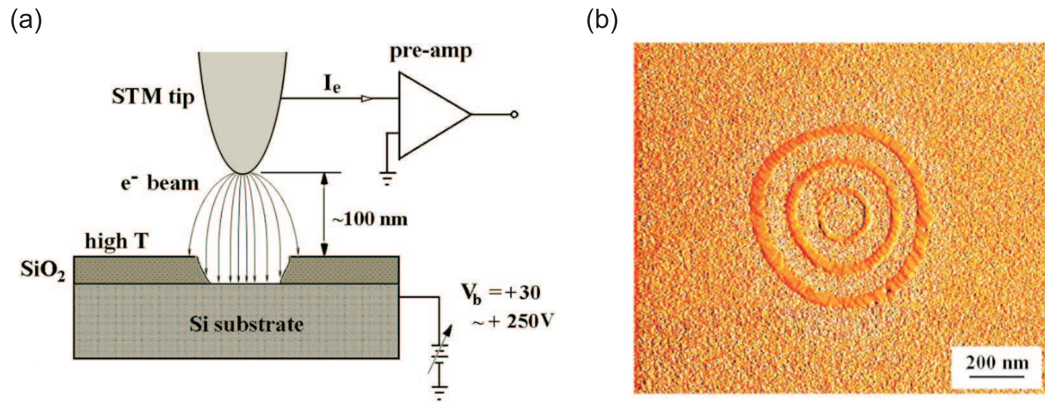

Figure 1.3: Material removal by low-energy electron stimulated reaction and thermal desorption (LEESR/TD): (a) schematic of decomposition of SiO_2 layer by an STM tip and (b) concentric ring pattern SiO_2/Si fabricated using STM tip by LEESR/TD process [19].

In material removal, nanoscale size features can be achieved by low-energy electron stimulated reaction and thermal desorption (LEESR/TD). Li *et al*. [18] and Iwasaki *et al*. [19] demonstrated that thin silicon oxide (SiO_2) layers with thicknesses of 1 nm up to a few nanometers on a silicon (Si) substrate can be selectively removed with a field-emitted electron beam of 10 to 250 eV and up to 1 μA of current extracted from the STM tip. This induces desorption of SiO_2 at temperatures between 300 and 700 $^\circ$C under UHV conditions. The oxide layer is removed by the electron-beam induced decomposition of SiO_2 at elevated temperatures into a gaseous SiO, which is

desorbed/evaporated from the Si substrate surface without consuming the substrate Si atoms. A commercial ultra-high vacuum (UHV) STM system (JEOL JSTM-4600X) was used, and the schematic of the STML LEESR/TD process is shown in Fig. 1.3(a) [19].

As illustared in Fig. 1.3(b) [18], a concentric-ring pattern SiO_2/Si was obtained by moving the STM tip positioned about 100 nm above the surface, in circle at a speed of 28 μm/s with an electron-beam of 85 eV and 12 nA of current with the substrate temperature kept at 650 $^{\circ}$C. The linewidth of these rings, shown in Fig. 1.3(b), is typically less than 50 nm, and the applied line doses from the inner ring to outer ring are 3.8, 4.3, and 4.8 $\times$ 10^{-3} C/cm, respectively [18].

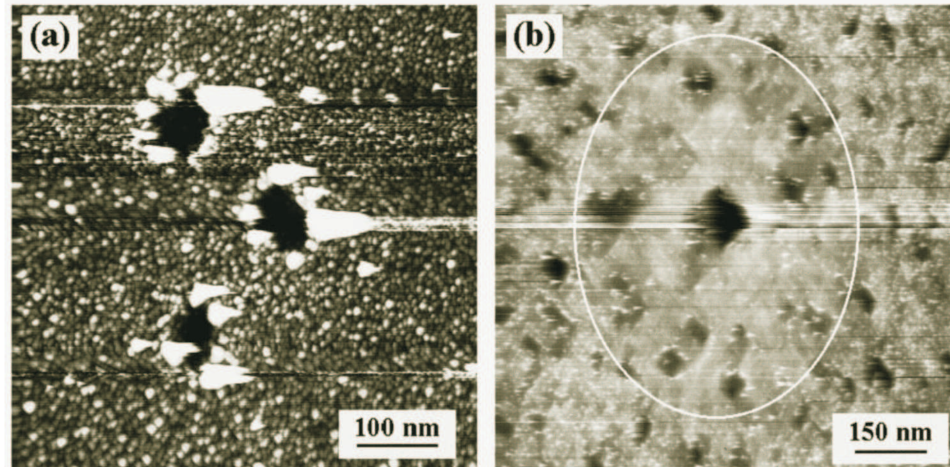

Figure 1.4: Holes created on a thin silver (Ag) film: (a) at room temperature with an electron-beam of 120 eV and 1 μA for 100 s, and (b) at 400 řC with an electron-beam of 100 eV and 716 nA for 60 s (at the center of the ellipse) [18].

Direct material removal from a thin metallic layer deposited on a silicon or glass substrate can also be achieved with a similar technique. As depicted in Fig. 1.4(a) [18], holes of 50 to 80 nm in diameter were created in an 8 nm thick silver (Ag) film on a silicon substrate at room temperature using an electron-beam of 120 eV and 1 μA of current for an exposure time of 100 seconds. With the silicon substrate temperature elevated to 400°C and using an electron-beam of 100 eV and 716 nA of current for an exposure time of a minute, a similar result can be achieved as shown in Fig. 1.4(b)

[18]. The same technique was used to form nanopits on a silicon substrate [20, 21], however, the exact mechanism of material removal is not fully understood.

1.2.5 Carbon Nanotubes as An Electron Source

Soon after the discovery of carbon nanotubes (CNTs) [22], substantial interest in the use of CNTs as electron sources [23] was stimulated by the earliest reports of their exceptional electron field emission behavior [24, 25], which results from their high aspect ratio, conductivity, and inertness. CNTs are grown as either single-walled nanotubes (SWNTs) or as multi-walled nanotubes (MWNTs), depending on their growth process [26]. Metallic or semiconductor SWNTs exist, but MWNTs are always metallic [27]. A SWNT can have a diameter range from 1 nm to a few nanometers and its length can be up to several micrometers, whereas a MWNT can have a diameter range from 5 nm to 100 nm and can be several micrometers long [27].

Many researchers have studied field emission from a multitude of CNTs in films [28, 29] or patterned arrays [30], microelectrodes with many CNTs [31], and CNT-based microcathodes [32]. These studies are of interest for applications like field emission display devices [33, 34] and parallel electron-beam lithography [32]. However, fewer studies were conducted on field emission from an individual CNT, which is more relevant to this work. Techniques previously used to study electron emission from individual nanotubes include the measurement of $I(V)$ curves [35, 36, 37], measurement of electron energy distribution [38, 39], field emission microscopy [40, 41], in-situ studies within a transmission electron microscope [42], and roaming anode techniques [43, 44, 45, 46]. Based on the studies of field emission conducted at distances greater than 1 mm, the maximum emission current recorded from an individual CNT is 0.1 mA (unusually high) prior to failure [35], the half-opening angle of an electron beam ranges from 6° up to 11°, and the full width at half maximum (FWHM) energy width of energy distribution ranges from 0.11 eV up to 0.40 eV.

There are even fewer studies of field emission from an individual CNT at separation distances less than 50 μm. Table 1.1 summarizes the studies of electron field emission from an individual CNT or a carbon nanofiber (CNF) at small distances based on all

available data. Of these studies, only Minh *et al*. [37], Bonard *et al*. [44], and *Sim et al*. [47] reported $I(V)$ curves for multiple distances. Minh *et al*. [37] measured $I(V)$ curves for an individual CNT on a silicon tip. Bonard *et al*. [44] and Sim *et al*. [47] used a roaming anode technique within a scanning electron microscopy (SEM) to measure $I(V)$ curves from an individual CNT protruding from a film of CNTs and an individual CNF protruding from a Kapton polyimide foil, respectively.

Table 1.1: Studies of field emission from an individual CNT or CNF at small distances

Distance (μm)	Field enhancement factor	Turn-on voltage^a (V)	Geometry r = radius (nm) l = length (μm)	Reference
0.06-5	230-460	47-185	$r = 17$, $l = 3.2$	[44]
0.12	4.8^b	90^b	$r = 50$, $l = 1.3^b$	[42]
0.1	90-380	20-30^b	$r = 50$, $l = 6$-30	[46]
10	208	270	$r = 24$, $l = 5.83$	[43]
10-50	500-750^b	60-260^b	$r = 15$-20, $l = 0.5$	[37]
20	200-500^b	150-400^b	$r = 20$, $l = 1.5$	[45]
0.02-5.5	5-360	22-100	$r = 8$, $l = 1$	[47]

^{a}1 nA ^{b}estimated

1.3 Dissertation Overview

In considering this recent research, an instrument that is capable of integrating direct patterning and imaging is ideal for research into nanolithographic techniques using field-emitted electron beams. Figure 1.5 illustrates the schematic of techniques in using such an instrument for direct-write nanolithography by a field-emitted electron beam with dimensional metrology by scanning tunneling microscopy. The instrument can be operated in at least modes: (1) scan sample surface in STM mode, and (2) write or pattern using a field-emitted electron beam in field emission mode.

As a strategy, this work is divided into two major tasks: (a) characterize the field emission at small distances using current-voltage $I(V)$ measurements for two potential candidates, a CNT field emitter and an ultra-sharp tungsten field emitter, as the electron source, and (b) design, fabricate, and test the key components of the instrument with

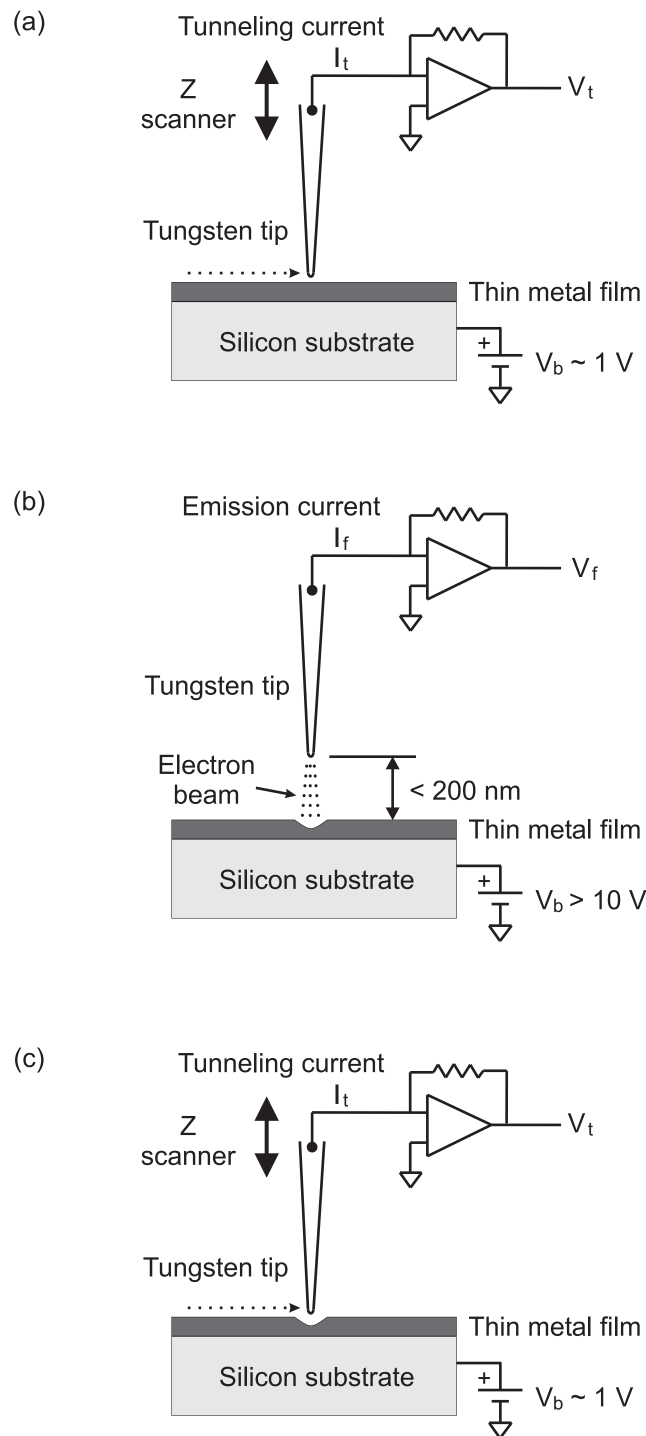

Figure 1.5: Schematic of techniques for direct-write nanolithography by a field-emitted electron beam with dimensional metrology by scanning tunneling microscopy: (a) scan sample surface before writing in STM mode, (b) write or pattern using a field-emitted electron beam in field emission mode, and (c) scan sample surface after writing in STM mode.

UHV compatibility for direct-write nanolithography by a field-emitted electron beam with dimensional metrology by scanning tunneling microscopy.

This instrument is not only for research into nanolithographic techniques using field-emitted electron beams, but also for providing experimental results in the near future that can be used for verifying computational and simulation works [6, 7]. In addition, the instrument can also be used for charaterizing field emission of various field emitters from extremely small distances to distances of a few milimeters.

1.3.1 Hypothesis

The hypothesis of this dissertation is that a new precision instrument can enable the integration of direct-write nanolithography by a field-emitted electron beam with dimensional metrology by scanning tunneling microscopy.

1.3.2 Dissertation Contributions

In proving this hypothesis, this dissertation made the following contributions:

1. a technique was developed for characterizing the field emission from one-dimensional (1D) nanostructures at small separation distances;

2. a new least-squares method was developed for extracting the Fowler-Nordheim (FN) parameters that is an improvement over conventional extraction using slope and ordinate intercepts on FN plots;

3. the design of a translational piezoelectric linear motor that has a low thermal drift using symmetrical design and low coefficients of thermal expansion materials;

4. experimental studies of the motion characteristics and the thermal stability of the piezoelectric linear motor; and

5. a simple method for improving the linearity of piezoelectric actuators using the preshaping of driving signals or waveforms.

1.3.3 Dissertation Contents Overview

This dissertation is organized into five chapters. Chapter 2 begins with an overview of the electron emission theory, and various electric field enhancement models are compared. A new method for extracting the Fowler-Nordheim (FN) parameters rather than the conventional extraction using slope and ordinate intercepts on the FN plots is presented and implemented. The preparation of electrodes and experimental systems are described. This chapter also introduces a technique for characterizing the field emission from one-dimensional (1D) nanostructures as a function of voltage and separation distance at small distances. Two types of emitters were used to demonstrate this technique, a CNT field emitter and an ultra-sharp tungsten field emitter.

Chapter 3 presents the design and operation of a translational piezoelectric linear motor, one of the key components of the new instrument for tip-sample approach. Specific attention is given to experimental studies of the motion characteristics and the thermal stability of the linear piezoelectric motor. A new method for measuring the motion characteristics and thermal stability of the motor is presented and implemented.

Chapter 4 focuses on the component (three-dimensional piezoelectric scanner) of the instrument that provides the fine motions of the tip, the vibration isolation of the instrument, and the instrument as a whole, with preliminary tests of the instrument in the STM-mode. A simple method for improving the linearity of the three-dimensional piezoelectric scanner is described and presented.

Chapter 5 concludes the dissertation with a summary and suggests topics for future work.

Chapter 2

Field Emission Characterization

2.1 Introduction to the Chapter

In order to use field-emitted electron beams for possible nanomanufacturing processes as described in the previous chapter, field emission must be studied at small electrode separation distances. Electrons are charged particles by nature, they tend to force each other away as they move away from their source. At large electrode separation distances, the accelerating voltage potential helps reduce the spread of the electron beam slightly, but the spread of the electron beam cannot be eliminated and it scales proportionally with the eletrode separation distance. As a result, the electrons are distributed over a finite area as they hit the workpiece surface, and hence the energy of the electron beam becomes dispersed. This makes it not suitable for creating sub-micrometer scale features.

At small separation distances, the accelerating potentials are reduced significantly since lower voltages are necessary to achieve field emission. The spread of the electron beam is still there due to the repulsive nature of the electrons. The trajectory of the electrons has been studied extensively by others [7, 48] for various emitter geometries using computational simulations. It has been found that the distribution of the electrons on the workpiece surface is on the order of the emitter-workpiece (electrode) separation distance. Thus, to use field-emitted electron beams for creating sub-micrometer scale features, without the help from electron focusing lenses, field emission must be conducted at small emitter-workpiece distances.

The purpose of this chapter is to demonstrate a successful experimental technique

for characterizing the field emission from individual carbon nanotube (CNT) field emitters or ultra-sharp tungsten field emitters as a function of voltage and separation distance at small electrode separation distances. The results presented in this chapter have already provided useful and realistic experimental data for computation and simulation works by others [6, 7].

This chapter begins with an overview of the electron emission theory.

2.2 Theoretical Background

2.2.1 Electrons Inside Metals and the Work Function

Electrons occupy energy levels in metals. At zero temperature (0 K), all energy levels are completely filled up to the Fermi level E_F and those above are empty. The extent to which a given energy level is filled is described by the Fermi-Dirac function $f(W,T)$ [49, 50], as given in Eq. (2.1). Here, k_B is Boltzmann's constant (1.3806×10^{-23} J/K), and T is the temperature measured in Kelvin (K). This function represents the distribution of electrons with energy W over the energy levels in the metal at temperature T. At 0 K, $f(W,T)$ takes the value 1 for $W \leq E_F$ and 0 otherwise. For temperature $T > 0$ K, some of the electrons just below the Fermi level E_F are promoted to the unoccupied levels just above E_F. At the Fermi level E_F, the value of $f(W,T)$ is exactly 0.5. As the temperature T increases, the range over which $f(W,T)$ drops from 1 to 0 increases and is proportional to the magnitude of k_BT.

$$f\left(W,T\right) = \frac{1}{1+\exp\left[\left(W-E_F\right)/k_BT\right]} \tag{2.1}$$

Electrons are normally retained within the metal due to the presence of a potential energy difference at the interface between the metal and the vacuum. This energy difference, measured from the Fermi level E_F up to the vacuum level, is called the work function ϕ. In other words, the work function is the minimum extra energy an electron must gain to escape from the metal into a field-free vacuum. The work function arises from two effects [51]. The first effect is the inner potential, which is the difference

between the chemical potential of the electron in the metal and that at a far distance from it in a field-free vacuum. The second effect arises from the electrostatic effects at the surface and decays slowly with distance. The value of work function ϕ depends on the material and its crystallographic orientation. For pure metals, the work function ranges from about 2.5 eV to 6 eV [52]. The work function of most high-melting metals (i.e., tungsten has a work function of 4.5 eV) is between 4 and 5 eV [51].

2.2.2 Emission of Electrons

The spontaneous emission of electrons from a metal into vacuum becomes possible when the electrons inside the metal are excited or/and when the metal surface is subjected to a high electric field. Although the main interest in this work focuses on the emission of electrons for the case with high electric field, some explanation of the other types of emission is appropriate and helpful. The emission of electrons from a metal via the excitation of electrons can be divided into two types [51]: photoemission and thermionic emission. Electron energies are measured from zero relative to the Fermi level E_F such that the electrons within the metal see a potential barrier of height ϕ at the interface between the metal and the vacuum. In order for these electrons to escape (emit) from the metal, the electrons must be promoted to the unoccupied energy levels higher than the work function ϕ.

In photoemission [53], the surface of a metal is irradiated by the energetic photons in light. The excitation of electrons is achieved by the absorption of energetic photons, in a quantum electronic phenomenon called the photoelectric effect. Electron emission occurs when the energy gained from the incoming photons is greater than the work function of the metal, i.e., $hv \geq \phi$, where h is Planck's constant (6.6262×10^{-34} Js) and v is the frequency of the electromagnetic radiation. The threshold wavelength lies in the visible or near ultraviolet (i.e., in between 350 nm and 700 nm) for clean metals.

In thermionic emission [49, 51], the metal is heated to a high temperature. The emission of electrons occurs when electrons acquire energy greater than the work function ϕ of the metal. A very weak electric field is usually applied to draw the emitted electrons away from the surface of the metal, but its effect on the emission process can be

ignored.

The emission of electrons can be greatly enhanced if the intensity of the electric field is increased. The electric field F is applied between the metal (electron emitter) and an opposite electrode (electron collector). Usually, the emitter (denoted as cathode) is at ground potential and the collector (denoted as anode) is at a positive voltage potential V ($>$ 0 V) above the ground potential. If the surfaces of the electrodes are flat, resembling two parallel plates separated by a distance s, then the electric field F is simply V/s. If the emitter is emitting electrons, these electrons are attracted to the electron collector. When a sharp needle-shaped emitter is used, the local electric field at the tip of the emitter is greatly enhanced. A sharp emitter limits the electron emitting area and enhances the local electric field at the tip by deforming the equipotential field lines.

The electric field, which deforms the potential barrier at the emitter surface, has two effects on the electron emission process. The potential barrier $V_b(x)$ at the interface between the emitter and the vacuum is given in Eq. (2.2), as a function of the distance x away from the emitter surface. The potential barrier $V_b(x)$ consists of three components: the work function ϕ, the effect of the applied electric field F, and the image charge potential [27]. Where, e is the charge on an electron (1.6022×10^{-19} C) and ϵ_0 is the dielectric permittivity of free space (8.8542×10^{-12} F/m).

$$V_b\left(x\right) = \begin{cases} 0 & ,x < 0 \\ \phi - eFx - e^2/16\pi\epsilon_0 x & ,x > 0 \end{cases} \tag{2.2}$$

The potential barrier $V_b(x)$ is plotted in Fig. 2.1 for two values of electric field: 0.8 V/nm and 2.5 V/nm. The first effect of the electric field is seen directly from Fig. 2.1; the height of the barrier is lowered by an amount $\Delta\phi$. The resulting barrier height, V_m, given in Eq. (2.3), is the adjusted minimum energy an electron must gain to escape from the emitter. Since V_m is less than ϕ, more electrons are emitted. The reduction of the barrier height due to an external applied electric field is known as the Schottky effect, and thus the enhanced electron emission is called Schottky emission [27]. The electric field strength necessary for Schottky emission is typically less than 0.8 V/nm.

$$V_m = \phi - \Delta\phi = \phi - \sqrt{e^3 F / 4\pi\epsilon_0} \tag{2.3}$$

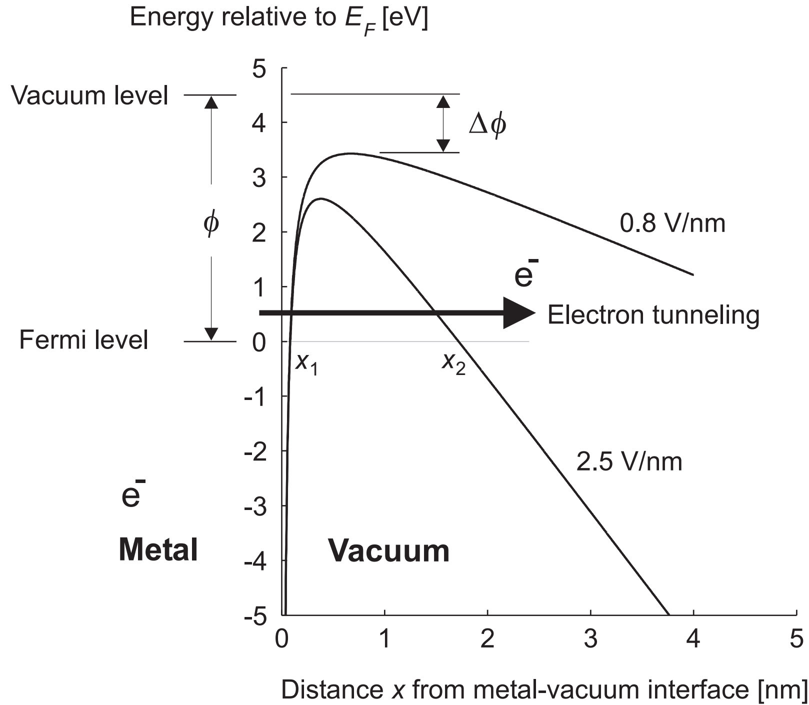

Figure 2.1: Potential energy (in eV) of an electron near a metal surface. A work function of ϕ = 4.5 eV is assumed. $x_2 - x_1$ represents the local barrier width encountered by a tunneling electron.

The second effect is the width of the potential barrier becomes smaller as the electric field increases. It can be seen from Fig. 2.1 that the barrier width $(x_2 - x_1)$ becomes smaller as the electric field increases from 0.8 V/nm to 2.5 V/nm. When the barrier width becomes sufficiently small ($<$ 2 nm), quantum-mechanical tunneling of electrons through the potential barrier also becomes possible. At high temperature and moderate electric field, all electrons at energy levels above V_m are emitted, and a small portion of electrons at energy levels just below V_m can also be emitted by tunneling through the deformed barrier. Thus, the total number of electrons emitted is a combination of the thermionic electrons that originated from above the top of the barrier and the electrons that tunneled through the barrier. This emission is called extended-Schottky emission

[27], and its upper limit of field strength can extend to about 3 V/nm.

At room temperature or below, even unexcited electrons can tunnel through the barrier under the action of intense electric fields (2 - 7 V/nm). The tunneling of electrons occurs mainly near the vicinity of the Fermi level E_F, because no electrons are available at higher energy levels. This electron emission is known as field emission [51]. The effect of higher temperatures on the field emission of electrons is referred to as thermal-field emission.

2.2.3 Emission Current Density: The General Case

Emission current density depends on three physical parameters: the emitter temperature T, the electric field strength on the emitter surface F, and the work function of the material ϕ. In this section, the emission current density derived for a planar emitter over a wide range of temperatures and electric fields is presented.

For a material with work function ϕ, the current density $J(F,T)$, given in Eq. (2.4), is found by integrating over all accessible energies, the product of the charge on an electron e, the number of electrons per second per unit area incident on the barrier $N(T,W)dW$ and the quantum tunneling transmission coefficient $D(F,W)$ [54].

$$J\left(F,T\right)=e\int_{-W_a}^{\infty}D\left(F,W\right)N\left(T,W\right)dW \tag{2.4}$$

W is the combination of the electron kinetic energy normal to the surface of the emitter and its potential energy $V(x)$ near the surface, given in Eq. (2.5), where x is the coordinate normal to the surface and out of the emitter, $p(x)$ is the electron momentum normal to the surface, $V(x)$ is the effective electron potential energy as a function of the distance x from the emitter surface, and m_e is the electron rest mass (9.1096×10^{-31} Kg). $-W_a$ is the effective constant potential energy inside the emitter, at the bottom of the conduction band, which is usually several electron volts below the Fermi level E_F such that $-W_a$ is simply $-(\phi+E_F)$.

$$W=\frac{p^2\left(x\right)}{2m_e}+V\left(x\right) \tag{2.5}$$

The potential energy of an electron near the emitter surface is given in Eq. (2.6), which also describes the potential barrier at the interface between the metal and the vacuum [55]. For simplicity, here the electron energies are measured from zero for a free electron outside the emitter (vacuum level) such that the work function ϕ is simply $-E_F$. The potential barrier composes of two components: $-eFx$ is the contribution from the external applied electric field F and $-e^2/16\pi\epsilon_0 x$ is the contribution from the image charge potential.

$$V(x) = \begin{cases} -W_a & , x < 0 \\ -eFx - e^2/16\pi\epsilon_0 x & , x > 0 \end{cases} \tag{2.6}$$

The transmission coefficient $D(F,W)$ represents the tunneling probability of an electron from the emitter into the vacuum. It depends strongly on the width of the potential barrier encountered by the electron. The transmission coefficient can be evaluated using the Wentzel-Kramers-Brillouin (WKB) approximation [56], given in Eq. (2.7), where x_1 and x_2 correspond to the intersection of W with $V(x)$, such that $x_2 - x_1$ represents the local width of the barrier as shown in Fig. 2.1, and $\hbar$ is Dirac's constant $(1.0546 \times 10^{-34}$ Js).

$$D(F,W) = \left[1 + \exp\left(-2i\hbar^{-1}\int_{x_1}^{x_2}\sqrt{2m_e\left[W - V(x)\right]}dx\right)\right]^{-1} \tag{2.7}$$

Equation (2.7) was evaluated by Murphy *et al.* [54], and the resulting transmission coefficient $D(F,W)$ is presented below for two different conditions. When $W > W_l$, the transmission coefficient is given by Eq. (2.8). And, when $W < W_l$, the transmission coefficient is given by Eq. (2.9). The limiting value W_l is given in Eq. (2.10).

$$D(F,W) = 1 \quad , W > W_l \tag{2.8}$$

$$D(F,W) = \left\{1 + \exp\left[\left(\sqrt{2}/3\right)(4\pi\epsilon_0)^{-3/4}\left(m_e^2 e^5/\hbar^4 F\right)^{1/4} y^{-3/2} v(y)\right]\right\}^{-1} \quad , W < W_l \tag{2.9}$$

$$W_l = -\sqrt{\frac{e^3 F}{8\pi\epsilon_0}} \tag{2.10}$$

The function $v(y)$, given in Eq. (2.11), results from including the image charge potential in the surface potential barrier of Eq. (2.6), with y given in Eq. (2.12). K and E denote the complete elliptic integrals of the first and second kind, respectively [57].

$$v\left(y\right) = \begin{cases} \sqrt{1+y}\left[E\left(\frac{1-y}{1+y}\right) - yK\left(\frac{1-y}{1+y}\right)\right] & , y \leq 1 \\ \\ -\sqrt{\frac{y}{2}}\left[\left(y+1\right)K\left(\frac{y-1}{2y}\right) - 2E\left(\frac{y-1}{2y}\right)\right] & , y > 1 \end{cases} \tag{2.11}$$

$$y = \sqrt{\frac{e^3 F}{4\pi\epsilon_0}\frac{1}{\phi}} \tag{2.12}$$

An assumption is made to calculate the number of electrons incident on the barrier $N(T,W)dW$: metals obey the Sommerfeld free electron model with Fermi-Dirac statistics, Eq. (2.1). Following this asumption, the number of electrons having energy within the range dW incident on the barrier at the emitter surface per second per unit area is given in Eq. (2.13) [58]. Equation (2.13) is also known as the supply function.

$$N\left(T,W\right)dW = \frac{4\pi m_e k_B T}{h^3}\ln\left\{1+\exp\left[-\frac{\left(W-E_F\right)}{k_B T}\right]\right\}dW \tag{2.13}$$

Using the transmission coefficients $D(F,W)$ in Eqs. (2.8) and (2.9) together with the number of electrons incident on the barrier $N(T,W)dW$ in Eq. (2.13), the emission current density [54, 55] becomes Eq. (2.14).

$$J\left(F,T\right) = \frac{4\pi m_e k_B T e}{h^3}\int_{-W_a}^{W_l}\frac{\ln\left\{1+\exp\left[-\left(W-E_F\right)/k_B T\right]\right\}}{1+\exp\left[\left(\sqrt{2}/3\right)\left(4\pi\epsilon_0\right)^{-3/4}\left(m_e^2 e^5/\hbar^4 F\right)^{1/4}y^{-3/2}v\left(y\right)\right]}dW$$

$$+\frac{4\pi m_e k_B T e}{h^3}\int_{W_l}^{\infty}\ln\left\{1+\exp\left[-(W-E_F)/k_B T\right]\right\}dW \tag{2.14}$$

Numerical methods have been used to evaluate the integral in Eq. (2.14), because

no analytical expression to the emission current density exists for a wide range of temperatures and electric fields [55, 59]. Analytical expressions for the current density exist for emission at low temperature and high electric field, or for emission at high temperature and low electric field. Since the primary interest of this work is the emission of electrons at high electric field, only the current density at low temperature and high electric field will be presented.

2.2.4 Approximation of Current Density at Low Temperatures and High Fields

At low temperature ($T \leq$ 1000 K) and high electric field, a widely used approximation for the emission current density is given in Eq. (2.15) with q given in Eq. (2.16). The emission of electrons mainly originates from the vicinity of the Fermi level. The factor $\frac{\pi k_B T/d}{\sin(\pi k_B T/d)}$ accounts for the electrons emitted at energies above the Fermi level due to the temperature effect. Electron emission of this sort is referred to as thermal-field emission. The derivation of this approximation for the emission current density can be found in the works by Murphy *et al.* [54] and Young *et al.* [60]. The approximation in Eq. (2.15), holds as long as $k_B T/q < 0.7$ [61], such that $J(F,T)/J(F,0) \leq 2.7$.

$$J\left(F,T\right) = J\left(F,0\right) \frac{\pi k_B T/q}{\sin\left(\pi k_B T/q\right)} \tag{2.15}$$

$$q = \frac{heF}{4\pi\left(2m_e\phi\right)^{1/2} t\left(y\right)} \tag{2.16}$$

The zero-temperature (0 K) current density $J(F,0)$ is given by the Fowler-Nordheim (FN) equation [62, 63], given in Eq. (2.17). For practical values of electric field F (2 - 7 V/nm), the value of y, from Eq. (2.12), is typically less than one. Thus, from Eq. (2.11), the function $v(y)$ can be reduced to Eq. (2.18) with modulus k^2 given in Eq. (2.19) for the elliptic functions. The function $t(y)$ is given in Eq. (2.20).

$$J_{FN} = J\left(F,0\right) = \frac{e^3 F^2}{8\pi h\phi t^2\left(y\right)} \exp\left(-\frac{8\pi\left(2m_e\right)^{1/2}\phi^{3/2}}{3ehF} v\left(y\right)\right) \tag{2.17}$$

$$v\left(y\right)=\sqrt{1+y}\left[E\left(k^2\right)+yK(k^2)\right] \tag{2.18}$$

$$k^2=(1-y)/(1+y) \tag{2.19}$$

$$t\left(y\right)=v\left(y\right)-\frac{2}{3}\hat{y}\frac{dv\left(y\right)}{dy} \tag{2.20}$$

By using properties of the derivatives of the elliptic function with respect to the modulus k^2 [57], $t(y)$ can be expressed directly in terms of the elliptic functions as given in Eq. (2.21).

$$t\left(y\right)=\left(1+y\right)^{-1/2}\left[\left(1+y\right)E\left(k^2\right)-yK\left(k^2\right)\right] \tag{2.21}$$

Both $v(y)$ and $t(y)$ are slowly varying functions. Burgess, Kroemer, and Houston [64] gave a convenient table for these functions. Alternatively, these functions $v(y)$ and $t(y)$ can be expressed analytically as in Eqs. (2.22) and (2.23), respectively [55, 65]. The dimensionless numerical parameters β_v, α_t, and β_t depend on the work function ϕ of the material. These parameters are listed in Table 2.1 for carbon nanotubes and tungsten emitters. The fit was carried out in the range $F\in$ [2,7] V/nm. For carbon nanotubes (CNTs), with work function ϕ of 4.7 eV as measured by Gao *et al*. for multiwalled CNTs [66], $v(y)$ varies between 0.82 and 0.48, and $t(y)$ varies between 1.03 and 1.07. For tungsten (W), with a work function ϕ of 4.5 eV, $v(y)$ varies between 0.81 and 0.44, and $t(y)$ varies between 1.03 and 1.07.

$$v\left(y\right)=1-y^{\beta_v} \tag{2.22}$$

$$t\left(y\right)=1+\alpha_t y^{\beta_t} \tag{2.23}$$

At room temperature (T = 300 K), with a work function $\phi\leq$ 4.8 eV, the ratio $J(F,T)/J(F,0)\leq$ 1.07 for $F\geq$ 3 V/nm. For higher values of electric field F, the

Table 2.1: Numerical parameters β_v, α_t, and β_t for carbon nanotube and tungsten

Material	Work function ϕ [eV]	β_v	α_t	β_t	References
carbon nanotube (CNT)	4.7	1.6875	0.1156	1.4001	
tungsten (W)	4.5	1.6863	0.1149	1.3909	
	2.5 - 6.0	1.6900	0.1107	1.3300	Ref. [65]
	2.0 - 5.0	1.6552	0.1094	1.2198	Ref. [55]

ratio is even closer to unity. The error is less than 7% at room temperature for practical values of electric field strength. Thus, for emitters that are operated near room temperature or below, the zero-temperature Fowler-Nordheim equation J_{FN} in Eq. (2.17) is widely used.

2.3 Electric Field Enhancement and Emission Area

2.3.1 Generalized Fowler-Nordheim Equation

A more generalized form of the Fowler-Nordheim (FN) equation [67], compared to that in Eq. (2.17), is given in Eq. (2.24); here J_{FN} is replaced with J. The emitted current density J [A/m^2] is expressed in terms of the work function ϕ [eV] and the local electric field at the tip of the emitter F [V/m]. The constants A and B equal 1.541×10^{-6} AeVV^{-2} and 6.831×10^{9} eV$^{-3/2}$Vm^{-1}, respectively.

$$J = \frac{AF^2}{\phi t^2(y)} \exp\left[-\frac{B\phi^{3/2}}{F} v(y)\right] \tag{2.24}$$

The dimensionless functions $v(y)$ and $t(y)$ are given in Eqs. (2.22) and (2.23) for y given by Eq. (2.25). The numerical parameters β_v, α_t, and β_t are listed in Table 2.1.

$$y = 3.7947 \times 10^{-5} \frac{\sqrt{F}}{\phi} \tag{2.25}$$

It has been demonstrated in prior reports of field emission from an elongated (sharp) emitter, such as individual multiwalled CNTs [39, 44, 68], that the current density follows the FN equation, even though it is based on a planar metallic field emitter. Measurements of the current density J and local electric field F at the tip of an emitter cannot

be performed directly. However, the experimentally measurable quantities, current I [A] and voltage V [V], are related to the FN equation by Eqs.(2.26) and (2.27). Where, A_{eff} [m^2] is the effective emitting area, λ is the dimensionless field amplification factor due to a sharp tip, and s [m] is the separation distance measured from the tip of emitter to the anode surface.

$$J = I/A_{eff} \tag{2.26}$$

$$F = \lambda V/s \tag{2.27}$$

Equation (2.26) assumes that the current density distribution over A_{eff} is uniform and equal to the maximum current density at the tip of the emitter. From previous theoretical and numerical works, this assumption is unsatisfactory to some extent [69, 70, 71, 72] since the current density distribution over the emitter surface where the electrons are emitted is not uniform due to the non-uniformity in the electric field strength across the surface. Furthermore, the actual emitting area depends on the applied electric.

The current density distribution over the emitter surface can be obtained through numerical simulation or analytical modeling provided that the geometry of the emitter is known *a priori*. The emission current is then obtained by integrating the current density distribution $\hat{J}$ over the surface of the emitter and is given by $I = \int_0^A \hat{J} dA = A_s \alpha J$. From this relation, one can notice that the same emission current can be obtained by multiplying the maximum current density J at the tip of the emitter by a factor $A_s \alpha$. The dimensionless parameter α is commonly known as area factor and it varies with the electric field F at the tip of the emitter as given in Eq. (2.27). If the tip of the emitter is assumed to be hemispherical, then A_s is the surface area of the hemisphere given by $2\pi r^2$, where r is the radius of the hemisphere. The entity A at the upper limit of the integral denotes the actual emitting area where the electrons are emitted.

The values of α have been calculated by others [69, 70, 71, 72] for various emitter geometries and it was found that α varies almost linearly and rather slowly with the

local electric field F at the tip of the emitter. The dependence of α on electric field is negligible when compared to the exponential term in Eq. (2.24). Thus, the product of $A_s\alpha$ is commonly assumed to be constant in experimental works. With this assumption, $A_s\alpha$ becomes equivalent to the effective emitting area A_{eff} of Eq. (2.26). Although it is of little importance in this work, a few more comments about the effective emitting area A_{eff} is neccessary. A_{eff} is the truncated emitting area with uniform current density and therefore it is not the actual emitting area. The actual emitting area A can be a few times larger than A_{eff} and it must be obtained through some device modeling [69].

2.3.2 Electric Field Enhancement

In order to produce appreciable field emission current density, electric fields in the range of 3 to 7 V/nm are neccesary. To establish such high electric fields with convenient values of applied voltage, i.e. $<$ 3 kV, the emitter (cathode) is usually needle-shaped with a high aspect ratio [73]. A sharp emitter forces the equipotential lines to bend and follow the shape of the emitter. As a result, the local electric field at the tip of the emitter is greatly enhanced. Since the electric field at the tip of the emitter is always higher than anywhere else on the emitter surface, electrons are emitted primarily from the tip of the emitter. The enhancement of the electric field at the tip of the emitter depends strongly on the geometry of both the electrodes and their separation distance.

Caution is necessary when considering experimental or computational work at small cathode-anode distances. The definition of the cathode-anode distance and the relationship to the local electric field at the tip of the emitter can be analyzed differently, and hence seemingly similar terms might describe different physical values. This dissertation uses the term separation distance s measured between the flat anode and the tip of the emitter [68], while Bonard *et al.* [44] used the distance d measured between the flat anode and the flat substrate of the cathode (emitter). Therefore, the separation distance s differs from d by the height h of the emitter.

For large distances, this difference is negligible, but as s approaches zero, d approaches h. This difference is important when considering the enhancement (or amplification) of the local electric field at the tip of the emitter [74]. Historically, the electric

field F at the tip is related to the applied voltage V by $F = \beta V$, where the field factor β has the dimension [1/length]. More recently, the field F is related to both the voltage V and distance d using $F = \gamma V/d$, where γ is the dimensionless field enhancement factor.

In this work, the electric field F at the tip of the emitter is related to the separation distance s and voltage V using $F = \lambda V/s$, and λ is the field amplification factor to distinguish it from the field enhancement factor γ. At large distances, the difference between λ and γ is indistinguishable $(\lambda_\infty = \gamma_\infty)$ since $s \approx d$, but their difference becomes substantial for small distances where s and d differ by the height h of the emitter. In fact, the amplification factor λ approaches unity (no field amplification) as s approaches zero, but the enhancement factor γ mathematically approaches infinity as s approaches zero [68].

Most previously conducted field emission studies were performed at large distances, and hence a model for estimating the field amplification factor λ at small separation distances needs further study. There is only one reported model, suggested by Miller *et al*. [75], that uses the same definition of the separation distance s used in this work, and the model considers a grounded sphere floating between a grounded plane and a charged plane. Miller *et al*. [75] gave the model for the field amplification factor λ, which varies with the separation distance s that is given in Eq.(2.28), where λ_∞ corresponds to the field amplification factor at distant field (i.e., $s \gg h$) and h is the effective height of the emitter. This model is valid for a separation distance $s \geq h$. When $s = h$, λ = 0.5λ_∞. When $s = 10h$, λ = 0.91λ_∞. And, when $s = 100h$, λ = 0.99λ_∞. This means that λ approaches λ_∞ when $s \geq 100h$.

$$\lambda = \lambda_\infty \frac{s}{s+h} \tag{2.28}$$

An even better expression for λ is given in Eq.(2.29) [75], which is valid for all values of separation distance s (including $s < h$). The exponential term $\exp\left(-\frac{s}{h}\sqrt{\lambda_\infty}\right)$ accounts for λ approaching unity (no field amplification) when the separation distance s becomes much smaller than the height h and tip radius r of the emitter since the geom-

etry approaches that of two opposing infinite planes, effectively eliminating geometric field amplification. For $s \geq h$, λ still varies very much like Eq.(2.28). For $s \gg h$, the exponential term simply vanishes.

$$\lambda = \lambda_\infty \frac{s}{s+h} + \exp\left(-\frac{s}{h}\sqrt{\lambda_\infty}\right) \tag{2.29}$$

When $\lambda_\infty \gg 1$, the exponential term can be replaced by a unity term in the modified form of Miller's equation so that the field amplification factor λ is given by Eq.(2.30) [68], which is also valid for all values of separation distance s with minimal error. The modified Miller equation describes the behavior of the field amplification factor λ as it varies over a large range of separation distance s. The field amplification factor λ asymptotically approaches a value of unity when the separation distance s becomes very small or approaches λ_∞ when the separation distance s is very large compared to the height h of the emitter.

$$\lambda = \lambda_\infty \frac{s}{s+h} + 1 \tag{2.30}$$

To validate the modified Miller equation for an emitter shaped as a hemisphere-on-post, the local electric field F at the tip of the emitter is computed using electrostatic finite element analysis (COMSOL software) for separation distances varying from 5 nm to 10 μm and with a fixed tip radius r = 10 nm and height h = 1 μm. When the electron space charge in between the electrodes is negligible, the electric potential within the vacuum between the electrodes is given by the solution to the Laplace's equation ($\nabla^2 V = 0$). The boundary conditions are established by setting the surface of the emitter (cathode) to ground potential and the anode surface to a positive voltage potential. Boundaries far away from the electrodes are assumed to be electrically insulated to account for the vacuum. The electrostatic field is obtained from **F** $= -\nabla V$. Once the electric field F at the tip is computed, the field amplification factor λ can be calculated from Eq.(2.27). Figure 2.2 demonstrates that the modified Miller equation is also effective for this emitter, which shaped as a hemisphere-on-post. From the data in Fig. 2.2, it is clear that the modified Miller equation fits the data well, and it yields a value of λ_∞

equal to 75.2 for the known emitter height.

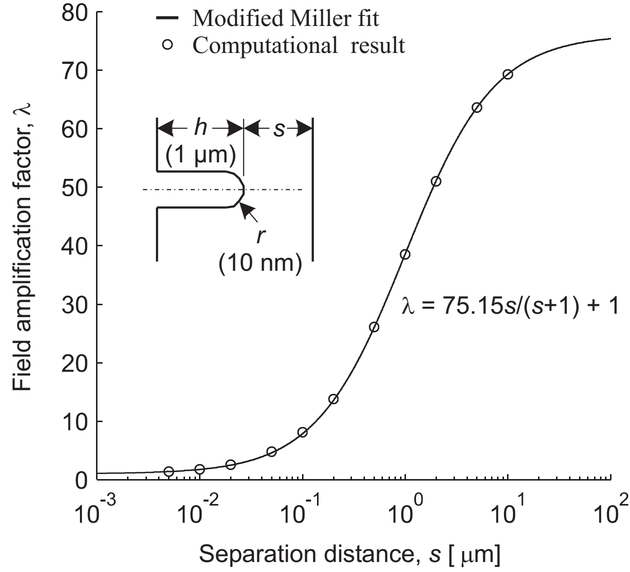

Figure 2.2: Field amplification factors computed by finite element analysis for a hemisphere on post with tip radius $r = 10$ nm and height $h = 1$ μm and fit with the modified Miller equation.

The field amplification factor λ_∞ for the geometry of this emitter at large distance can also be determined from Eq.(2.31), valid for $4 \leq h/r \leq 3000$, as given by the computational result of Edgcombe and Valdre [76]. Their expression gives λ_∞ = 77.2, so that the values from the modified Miller equation differ by less than 3%. This error would be even smaller if more numerical data were computed for separation distance s larger than ten times the height h of the emitter. Therefore, the modified Miller equation is a very reasonable empirical model for how the field amplification factor λ varies with separation distance s over a large range of values.

$$\lambda_\infty = 1.2\,(h/r + 2.15)^{0.9} \tag{2.31}$$

Alternatively, the electric field F at the tip of the emitter can be related to the distance d and voltage V using $F = \gamma V/d$, where γ is the field enhancement factor and d is the distance measured between the planar anode and the planar substrate of the cathode

(emitter) such that $d = s + h$. With this definition of distance d and based on fitting a curve to the data published by Edgcombe *et al.* [76], Bonard *et al.* [44] found that the empirical model that describes the behavior of the field enhancement factor γ, which varies with d over a large range of values, is given in Eq.(2.32).

$$\gamma = \gamma_\infty \left[1 + 0.013\left(\frac{d}{d-h}\right) - 0.033\left(\frac{d-h}{d}\right)\right] \tag{2.32}$$

Figure 2.3 compares the empirical models for an emitter with a tip radius r = 10 nm and height h = 2 μm. Clearly, the field enhancement factor γ and the field amplification factor λ vary very differently with the separation distance s or $d - h$. The field enhancement factor γ increases significantly when the distance d becomes smaller than a quarter of the emitter height h, but it levels off for large distances. In apparent contrast, the field amplification factor λ, which varies significantly in the range $0.01h < s < 100h$, decreases as the separation distance s decreases, but it also stabilizes to a constant value at large separation distance. At very small distances $s \leq h$, γ becomes very large whereas λ approaches unity. At large distances $s \geq 100h$ (distant field), the difference between the field enhancement factor γ and the field amplification factor λ is indistinguishable, and thus γ_∞ and λ_∞ are equivalent.

2.3.3 Extraction of FN Parameters

It is common practice to extract the FN parameters from the best-fit straight line on a plot of data using the FN coordinates, which are $1/V$ along the abscissa and ln(I/V^2) along the ordinate. Such a plot is commonly known as an FN plot. Then, the FN parameters, effective emitting area A_{eff} and field amplification factor λ (or enhancement factor γ) are determined from the ordinate intercept and the slope of the best-fit straight line on the FN plot.

Using J given in Eq. (2.26) and F given in Eq. (2.27), and taking the natural logarithm of Eq. (2.24), the FN equation can be linearized as given in Eq. (2.33) by assuming that $v(y) = 1$ and $t(y) = 1$ to avoid the evaluation of the elliptic functions.

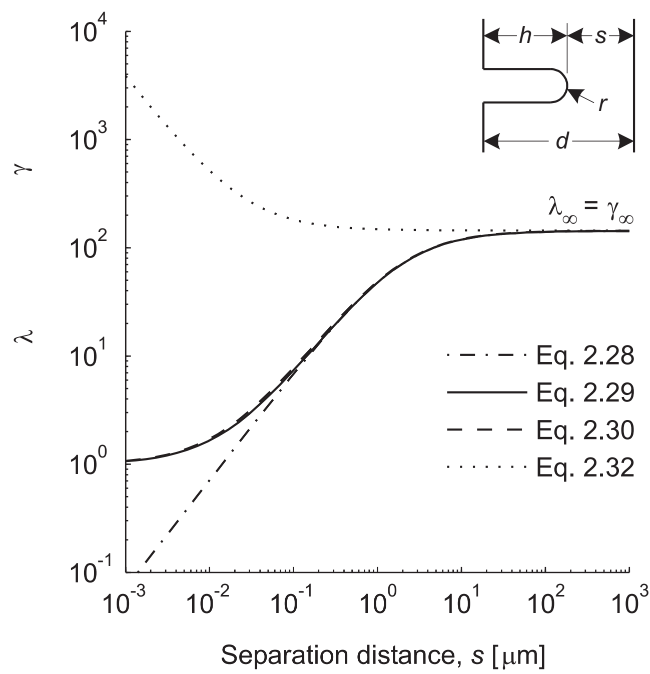

Figure 2.3: Comparison of empirical models for field enhancement factor γ and field amplification factor λ as a function of separation distance s for an emitter with a tip radius r = 10 nm and height h = 2 μm.

$$\ln\left(\frac{I}{V^2}\right) = -\frac{B\phi^{3/2}s}{\lambda}\left(\frac{1}{V}\right) + \ln\left(\frac{A\lambda^2 A_{eff}}{\phi s^2}\right) \tag{2.33}$$

Clearly, the slope of the FN plot is $-\frac{B\phi^{3/2}s}{\lambda}$ and the ordinate intercept is $\ln\left(\frac{A\lambda^2 A_{eff}}{\phi s^2}\right)$. The field amplification factor λ calculated from the slope of the FN plot can be used since the simplifications $v(y) = 1$ and $t(y) = 1$ produce a small error of only about 4% to 8% [77]. The emitting area A_{eff}, on the other hand, calculated from the ordinate intercept, can be larger by a factor of 56 - 185 for ϕ = 4.5 eV [77]. The reason is that, even a small deviation of $v(y)$ from 1 causes a large error in the current density due to the exponential term in Eq. (2.24). For practical values of electric fields and wide range of work function ϕ, $v(y) = 1$ gives current densities which are too small by a factor 10^2 - 10^6 [55].

To calculate the emitting area A_{eff} more precisely, the variation of $v(y)$ and $t(y)$ in Eq. (2.24) must be accounted. $t(y)$ is a very slowly varying function so that $t^2(y) = t_N^2$. And, $v(y)$ can be approximated by a quadratic function [78] so that $v(y) = s_a - u_a y^2$. From Eq. (2.25), y can be written as $y = C\sqrt{F}/\phi$, where, C is simply 3.794686×10^{-5} eV$\text{V}^{-1/2}\text{m}^{1/2}$. The modified FN equation is given in Eq. (2.34) [79], which can also be linearized.

$$I = \frac{A\lambda^2 A_{eff} V^2}{\phi s^2 t_N^2}\exp\left(\frac{u_a BC^2}{\sqrt{\phi}}\right)\exp\left(-\frac{s_a B\phi^{3/2}s}{\lambda V}\right) \tag{2.34}$$

The new slope and ordinate intercept are $-\frac{s_a B\phi^{3/2}s}{\lambda}$ and $\ln\left(\frac{A\lambda^2 A_{eff}}{\phi s^2 t_N^2}\right) + \frac{u_a BC^2}{\sqrt{\phi}}$, respectively. Here, $t_N^2 \approx$ 1.1 [77, 78], BC^2 = 9.83624 eV$^{1/2}$, $s_a = 0.95$ [78, 79], and $u_a = 1.0$ [78, 79]. The emitting area A_{eff} and field amplification factor λ calculated using the approximated $v(y)$ and $t(y)$ are for verification purposes. The exact and approximate functions of $v(y)$ and $t^2(y)$ are plotted in Fig. 2.4.

For practical values of electric fields ($2 < F < 7$) V/nm and ϕ = 4.5 eV, y varies from 0.377 to 0.706, the maximum error associated with the approximate $v(y)$ is about 2.5%. Whereas, the functions $v(y)$ and $t(y)$ given in Eqs. (2.22) and (2.23), as recommended by Paulini *et al.* [55], give a maximum error of 0.3%. In Section 2.6, these functions will be used in an improved technique for extracting the effective emitting area A_{eff}

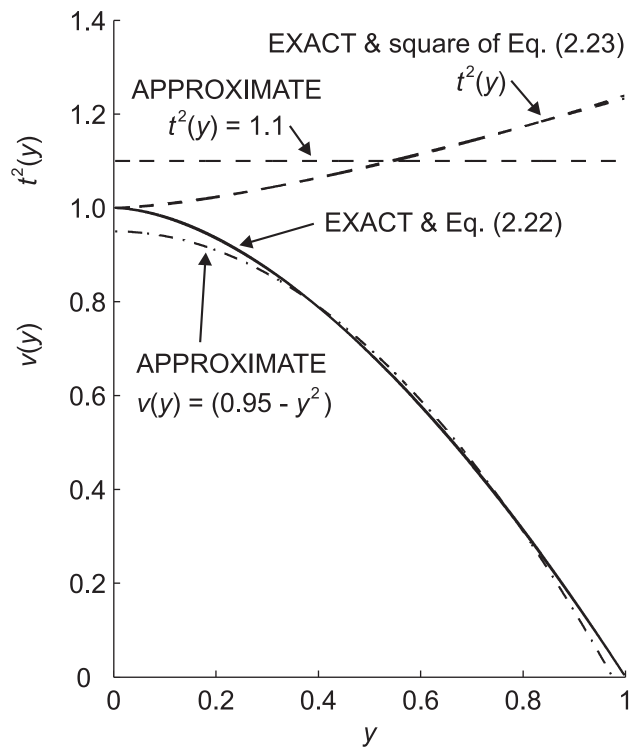

Figure 2.4: Comparison of approximate forms with exact solutions for the Fowler-Nordheim field emission functions $v(y)$ and $t^2(y)$ for ϕ = 4.5 eV.

and field amplification factor λ in which it utilizes a nonlinear least squares curve fitting algorithm that fits the FN equations given in Eqs. (2.24) - (2.27) to a measured $I(V)$ curve [68].

2.4 Preparation of Electrodes

This section describes the preparation of the field emitters and the electron collector used in the field emission experiments. Recall that the field emitter is the cathode and the electron collector is the anode.

2.4.1 Sharp Tungsten Field Emitter

Tungsten wires of 99.9% purity (Supplier: GoodFellow) with 150 μm in diameter and 30 mm in length were obtained from 300 mm long straightened tungsten wires. Sharp tungsten tips were prepared by electrochemical etching in 2.0N NaOH standardized solution with DC voltages that are controlled by a circuit, which detects a sudden change in the etch current when the submerged portion covered with a layer of epoxy or heat-shrink poly-tetrafluoroethene (PTFE) tube of the wire drops [80].

The electrochemical etching apparatus for preparing sharp tungsten tips is shown in Fig. 2.5. The time progression of the electrochemical etching process of a tungsten wire is shown in Fig. 2.6 prepared with this method. The scanning electron micrographs (SEM) of Fig. 2.7 show a few sharp tungsten field emitters. The tips of the etched tungsten wires exhibit a parabolic/hyperbolic shape with tip radii typically around 15-100 nm [80].

2.4.2 Carbon Nanotube Field Emitter

To prepare the CNT field emitter, an individual multiwalled CNT, synthesized by chemical vapor deposition (CVD) using xylene and ferrocene [29], is attached to the tip of an etched tungsten wire in two steps. The first step begins with aligning a sharp tungsten tip with a single CNT that protrudes from a film of CNTs, as shown in Fig. 2.8(b), using

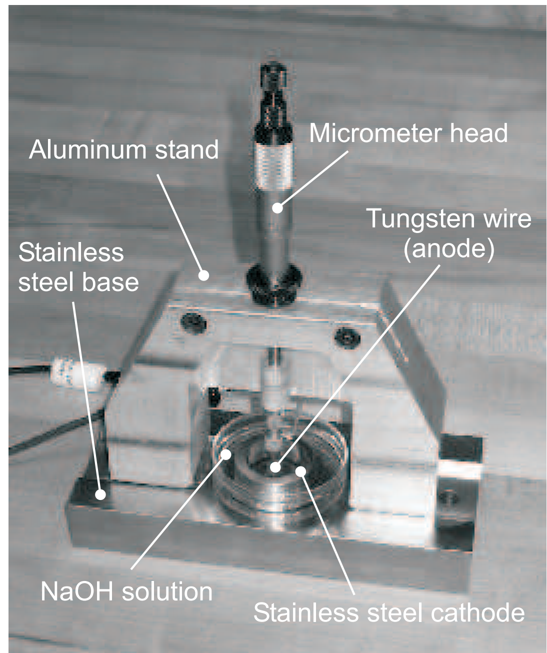

Figure 2.5: Electrochemical etching apparatus for preparing sharp tungsten tips [80].

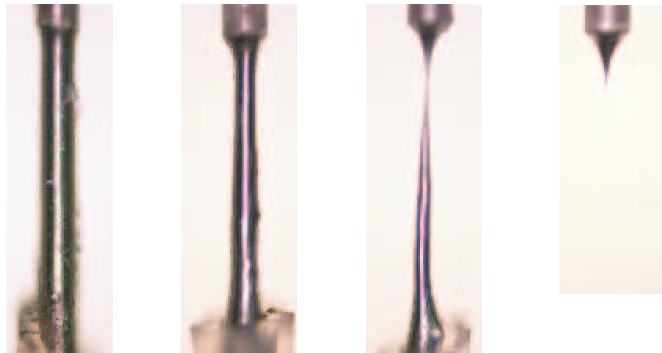

Figure 2.6: Time progression of electrochemical etching process of a tungsten wire [80].

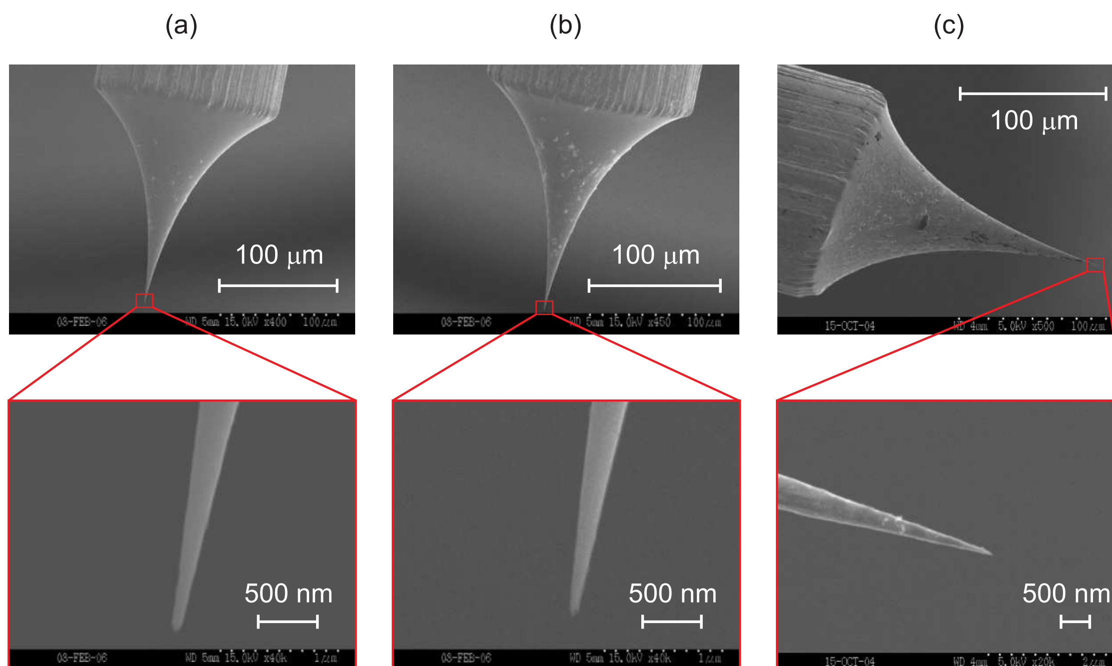

Figure 2.7: Sample images of sharp tungsten field emitters.

the CNT attachment apparatus shown in Fig. 2.9 that operates under an optical microscope (Nikon, LHS-H100P) with a maximum magnification of 1000×. A sharpened tungsten wire was clamped onto a standard SEM mount by a stainless steel rod. The source of CNTs is an electrically conductive carbon tape adhered with clusters or film of CNTs.

In the second step, the CNT is broken (oxidized) by Joule heating after flowing an electrical current through it, as shown in Fig. 2.8(c). After breakdown, a segment of the CNT remains attached to the tungsten tip. Figure 2.10 shows a measurement of the electrical current that flows through a CNT as a function of applied voltage during the cutting process. For this particular CNT, it broke at 6.9 V, which corresponds to an electrical current of about 82 μA. Typically, it would need an electrical current on the order of 10 to 100 μA to cut a CNT and the applied voltage can vary from 5 to 15 V. The scanning electron micrographs of Fig. 2.11 illustrate a few CNT field emitters obtained using the fabrication technique described above.

This technique of individual CNT attachment is much more reliable than the arc-

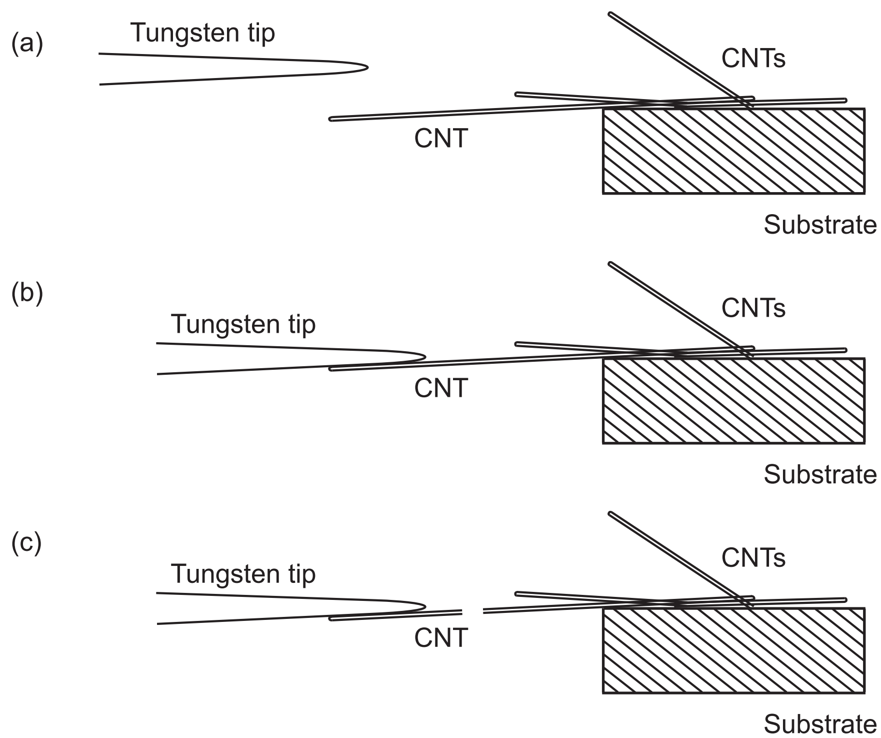

Figure 2.8: Procedures for attaching a carbon nanotube (CNT) to a tungsten tip. (a) A CNT protruding from a thin substrate containing many CNTs is selected and (b) is aligned and attached to a tungsten tip, and (c) the CNT is broken by Joule heating after flowing an electrical current through it.

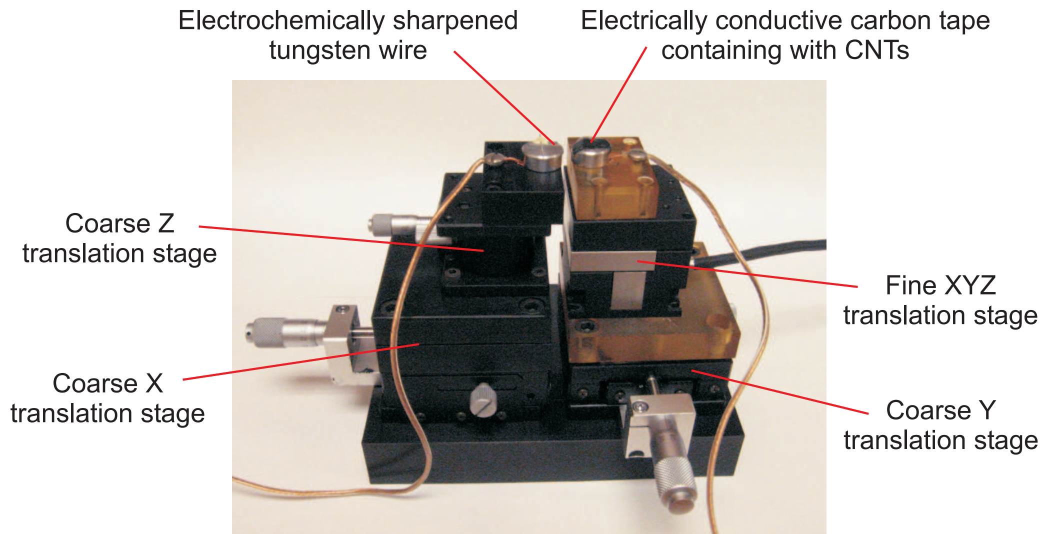

Figure 2.9: Apparatus for preparing carbon nanotube (CNT) field emitters.

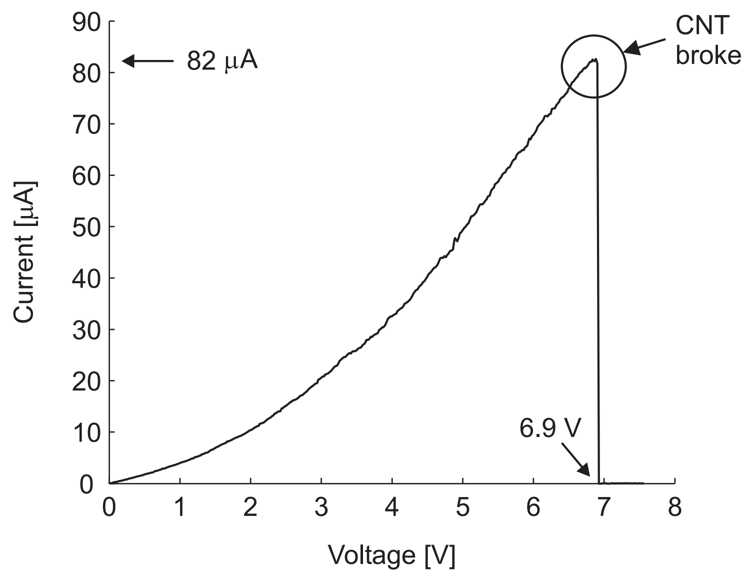

Figure 2.10: A measurement of the electrical current that flows through a CNT as a function of applied voltage during the cutting process.

discharge technique [80], which often yielded various outcomes such as multiple CNTs attached to the tungsten tip, CNT(s) attached too far from the tip, or even without any CNT attached to the tip at all. This improved technique is similar to those described by others [27, 81, 82, 83, 84], but no adhesive was used on the tungsten tip. Attempts to grow a single CNT on the tungsten tip were also conducted, but it was unsuccessful. Instead of CNTs, tungsten oxide nanorods with carbon caps were grown on the tungsten tip [85].

The attached CNTs may have a closed end, an open end, or an irregular end that might be opened in some places. The ends of CNTs shown in the scanning electron micrographs of Fig. 2.11(a) - (c) appear to be opened. Whereas, the end of CNT shown in the scanning electron micrograph of Fig. 2.11(d) appears to be closed. Furthermore, the end (tip) condition of the CNT might change as suggested by some experimental evidence of unraveling [25] or closing [86] during field emission.

2.4.3 Electron Collector

The anode was a cleaved optical fiber (125 μm in diameter) that was coated with copper (Cu) along its cylindrical surface to connect with a gold (Au) layer deposited on the fiber's cleaved end. The depositions of the Cu-Au layer on the fiber were performed in a thermal evaporator. The scanning electron micrographs of Fig. 2.12 show a typical Cu-Au coated optical fiber. This allows for an arrangement of the electrodes that aims a sharp cathode (field emitter) at a much larger anode surface, which is flat and smooth to within $\sim$ 10 nm [80] as estimated by Zygo scanning white light interferometry.

2.5 Experimental Methods and Apparatus

Field emission of electrons from sharp emitters requires an ultra-high vacuum (UHV) environment to ensure stable emission current conditions. The adsorption and desorption of the residual gas atoms or molecules onto the electron emitting sites in a poor vacuum condition causes the emission current to fluctuate considerably because the emitting area is small. A UHV chamber together with other instrumentation was there-

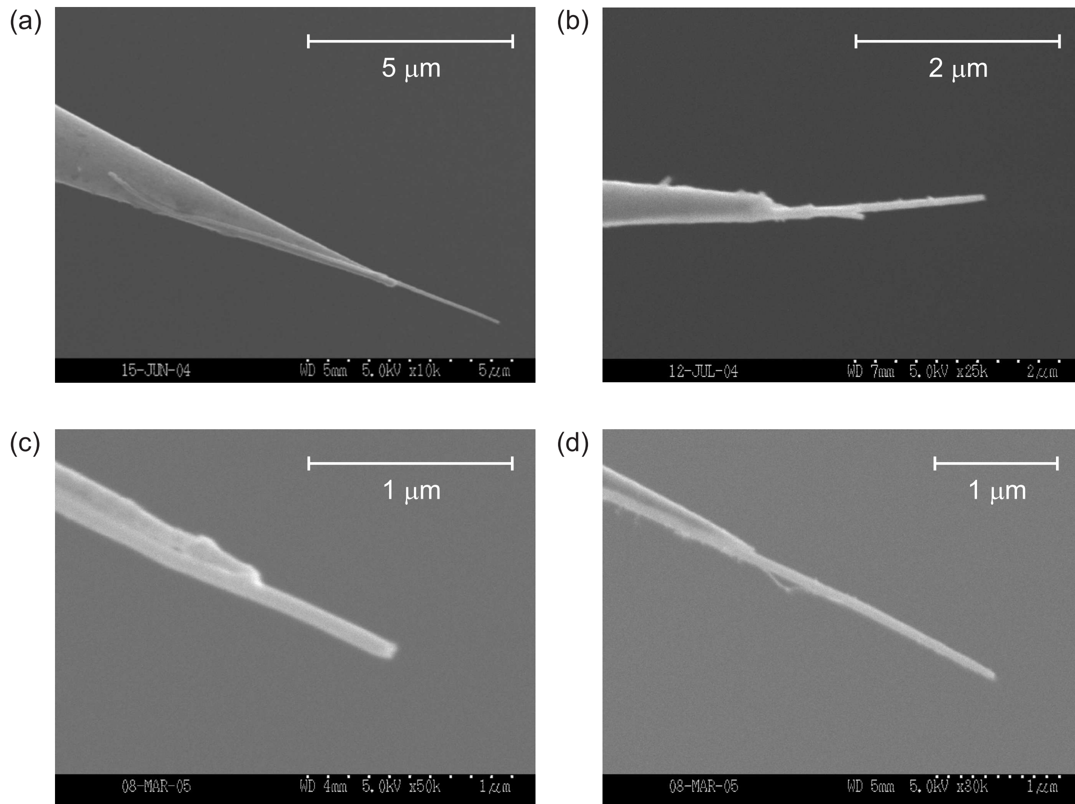

Figure 2.11: Sample images of CNT field emitters.

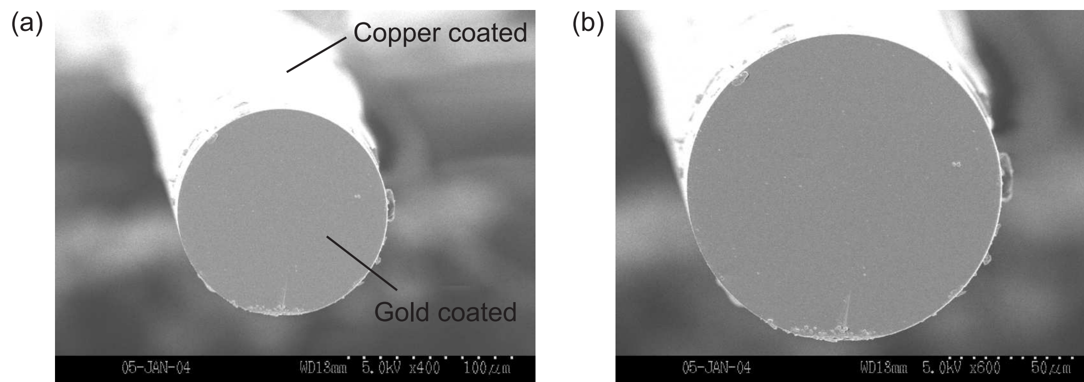

Figure 2.12: Sample images of anode.

fore necessary to carry out the experiments. All field emission experiments described in this chapter were carried out under vacuum conditions in the 10^{-8} to 10^{-9} Torr pressure range.

2.5.1 Ultra-High Vacuum Chamber

The ultra-high vacuum chamber system, designed by the author and fabricated by Kurt J. Lesker Company, is mounted on a granite slab that floats on four pneumatic vibration isolators, as shown in the photograph of Fig. 2.13. The top flange can be removed if an installation is needed inside the UHV chamber. A load-lock station is separated from the UHV chamber by a manual gate valve. This station, which handles sample transfer, is for future upgrades. The load-lock station is evacuated with a turbomolecular pump combined with an oil-free mechanical backing pump. These pumps are also used to evacuate the UHV chamber during bakeout.

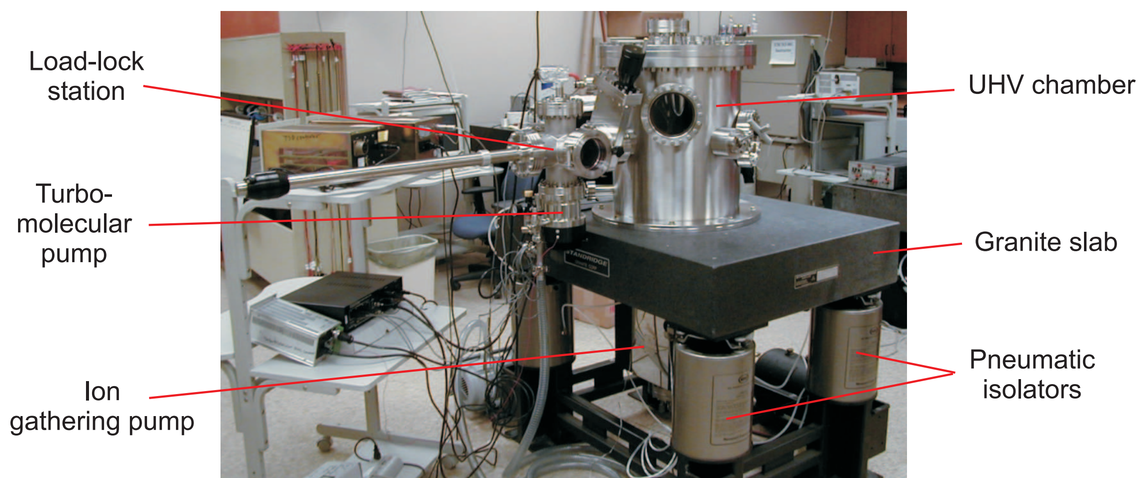

Figure 2.13: Photograph of the ultra-high vacuum chamber system for experimental studies.

Bakeout of the chamber is performed with four stab-in heaters, and the bakeout duration is usually 1 to 7 days. The temperature on the chamber walls can reach as high as 200°C during bakeout. The UHV chamber is pumped by a 240 l/s ion gathering pump together with a titanium sublimation pump (TSP). After bakeout, the

base pressure in the UHV chamber is typically between 10^{-9} and 10^{-10} Torr. Without bakeout, the base pressure in the UHV chamber is usually around 10^{-8} Torr.

2.5.2 Apparatus and Instrumentation

Measurements of the emission current I as a function of the applied voltage V and the separation distance s were performed using the apparatus and instrumentation illstrated in Fig. 2.14, which consists of a nanopositioning stage, a high gain transimpedence amplifier, and a low-noise low-leakage high voltage power supply. A personal computer (PC) controls the experiments and records the measured data. The photograph of Fig. 2.15 show the experimental setup inside the UHV chamber used for field emission experiments. All the components of the experimental setup inside the UHV chamber were carefully designed and selected to minimize outgassing, and must also endure high temperature during the bakeout process.

The nanopositioning stage is guided by a double-compound flexural bearing [87] that is actuated by a UHV-compatible piezoelectric (PZT) actuator with about a 21 μm displacement range. The separation distance s of the electrodes is controlled by the PC using an analog signal to a piezoelectric amplifier (Polytec PI, Model E-501.00). The displacement of the nanopositioning stage as a function of the applied voltage to the PZT actuator is plotted in Fig. 2.16.

As shown in the photograph of Fig. 2.14, the anode and cathode are passively aligned by pressing them into two grooves that were micro-machined into quartz substrates [88]. Stainless steel wires were used to preload the electrodes into the grooves and provide electrical contact with each electrode. This arragement of electrodes allows the cathode to remain stationary, and the anode moves when the piezoelectric actuator presses against the flexural bearing.

For generating DC voltages, a high-voltage power supply (Bertan Model 230-03R) was used, which can be remotely controlled by the PC. In the experiments, the high electric field needed for electron emission was generated by application of a positive DC voltage to the anode. For measuring the emission current, a transimpedence amplifier (Keithley, Model 428) was used that has adjustable gains from 10^{3} to 10^{11} V/A.

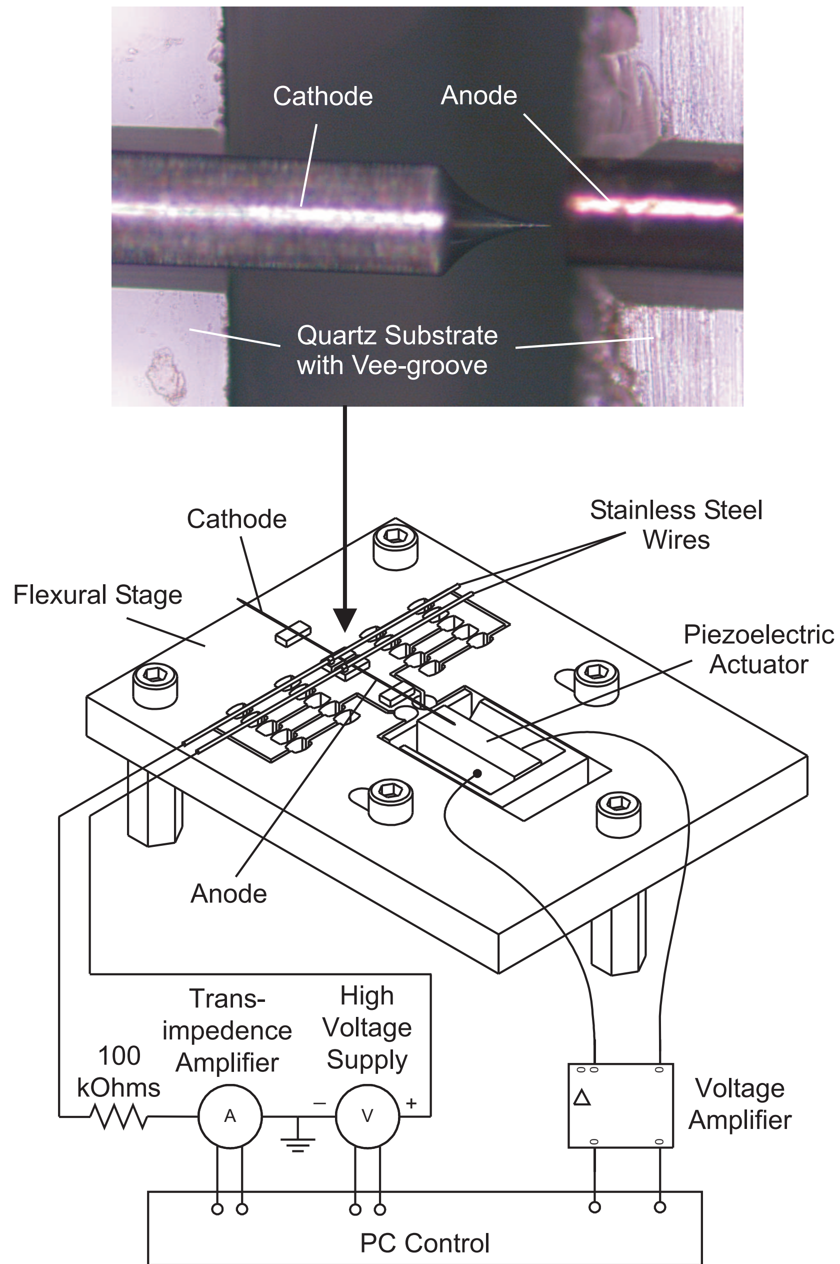

Figure 2.14: Apparatus and instrumentation for field emission measurement at small anode-cathode distances.

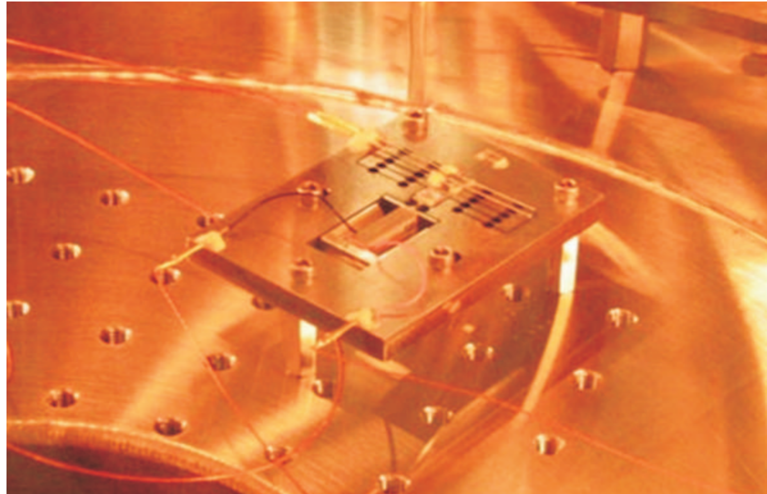

Figure 2.15: Photograph of the experimental setup inside the UHV chamber used for field emission experiments.

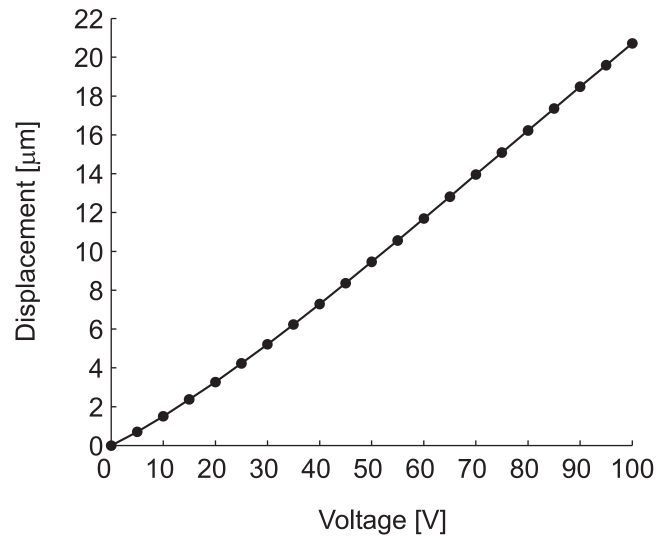

Figure 2.16: Displacement of the nanopositioning stage as a function of the applied voltage to the piezoelectric (PZT) actuator.

The cathode is connected to the transimpedence amplifier, which is virtually held at ground potential. The electrical connection of the electrodes, the high-voltage power supply, and the transimpedence amplifier are shown in Fig. 2.14. The addition of a 100kΩ resistor in the connection close to the emitter serves as a suppresor, which also protects the transimpedence amplifier in the event of high-voltage arcs.

2.5.3 Experimental Procedure

In measuring field emission at small distances, it is essential to establish a datum for measuring the separation distance s precisely so that the local electric field at the tip of an emitter can be determined accurately in later analyses. This is accomplished by detecting the anode surface with the tip of the emitter prior to measuring any $I(V)$ curves. A simple non-destructive technique was used, which detects tunneling current, by slowly closing the gap between the electrodes at a rate of about 4 nm/s or less until a small bias voltage (typically 0.5 V to 2.0 V) produces a sudden increase in the current. The gain of the transimpedence amplifier was set to 10^{10} V/A.

The sudden increase typically occurs over less than a few nanometers of displacement, so the initial separation distance is known to within the same value as the surface roughness/flatness in the vicinity where the electrons strike the anode. In order to use this surface detection technique, the initial separation distance between the tip and the anode surface must be within the displacement range of the PZT actuator. Once the anode surface is detected, the anode is retracted to its home position. The initial separation distance is then determined from the recorded voltage applied to the PZT actuator using the data shown in Fig. 2.16.

An example of the measured current during surface detection is plotted in Fig. 2.17 as a function of the distance traveled by the anode, for the CNT field emitter (cathode) shown in Fig. 2.11(b). This experiment was conducted with a bias voltage of 1.0 V applied to the cathode. The current increased gradually to about 4 pA while the anode traveled 13.567 μm, and then it suddenly jumped to about 1 nA during an additional travel of only 4 nm. From this data, it was concluded that the initial separation distance between the tip of the CNT and the anode surface was about 13.571 μm, which

served as the datum (home position) for determining the separation distances in the subsequent experiments.

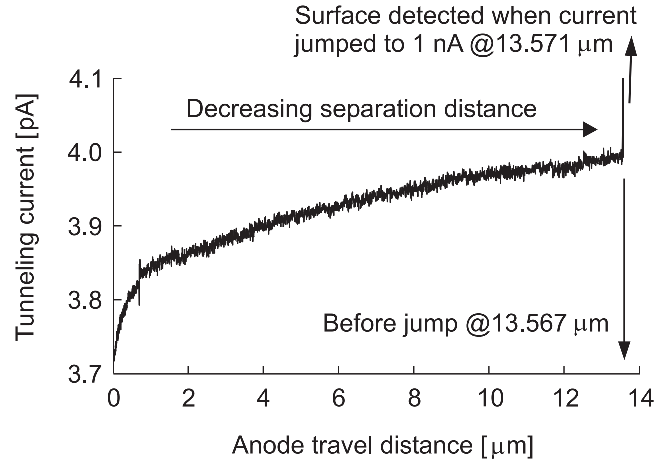

Figure 2.17: Surface detection for establishing datum and initial separation displacement of electrodes (home position).

Once the initial separation distance at the home position is known, a preliminary field emission test was conducted to remove some of the absorbates on the emitter surface [89]; current was maintained until the emission current become reasonably stable. After the cleaning process, $I(V)$ curves were measured at several separation distances. The gain setting of the transimpedence amplifier for the $I(V)$ measurements was 10^7 V/A, which can measure currents up to 1 μA. A single $I(V)$ data point represents the mean current recorded at a given applied voltage over a one second period at a sampling frequency of 10 kHz. Three $I(V)$ curves were recorded at each separation distance s with the applied voltage ranging from below the turn-on voltage up to the voltage when a few hundred nanoampere of current is detected. The turn-on voltage is the voltage required to produce 1 nA of emission current. An average $I(V)$ curve was constructed using the mean of the three measured $I(V)$ curves at each separation distance s.

To reduce the error in the separation distance s, the nonlinearities in the displacement of the PZT actuator were corrected with prior calibration. The creep behavior of the PZT actuator, which is the change in position as a function of time $\Delta L(t)$ [μm], was

corrected using Eq. (2.35), where t [s] is time, $\Delta L_{t=0.1}$ [μm] is the displacement 0.1 seconds after the voltage change is complete, and γ_c is the creep factor (on the order of 0.01 to 0.02, which is 1% to 2% per time decade). The PZT actuator used in the nanopositioning stage has a creep factor γ_c of about 0.01.

$$\Delta L\left(t\right) \cong \Delta L_{t=0.1}\left[1+\gamma_c \log\left(\frac{t}{0.1}\right)\right] \tag{2.35}$$

2.6 Characterizing Field Emission at Small Separation Distances

In this section, the characterization of field emission by means of current-voltage $I(V)$ measurements at small electrode separation distances is presented. Two types of field emitters were used: a carbon nanotube (CNT) field emitter and a sharp tungsten field emitter.

2.6.1 Carbon Nanotube Field Emitter

This section presents the electron field emission from an individual CNT attached to a sharp tungsten tip using the preparation methods in Section 2.4. The CNT field emitter used in the experiments is shown in the scanning electron micrograph of Fig. 2.11(b). A CNT with $\sim$ 60 nm in diameter protrudes about 2.1 μm from the sharpened tip of a 150 μm diameter tungsten wire. Twenty-four sets of $I(V)$ data were measured at electrode separation distances s between 1.46 and 13.43 μm. The data was compensated for a voltage drop due to an effective series resistance of about 10 MΩ in the field emission circuit. The presence of a large resistance in series with the emitter, which causes the saturation behavior in the emission current [89, 90], is not uncommon, as Bonard *et al.* [91] reported that the contact resistance at the CNT-substrate interface is typically between 300kΩ and 400MΩ.

The nonlinear least squares curve fitting technique described in Section 2.3 was used for fitting the FN equations to each of the twenty-four measured $I(V)$ curves using emission current greater than 0.1 nA. These fits yielded the values for the field amplification factor λ and the effective emitting area A_{eff} at each of the separation

distances s. These values are compared to the values of the field amplification factor and the emitting area calculated from the slope and the ordinate intercept of a FN plot using the approximated $v(y) = 0.95 - y^2$ and $t^2(y) = 1.1$, the differences are within 1.2% and 19.1% for the field amplification factor and the emitting area, respectively.

Five of the twenty-four experimentally measured $I(V)$ curves (dots) together with their FN fits (solid lines) are plotted in Fig. 2.18 for separation distances s = 1.46, 1.98, 5.10, 8.74, and 13.43 μm. Each curve consists of two distinct regions that are distinguished by changes in the first derivative of the data. In the first region, the slope is nearly flat and the emission current is below 60 pA due to the minimum resolution for a gain setting of 10^7 V/A on the transimpedence amplifier. A second region above 60 pA in the $I(V)$ data follows the FN theory well as indicated by the curve fits in Fig. 2.18 and also by the straight lines plotted in the FN coordinates in Fig. 2.19.

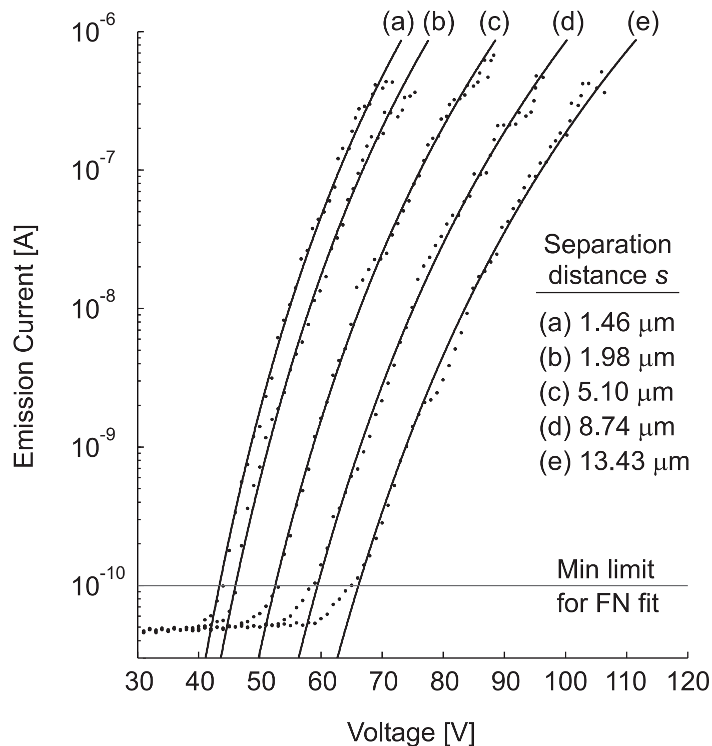

Figure 2.18: $I(V)$ characteristics of the CNT field emitter shown in Fig. 2.11(b) at five separation distances. Solid lines are Fowler-Nordheim (FN) fits.

The $I(V)$ curves shift leftwards with decreasing separation distance s, and the amount of shift between successive $I(V)$ curves increases with diminishing separation distance s. These trends are due to the rapid rate of change (increase) in the applied electric field (V/s) at small separation distances and the relatively slower change (decrease) in the field amplification factor λ. Hence, less voltage is necessary to establish a sufficient electric field at the tip of the CNT to produce electron emission. Similar observations were reported in prior studies with a sharp tungsten emitter by Olson *et al.* [92] and with a CNT emitter grown on a silicon tip by Minh *et al.* [37].

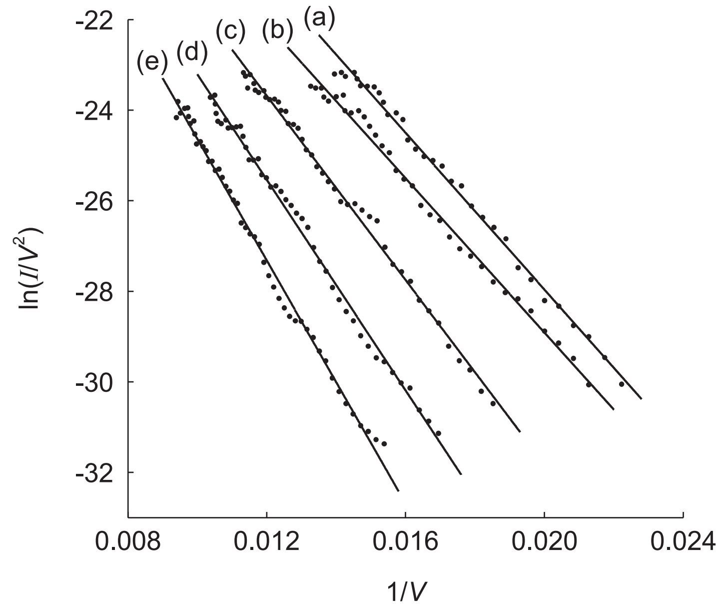

Figure 2.19: FN plots of the $I(V)$ curves shown in Fig. 2.18.

A turn-on voltage V_{to}, which is the voltage necessary to produce 1 nA of emission current, was also determined for each separation distance s. The dependence of emission on separation distance s is further evidenced by the turn-on voltage V_{to} shown in Fig. 2.20. As the separation distance s decreases from 13.43 to 1.46 μm, the turn-on voltage decreases from about 74 V to 48 V and the applied turn-on field (V_{to}/s) increases from 5.2 to 33.3 V/μm, as shown in Fig. 2.21, inferring a diminishing field amplification factor λ. The shape of the curve is similar to the numerical result of

Edgcombe *et al*. [76], the experimental result of Boyle *et al*. [93], and the experimental result of Young *et al*. [12] using the topografiner.

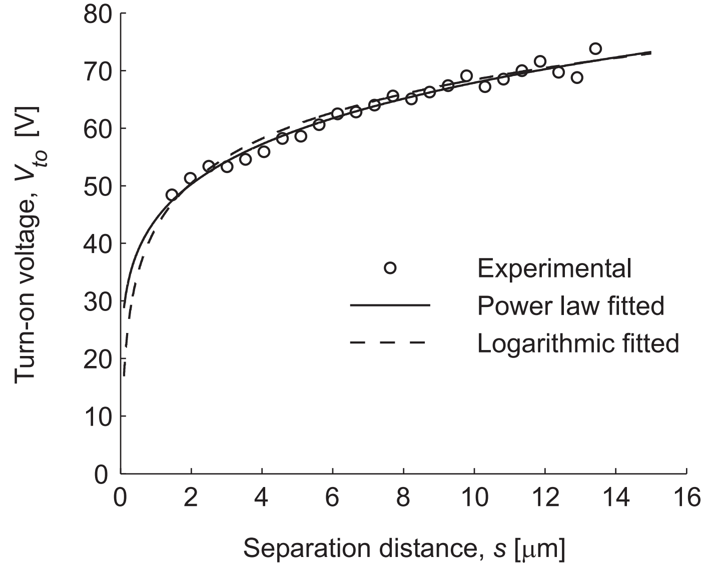

Figure 2.20: Turn-on voltage as function of separation distance.

Both power and logarithmic relations were considered as prospective empirical curves since they both suggest that V_{to} approaches zero and the derivative of V_{to} increases rapidly for very small gaps. The logarithmic relation was used for emitters described by the hyperbolic model [12]. However, the CNT tip is definitely not hyperbolic, and it was found that the power law fits the data better. Therefore, the turn-on voltage V_{to} as a function of separation distance s was fitted to a power law of the form $V_{to} = as^b$.

At small separation distances, the derivative of the data is high, and it decreases to a nearly constant value at larger distances. These results appear to fall in the transition region where the slope changes. The empirical power function, relating V_{to} [V] to the separation distance s [μm], obtained from the best-fit curve is $V_{to} = 44s^{0.19}$. Despite the reduction in turn-on voltage, the turn-on field at the CNT tip $(\lambda V_{to}/s)$ remains unchanged at about 3.7 V/nm for all the separation distances. This value falls in the lower range of the typical electric field strengths (3 to 6 V/nm) necessary for electron field

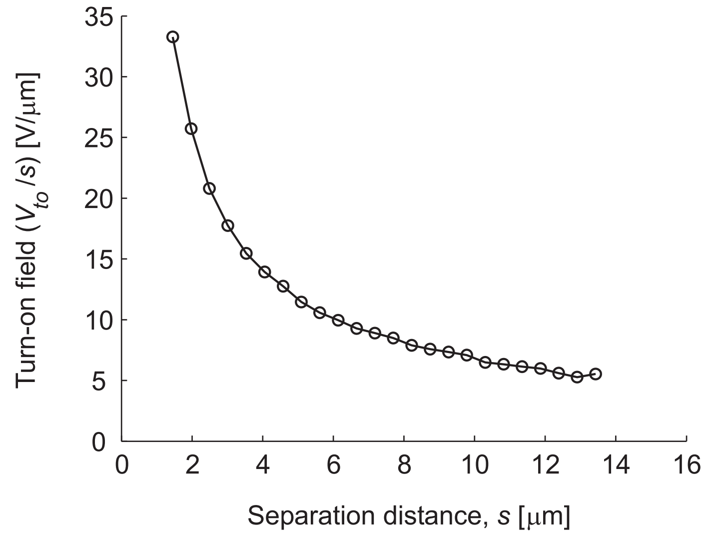

Figure 2.21: Turn-on field as function of separation distance.

emission.

The field amplification factor λ is the magnification of the applied electric field (V/s) at the tip of an emitter due to the geometry of both electrodes and their separation. The amplification factor λ is independent of the applied voltage V and the material of the emitter, but it depends strongly on the separation distance s and the geometry of both electrodes due to the concentration of the electric field. As illustrated in Fig. 2.22, the field amplification factor λ decreases nonlinearly from 680 to 110 with decreasing separation distance s. The field amplification factor λ decreases by about 6 times as the separation distance s decreases from 13.43 to 1.46 μm. As shown later in Section 2.6.2, these values are about an order of magnitude greater than that when using a sharp tungsten tip emitter without a CNT attached.

After fitting the data to the modified Miller equation, Eq.(2.30), the empirical relation between λ and s [μm] is determined to be $\lambda = 2361s/(s + 32.8) + 1$. This suggests that as s becomes much larger than the effective height h of the emitter, which is determined to be 32.8 μm, the field amplification factor λ approaches λ_∞ = 2361. Whereas, when s becomes much smaller than the height h of the emitter, the field amplification factor λ approaches unity. The field amplification factor λ therefore varies between the

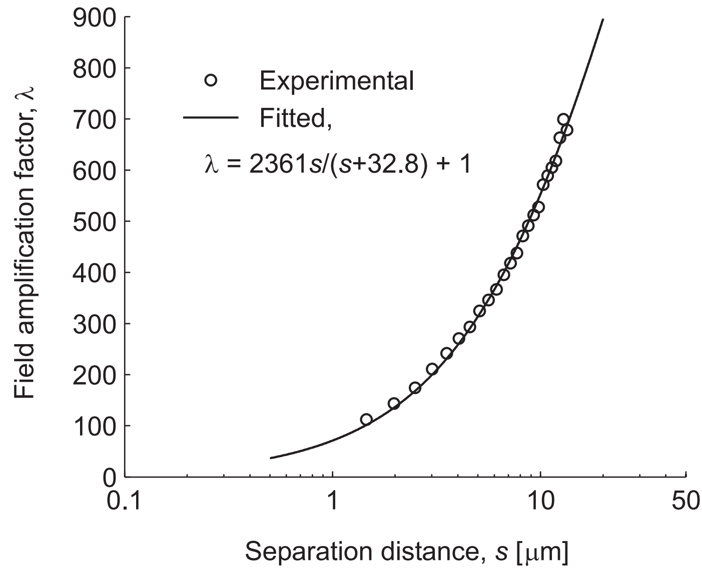

Figure 2.22: Field amplification factor as function of separation distance.

asymptotic values of unity and λ_∞ over the entire range of the separation distance s. The experimental data covers a relatively small range of separation distance s between 1.46 and 13.43 μm, which is smaller than the height h of the emitter (32.8 μm), thus the overall behavior of the field amplification factor λ over a large range of s could not be observed. Nevertheless, the empirical model fits the data well for the given range of s as shown in Fig. 2.22 and it is believed that the modified Miller equation is a reasonable empirical model to describe the behavior of λ over a large range of s (see Section 2.3).

The effective emitter height h of 32.8 μm, which is much greater than the protruding length of the CNT (2.1 μm), indicates that the shape of the tungsten tip also plays a significant role in enhancing the electric field at the tip of the CNT. If the end of the CNT is assumed to be closed with hemispherical surface, using the effective emitter height h = 32.8 μm and r = 30 nm (CNT tip radius), λ_∞ is determined to be about 650, which is about 3.6 times smaller than the value obtained by fitting with the modified Miller equation. This means that the end of the CNT is not closed. Such a large λ_∞ indicates that the CNT may have an irregular or opened end. In fact, it has been demonstrated experimentally [25] and computationally [94] that an opened CNT produces a greater

electric field enhancement than that of a closed CNT.

The trend of the field amplification factor λ is compared with that of Bonard *et al.* [44], who reported the dependence of the field enhancement factor γ on the distance $d = s + h$ for his CNT emitter using a scanning anode technique. It was found that the field enhancement factor γ increases from 230 to 460 and the turn-on voltage decreases from 185 to 47 V as the distance d decreases from 5.0 to 0.06 μm. Excellent agreement can be observed in the reduction of the turn-on voltages with the decreasing separation distance s. But, the trends of the field amplification factor λ and the field enhancement factor γ are contradictory. This contrast in the trends initially appears anomalous, but it is explained by considering the two different approaches [74], discussed in Section 2.3, for specifying the distance between the anode and cathode. Bonard *et al.* [44] used the distance d between the planar anode and the planar substrate of the cathode (emitter) and the corresponding relation $F = \gamma V/d$. Therefore, the enhancement factor γ should increase rapidly towards infinity as the separation s approaches zero or d approaches h. For our data, the electric field at the tip is $F = \lambda V/s$. Therefore, the amplification factor λ should decrease and approach unity as s approaches zero.

The trend of the field amplification factor λ agrees well with the computational work by Edgcombe *et al.* [76] and the earlier experimental work by Boyle *et al.* [93], who reported on the field emission from a pair of crossed tungsten wires 0.75 mm in diameter prior to the electrical breakdown. This trend is further supported by the recent experimental work of Sim *et al.* [47], who reported on the field emission from a single carbon nanofiber over a range of separation distances between 20 nm and 5.5 μm. Sim *et al.* [47] also verified that the modified Miller equation is a very reasonable empirical model for describing the behavior of the field amplification factor λ, which varies with the separation distance s over a large range of values. Unfortunately, the values of the field amplification factor λ and turn-on voltage V_{to} cannot be correlated directly due to the differences in the size and geometry of the electrodes. Nevertheless, the behaviors for how λ and V_{to} vary with the separation distance s remain the same.

The effective emitting area A_{eff}, on the other hand, is much more difficult to assess

than the field amplification factor λ. From the FN fitting, the values of the effective emitting area were found to vary between 20 and 350 nm^2. This substantial variation in the emitting area A_{eff} is probably due to its high sensitivity on the variability of $I(V)$ measurements, which results mainly from fluctuation in the emission current [95]. The current fluctuation is attributable to transient variation in the work function caused by adsorption and desorption of residual gas atoms on the CNT tip.

The vacuum pressure of 10^{-8} Torr means that roughly a monolayer of residual gas atoms forms on the emitter surface about every minute or less [96]. With this transient adsorption and desorption, the work function fluctuates between the work function for a clean surface (5 eV for carbon) and a lower work function due to tunneling through an adsorbed layer. The work function for the CNT was asummed to be 4.7 eV, which is slightly lower than that of carbon [66], and the calculated effective emitting area A_{eff} resulting from this assumption appears reasonable. It is believed that the mean value of A_{eff} is a better estimate for the actual effective emitting area than the individual values determined from each $I(V)$ curve. The mean of the twenty-four values for A_{eff} is determined to be 106 nm^2.

The emission current density at the tip of the CNT was calculated using the mean effective emitting area. The calculated current density is plotted against the local electric field $(\lambda V/s)$ at the tip of the CNT in Fig. 2.23. The current density follows the FN theory well for the electric fields between about 3 and 5 V/nm, which correspond to current densities of about 10^5 and 10^9 A/m^2, respectively. For electric fields larger than 5 V/nm, a slight saturation in the current density is noticeable. Clearly from Fig. 2.23, the tip of the CNT reaches a maximum current density of about 10^{10} A/m^2 during the field emission experiments. This value of current density is two orders of magnitude lower than the reported current density of 10^{12} A/m^2 needed to cause field evaporation of atoms from the end of the nanotube [97]. Therefore, no damage to the tip of the CNT is to be expected.

In a collabration work with Sanchez *et al.* [98], the CNT emitter was modeled as a nanotube with an opened end having outer diameter of 60 nm and protruding 2.1 μm directly from the tungsten tip. The computational results correlate well with the

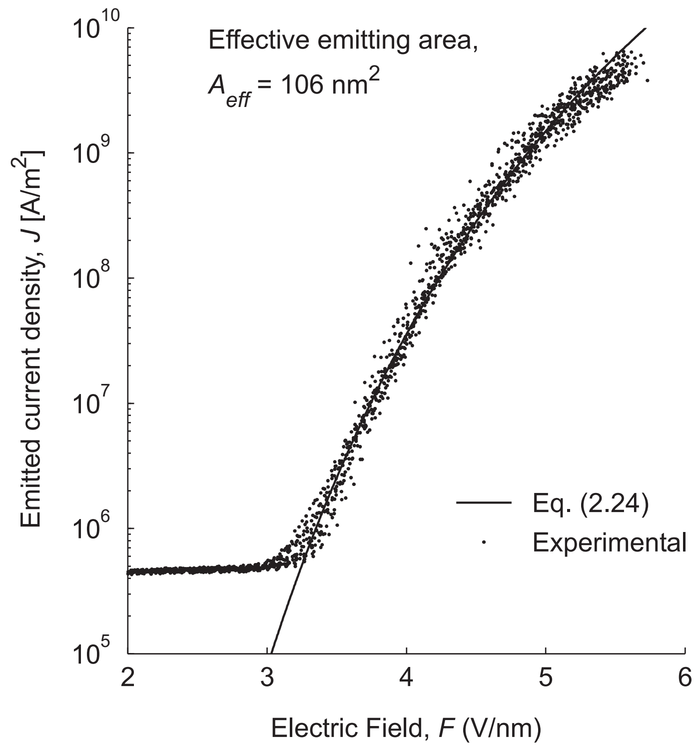

Figure 2.23: Current density versus local electric field at the tip of the carbon nanotube.

experimental results when the wall of the CNT is about 1.6 nm thick. This means that the end of the CNT consists of five walls, considering that the inter-wall distance of a multiwalled CNT is 0.34 nm [99, 100]. The field amplification factor at distant field for an opened CNT with a wall thickness of w can be calculated using the empirical relation: $\lambda_\infty = 0.62h/r + 0.14h/w + 7$ [94]. Here, h and r are the height and the outer radius of the emitter, respectively. According to Kokkorakis *et al.* [94], when the CNT wall becomes very thin (i.e., $w \ll r$), the ratio h/r will be irrelevant since the equipotential lines bend completely around the walls and λ_∞ can be determined exclusively by the ratio h/w. Thus, λ_∞ is determined to be 2870. This value is much closer ($\sim$ 1.2 times larger) to the experimental λ_∞ compared to that of a closed end ($\sim$ 3.6 times smaller).

2.6.2 Sharp Tungsten Field Emitter

This section presents a field emission study conducted for a sharp tungsten tip (without a CNT attached). The sharp tungsten field emitter used in the experiments is shown in the scanning electron micrograph of Fig. 2.7(c). Eleven sets of $I(V)$ data were measured at electrode separation distances s between 0.13 and 5.35 μm. The measured $I(V)$ curves (dots) together with their FN fits (solid lines) are plotted in Fig. 2.24 for separation distances of s = 0.13, 0.65, 1.17, 1.70, 2.22, 2.74, 3.26, 3.79, 4.31, 4.83, and 5.35 μm. Clearly, the $I(V)$ data follows the FN theory well as indicated by the curve fits in Fig. 2.24. The $I(V)$ curves shift leftwards with decreasing separation distance s, similar to those of a CNT field emitter, and the amount of shift between successive $I(V)$ curves increases with diminishing separation distance s.

Figure 2.25 shows that the turn-on voltage V_{to} decreases from 524 to 207 V as the separation distance s decreases from 5.35 to 0.13 μm. The turn-on voltage V_{to} decreases significantly when the separation distance s becomes smaller than 2 μm. The applied turn-on field (V_{to}/s), on the other hand, increases significantly from 98 to 1550 V/μm as the separation distance s decreases from 5.35 to 0.13 μm as shown in Fig. 2.26 inferring a disminishing field amplification factor. Because tungsten tips exhibit a hyperbolic shape [12], the turn-on voltage V_{to} as a function of separation distance s was fitted to a logarithmic relation of the form $V_{to} = a\ln(bs+1)$ such that V_{to} vanishes as

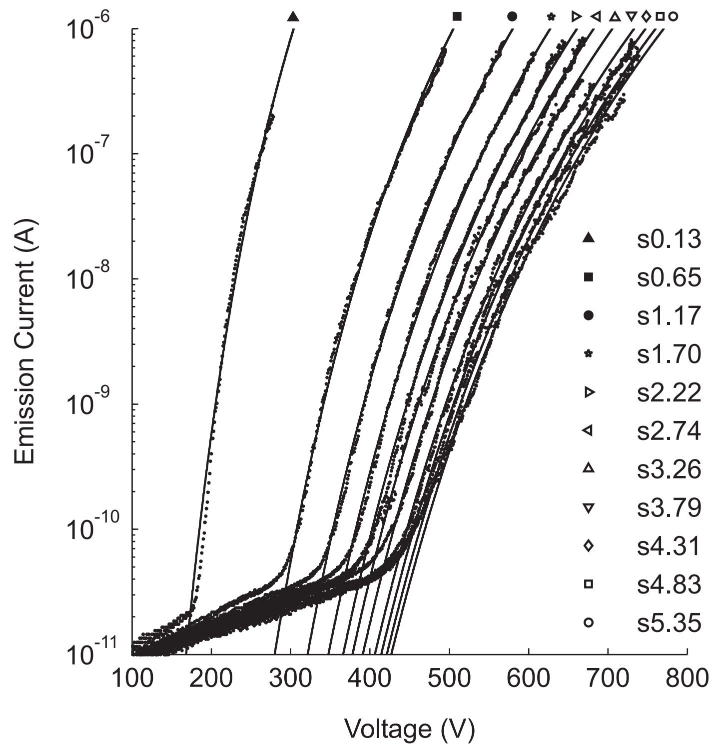

Figure 2.24: $I(V)$ characteristics of the sharp tungsten emitter shown in Fig. 2.7(c) at eleven separation distances s = 0.13, 0.65, 1.17, 1.70, 2.22, 2.74, 3.26, 3.79, 4.31, 4.83, and 5.35 μm.. Solid lines are Fowler-Nordheim (FN) fits.

s approaches zero. The empirical logarithmic function relating V_{to} [V] to the separation distance s [μm] was obtained to be $V_{to} = 85.9 \ln(82.1s + 1)$.

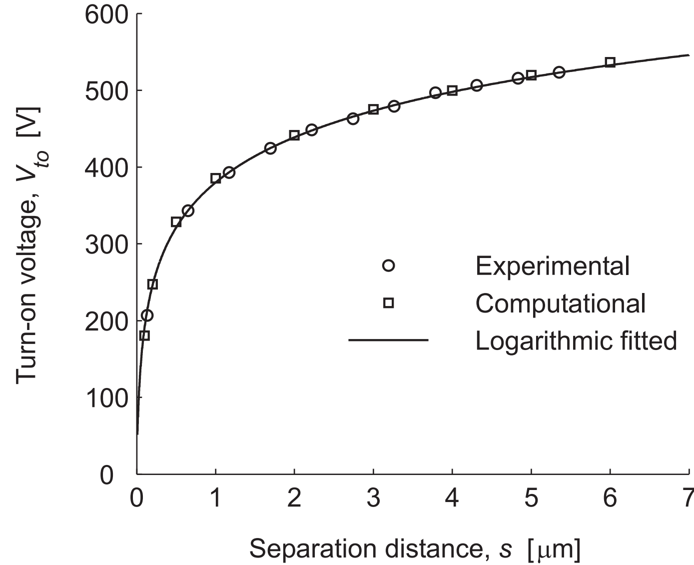

Figure 2.25: Turn-on voltage as function of separation distance.

The values of field amplification factor λ and effective emitting area A_{eff}, at each of the separation distances s, were extracted using the same nonlinear least squares curve fitting technique that fits the FN equations to each of the measured $I(V)$ curves. Figure 2.27 shows the extracted field amplification factor λ as a function of the separation distance s. The field amplification factor λ decreases nonlinearly from 33.6 to 2.1, a reduction factor of 16 times, as the separation distance s decreases from 5.35 μm to 0.13 μm. These values of field amplification factor λ are ten times smaller than those of the CNT field emitter (as discussed in the previous section) for separation distance s varying in between 1.0 and 5.5 μm. A value of λ equal to 2.1 at separation distance s of 0.13 μm clearly indicates that λ approaches unity as s becomes very small. This also means that the geometry of the electrodes resembles that of two parallel plates with no field enhancement. The mean effective emitting area A_{eff} is determined to be 420 nm^2.

After fitting the data to the modified Miller equation, the empirical relation between

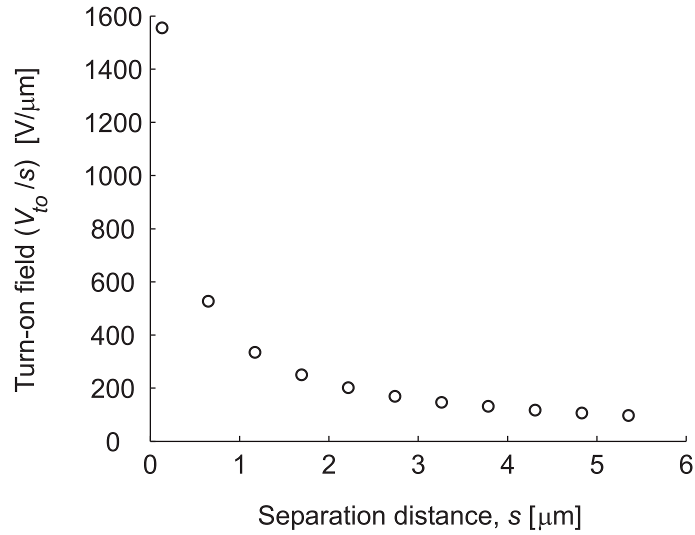

Figure 2.26: Turn-on field as function of separation distance.

λ and s [μm] is determined to be $\lambda = 150s/(s + 19.6) + 1$. From the data in Fig. 2.27, it is clear that the modified Miller equation fits the data well, and it yields the effective height h of the emitter and the field amplification factor λ_∞ at distant field to be 19.6 μm and 150, respectively. The behavior of how the field amplification factor λ varies with separation distance s is clearly visible in the region where s is less than 5.5 μm.

Despite the dependence of turn-on voltage V_{to} and field amplification factor λ on separation distance s, the turn-on field $(F_{to} = \lambda V_{to}/s)$ at the tip of the sharp tungsten emitter remains unchanged at about 3.3 V/nm for all the separation distances. This is the field strength needed to produce 1 nA of emission current from the tungsten tip. It is slightly less than 3.7 V/nm for a CNT emitter because the work function of tungsten (4.5 eV) is slightly slower than that of CNTs (4.7 eV).

The values of field amplification factor λ and turn-on voltage V_{to} are also computed using electrostatic finite element analysis (FEMLAB software) for separation distances s = 0.1, 0.2, 0.5, 1.0, 2.0, 3.0, 4.0, 5.0, and 6.0 μm. The tip of the emitter was assumed to be hemispherical with tip radius r equal to 91 nm. A 2D axisymmetric model of the sharp tungsten emitter (cathode) and the metal coated fiber (anode) was created for the finite element analysis as shown in Fig. 2.28. The geometry of the sharp tungsten

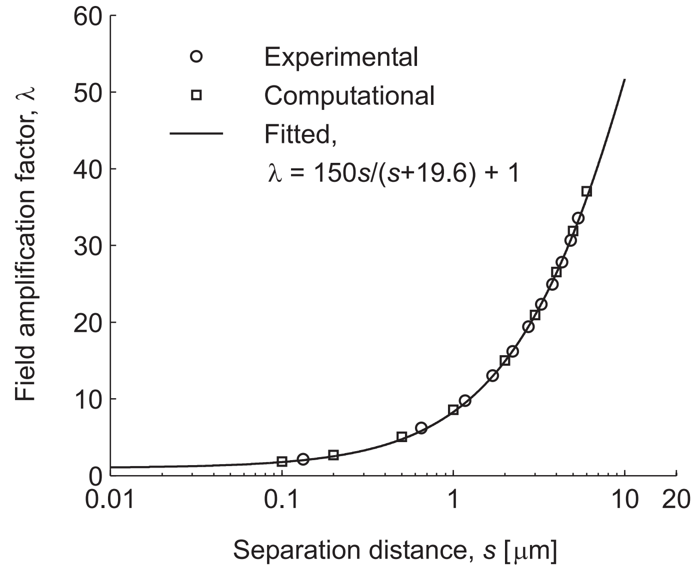

Figure 2.27: Field amplification factor as function of separation distance.

emitter was approximated from the actual image of the emitter shown in the scanning electron micrograph of Fig. 2.7(c).

The values of λ are plotted in Fig. 2.27, and it is clear that they correlate well with the experimental data. Using these values of λ and F_{to} equal to 3.3 V/nm, the turn-on voltage V_{to} can be determined from $V_{to} = F_{to}s/\lambda$ for each of the separation distances s. The values of V_{to} are plotted in Fig. 2.25, and they also correlate well with the experimental data. The field amplification factor λ_∞ at distant field can be determined from Eq.(2.31). Using effective emitter height h = 19.6 μm and tip radius r = 91 nm, λ_∞ is determined to be 152, which is in excellent agreement with the value obtained from the fitting using the modified Miller equation.

2.7 Chapter Summary

Using the experimental and computational methods developed in this chapter, field emission from an individual CNT or an ultra-sharp tungsten field emitter can be characterized as a function of the applied voltage and the separation distance at small separation distances. This was demonstrated using a technique that employs an ap-

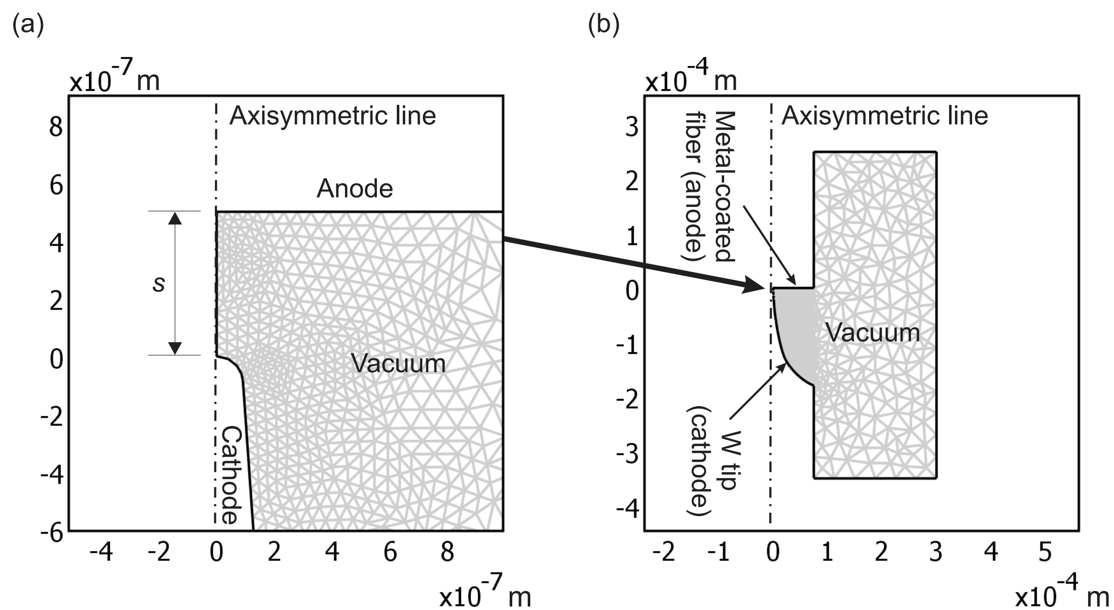

Figure 2.28: Axisymmetric model of the sharp tungsten emitter (cathode) and the metal coated fiber (anode).

paratus to precisely adjust the separation with respect to a datum distance established between the tip of the emitter and a metalized optical fiber. Sets of $I(V)$ data measured at various separation distances were fitted to the Fowler-Nordheim equation to determine how the field amplification factor and effective emitting area vary with the separation distance. It was found that both the field amplification factor and turn-on voltage decrease as the separation distance decreases. It was also found that the dependence of the field amplification factor is empirically well modeled by the modified Miller equation.

The experimental technique described and demonstrated in this chapter enables the study of field emission from 1D nanostructures at small separation distances. The approach is an improvement over other techniques, such as the scanning anode approach especially for studying field emission from individual CNT, since the separation is controlled more precisely over a larger range, the electric field at the CNT tip is not affected by neighboring CNTs, and the anode is a flat to within a few nanometers. Because of the high sensitivity to separation distance, it is essential to detect the surface

of the anode and establish a home position prior to conducting $I(V)$ measurements.

It was also found that field emission current on the order of a few hundred nanoamperes can be easily obtained at separation distances ranging from sub-micrometer up to a few micrometers. These emission currents are sufficient for most e-beam lithography. The voltages needed to create sufficient electric fields for field emission were found to be a few times lower when a CNT is attached to the sharp tungsten tip.

Chapter 3

Piezoelectric Linear Motor as Coarse Positioner for Tip-Sample Approach

3.1 Introduction to the Chapter

This chapter presents the design and operation of a coarse positioner called piezoelectric linear motor, which is one of the key components of the instrument for tip-sample approach. The performance of the instrument depends on many aspects of the piezoelectric linear motor such as mechanical rigidity, thermal stability, and smoothness of motion. A new method for measuring the motion characteristics and the thermal stability of the piezoelectric linear motor is presented. The chapter begins with a review of three popular coarse positiners used today.

3.2 Background

Piezoelectric actuators are electro-mechanical energy transducers in which they transform electrical energy into mechanical motion via the inverse piezoelectric effect [101]. The inverse piezoelectric effect, exhibited by particular dielectric materials such as lead zirconate titanate (PZT), produces a small amount of mechanical strain proportional to the magnitude of an applied electric field. The smallness of the strain enables positioning with extremely fine resolution. The piezoelectric phenomena is employed in a variety of actuators to produce displacements with extremely fine resolution (sub nanometer) over small travel ranges (several micrometers) [102]. The maximum travel range is limited by the dielectric strength and the maximum possible deformation of

the piezoceramic materials. The use of piezoelectric actuators can be found in many precision instruments and machines [103, 104, 105, 106, 107, 108, 109].

For longer travel range (several millimeters) applications, the same materials can be used as piezoelectric motors [110, 111, 112, 113, 114, 115, 116] to provide long range displacement via the repetition of many small steps (sub micrometer to several micrometers). Both piezoelectric actuator and motor are common in scanning probe microscopy (SPM) [114, 117]. The piezoelectric actuator, in form of tube scanner [118], scans the probe over the sample surface (or vice versa) in a rasterized pattern, while the motor brings the probe close to the sample surface.

There are three common approaches, as shown in Fig. 3.1, for using the repetition of small displacement of piezoelectric actuators to achieve long travel ranges. Figure 3.1(a) shows the stick-slip approach, which has been used in several instruments [110, 111, 119] because of its simplicity. Due to friction forces (stick), a slider is slowly translated a small step with one or more piezoelectric actuators, and then the piezoelectric actuators are rapidly jerked to its initial position. The slider does not move during the jerking motion due to its inertia (slip). The process is repeated to produce multiple steps. This approach is restricted to motion in a horizontal plane, unless a preload or clamping mechanism is used; for vertical motion, Renner *et al.* [111] preloaded the slider with a mechanical spring, and Mugele *et al.* [119] used a magnetic clamp. This approach is also used in the commercially available Picomotor screw-type actuators [120].

The second approach, applied in the commercially available Inchworm [112] motor, uses wormlike motion as illustrated in Fig. 3.1(b). A round tube in the center of the motor cyclically steps by clamping, extending, unclamping, and retracting the ring-shaped piezoelectric actuators. Since the translating tube is always clamped by at least one actuator, the motor can be used in any orientations. Step size as small as 1 nm has been achieved with a lever reduction mechanism incorpated into the motor [116]. A derivative of this approach is also used in the commercially available NEXLINE® linear motors from Physik Instruments (PI).

A third approach, as illustrated in Fig. 3.1(c), was originally described by Pan [113,

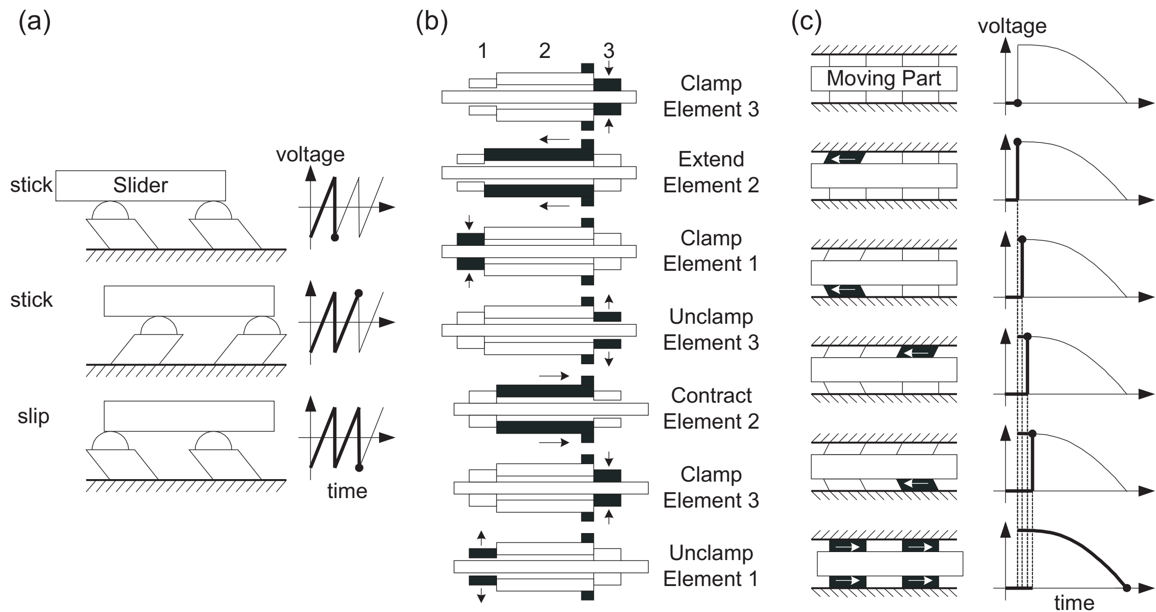

Figure 3.1: Common approaches for using small displacement of piezoelectric actuators to achieve long travel ranges, (a) stick-slip motion, (b) wormlike motion, and (c) walking motion.

117] and has since becomes a popular choice for low temperature instruments (cryostats) [121, 122, 123]. For conceptual illustration purpose, only four actuators are shown in the figure. In the actual motor, a sapphire prism is actually translated by six shear-mode piezoelectic actuators. A single step of the motor consists of a sequential-sliding action and a carrying action. In the sliding action, each of the six actuators consecutively slides backward along the surfaces of the prism. During the sliding of an actuator, the prism is held by the static friction forces at the remaining five actuators. In the carrying action, all six actuators simultaneously displace forward carrying the prism. There are several advantages to Pan's concept:

1. the motor can be symmetric, which improves thermal stability;
2. no external servo-control is required to hold the translating prism in position;
3. the motor can operate in any orientations;
4. preload can be adjusted to increase or decrease the holding force;

5. the motor can be designed to be stiff (rigid);

6. the motor can be compact; and

7. the motor can operate in vacuum environments and at low temperatures.

A variant of Pan's motor, as described by Gupta *et al*. [114], uses a single piezoelectric tube segmented into six sections instead of six shear-mode piezoelectric actuators. The motor works by crawling the segmented tube inside a prismatic shaped cavity. Although this motor is compact and cost effective, high preload forces are not possible since bending loads produce tensile stresses that can fracture and break the segmented sections of the piezoelectric tube.

Another variant of Pan's Motor, as described by Mariotto *et al*. [115, 124], replaces the translating sapphire prism with a sapphire rod. The study shows that the motor can operate in either inertial or frictional mode, depending on the transient actuation of the piezoelectric actuators. Gupta *et al*. [114] and Mariotto *et al*. [115, 124] measured their motors average step size as the ratio of travel distance to number of actuation steps using an optical microscope and a micrometer, respectively. These measurement methods cannot be used to characterize the motion per step and the variation in the step size of the motors cannot be determined.

3.3 Design and Construction

The piezoelectric motor differs from that of Pan [113], Gupta *et al*. [114], and Mariotto *et al*. [115, 124] in three fundamental ways: (1) the inclusion of a compliant suspension between the motor's supporting structure and piezoelectric actuators, (2) a lever reduction mechanism that provides for fine adjustment of the preload force via the compliant suspension, and (3) a radially symmetric structure made of materials with low coefficients of thermal expansion to greatly improve thermal stability. A detail view of the components and assembly of piezoelectric linear motor is given in Fig. 3.2(a) with a section cut-away.

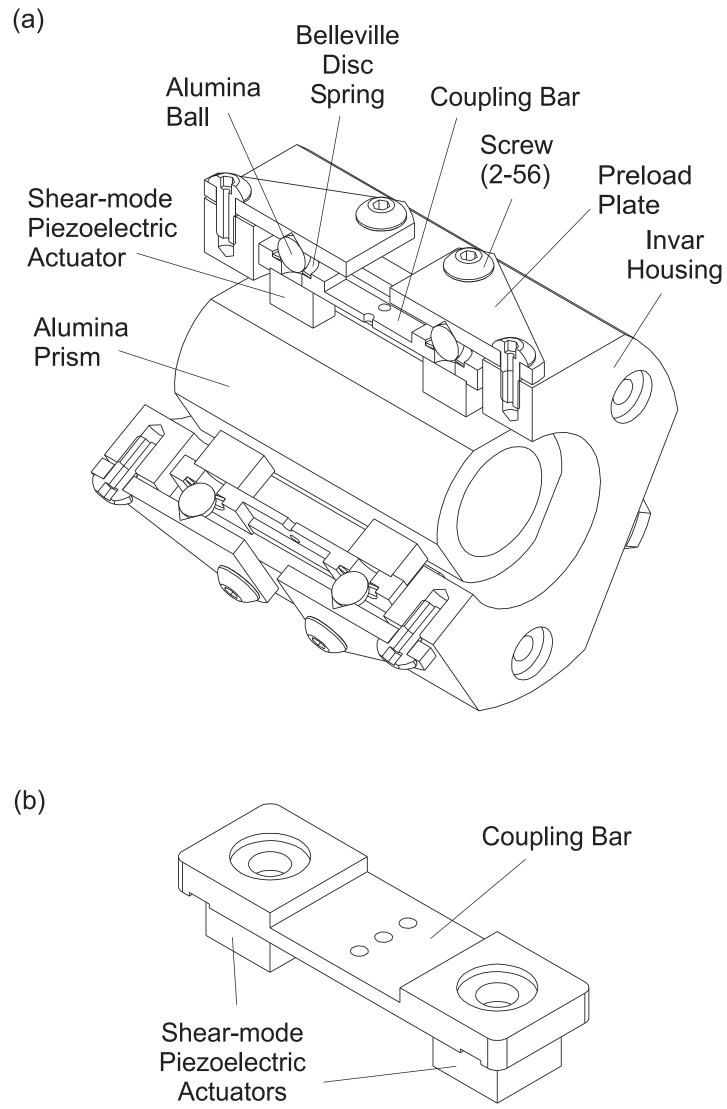

Figure 3.2: (a) Section cut-away view of piezoelectric linear motor and (b) driving mechanism.

The motor consists of six shear-mode piezoelectric actuators (PI: P-121.01) that clamp the alumina prism in position. Each actuator has two passive and two active shear-mode piezoelectric plates ($5 \times 5 \times 0.5$ mm) with alumina end plates. The alumina prism is machined from an alumina tube (outer diameter of 14.53 mm) with three equally angular spaced sides ground flat. The width of flat surfaces is 6.0 mm wide and the length of the prism is 30.5 mm long. The prism is the translating component located at the center and its axis coincides with the translation axis of the motor. The housing, machined from invar 36, contains three identical driving mechanisms and six identical preload mechanisms. The driving mechanisms are angularly spaced 120° apart, and they are hidden in the cut-out pockets on the invar housing. The alumina prism is kinematically constrained [125] from rotations due to its prismatic shape and the arrangements of the driving mechanisms, alumina balls, and preload plates. Such a design ensures very little sensitivity to temperature fluctuations in the ambient environment, which makes it ideal for applications where thermal stability is crucial.

Each driving mechanism, as shown in Fig. 3.2(b), consists of two shear-mode piezoelectric actuators bonded 17.78 mm apart near each end of a coupling bar. This prevents each individual actuator from rotating during operation. The linear motor has a travel range of about 7.6 mm, which is limited the length of the alumina prism. The adverse effects of manufacturing form errors such as the flatness and parallelism of the sliding surfaces on the alumina prism should be considered. The coupling bar is designed to be compliant in certain directions and rotations to account for these form and shape imperfections of the prism while providing a stiff structural link between the actuators.

On the other side of the coupling bar, where the shear actuators are located, are two circular pockets house the belleville disc springs that preload the alumina prism. Each preload mechanism consists of a belleville disc spring, an alumina ball, a triangular shaped preload plate, and three vented screws (size 2-56). The preload plate has a cone shaped pocket, centered with respect to the screws on one side of the plate for constraining the alumina ball. The preload force against the alumina prism is increased by tightening only one of these screws to increase the compression in the belleville disc

springs. This adjustment can be done independently for both front and rear preload planes.

In each preload plane, there are three preload mechanisms and thus three belleville disc springs are angularly spaced 120° apart. This arrangement ensures an equal preload force from all three radial directions whenever one of the preload plates is adjusted. The deflection due to the weight of the alumina prism can be neglected since it is much smaller than the preload force. The amount of the preload force P, given by Eqs. (3.1) to (3.3), generated by a belleville disc spring depends on its deflection δ due to a compressive load [126]. Other parameters in these equations include modulus of elasticity E, Poisson's ratio ν, disc thickness t, unloaded disc height h, inner radius a, outer radius b, and ratio of radii α = b/a.

$$P = \frac{C_1 C_2 E t^4}{(1-\nu^2)\, b^2} \tag{3.1}$$

$$C_1 = \frac{1}{2}\left(\frac{\delta}{t}\right)^3 - \frac{3h}{2t}\left(\frac{\delta}{t}\right)^2 + \left(1+\frac{h^2}{t^2}\right)\frac{\delta}{t} \tag{3.2}$$

$$C_2 = \pi\left(\frac{\alpha+1}{\alpha-1} - \frac{2}{\ln\alpha}\right)\left(\frac{\alpha}{\alpha-1}\right)^2 \tag{3.3}$$

The alumina ball that seats in between the cone shaped pocket of the preload plate and the belleville disc spring acts as a moving pivoting point and also improves the adjustment resolution of the preload force due to the lever reduction mechanism formed by the ball being centered with respect to the screws. The schematic of the lever reduction preload mechanism for a preload plane is illustrated in Fig. 3.3. The stiffness of the preload plate is 11.2 N/μm computed from finite element analysis (FEA). And, the axial stiffness of the actuator is 190 N/μm. Since they are much larger than the stiffness of the disc spring, the preload plate and the piezoelectric actuator are asssumed to be rigid bodies. An adjustment of δ_s at one of the screws will displace the ball by one third (δ_b=$\frac{1}{3}\delta_s$) because the lever reduction mechanism has a reduction ratio of $\frac{1}{3}$.

Since the preload forces produced by the disc springs are the same for a displacement of δ_b applied directly to one of the alumina balls, all three bellevile disc springs

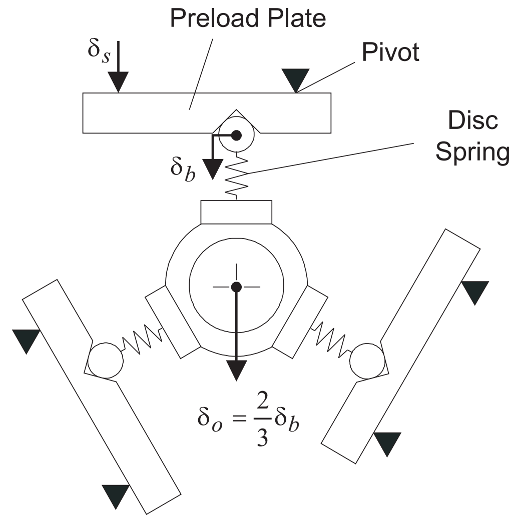

Figure 3.3: Schematic diagram of preload mechanism with lever reduction.

deflected equally. A displacement of δ_b at one of the alumina balls causes the axis of the alumina prism to displace by an amount of about $\frac{2}{3}\delta_b$. The deflection δ of all the belleville disc springs in the preload plane is then approximately one third the displacement of δ_b as given by Eq. (3.4).

$$\delta \cong \frac{1}{3}\delta_b \tag{3.4}$$

Thus, with the lever reduction mechanism, the deflection δ of the belleville disc springs for an adjustment of δ_s at one of the screws is given by Eq. (3.5).

$$\delta = \frac{1}{9}\delta_s \tag{3.5}$$

The preload force P generated by the disc spring for an adjustment of δ_s at one of the screws is then calculated from Eqs. (3.1) to (3.3) using the deflection δ in Eq. (3.5). Figure 3.4 shows the preload force generated by the disc spring for an adjustment of δ_s at one of the screws. The parameters of the belleville disc spring are listed in Table 3.1.

It is recommended [114] to adjust the preload forces of the motor such that they

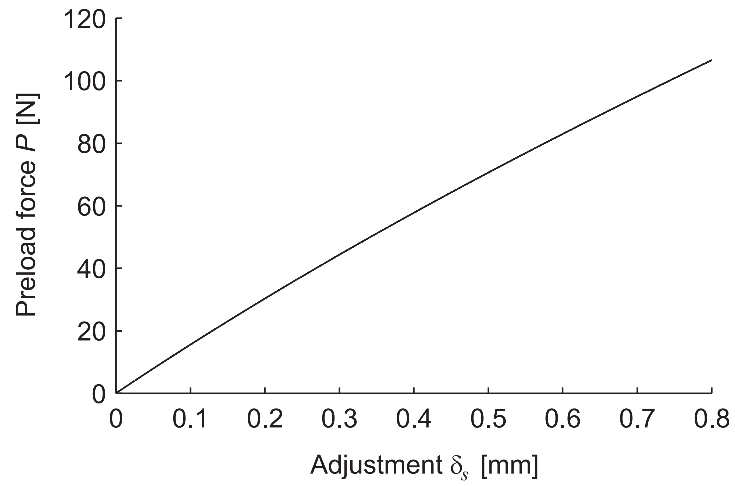

Figure 3.4: Preload force P generated by the disc spring for an adjustment of δ_s at one of the screws.

Table 3.1: Parameters of belleville disc spring

Modulus of elasticity, E	200 GPa
Poison's ratio, ν	0.3
Disc thickness, t	0.254 mm
Unloaded disc height, h	0.129 mm
Inner radius, a	1.270 mm
Outer radius, b	2.235 mm

are very nearly the same for both front and rear preload planes. The resolution in the adjustability of the preload force is about 1 N assuming that the 2-56 screw can be turned with an increment of 5°. The static holding force F_{hold} of the motor then equals the total friction force for all six of the preload forces P time the coefficient of static friction μ_s as given in Eq. (3.6).

$$F_{hold} = 6\mu_s P \quad (3.6)$$

The coefficient of static friction μ_s for alumina sliding on alumina in the prototype motor was measured experimentally to be 0.203 $\pm$ 0.018. It is recommended that the maximum shear load of the piezoelectric actuator not be exceeded. The maximum preload force of the disc spring is about 110 N, which is limited by the maximum allowable stress of about 2.75 GPa [126] at the inner boundary of the belleville disc springs. As a rule of thumb, a disc spring usually has useable range of up to 75% of its maximum deflection (flattened). For the disc spring used in this motor, the upper limit is at about 95 μm. The maximum frictional force is therefore 22 N, which is less than the maximum allowable shear load of 50 N for the actuator. This produces a theoretical maximum static holding force of about 135 N for this motor. The prototype of the piezoelectric linear motor is shown in Fig. 3.5.

3.4 Operation

The linear motor can operate in two modes: scanning mode and stepping mode. In scanning mode, all six shear-mode piezoelectric actuators clamping on the alumina prism shear simultaneously in phase without sliding. In stepping mode, each of the piezoelectric actuators is actuated rapidly and orderly in the reserve direction to cause it to slide along the surface of the alumina prism while the prism is held by the static friction forces at the remaining five actuators, and then simultaneously actuating all the actuators slowly (in phase) to carry the prism one step in the forward direction. A simplified conceptual illustration of this stepping mode is shown in Fig. 3.1(c) with only four actuators.

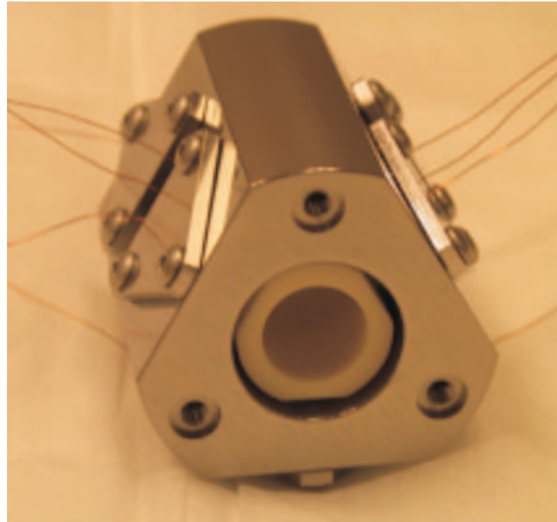

Figure 3.5: Photograph of the piezoelectric linear motor.

For stepping mode, this motor requires a special electronic circuit that can generate six synchronized output waveforms to drive the piezoelectric actuators. It would be very costly to use six high-voltage amplifiers to drive all the actuators. A common alternative [114] uses a transformer to amplify the 60 Hz alternating current (AC) power line signal and a variac to adjust the amplitude of the AC signal. The signal is then conditioned and split into six synchronized voltage outputs with an appropriate time delay in between them.

Although this alternative is rather cheap and simple, a drawback would be each consecutive voltage step applied to the actuator is always slightly lower in amplitude than the previous one. This may cause the sliding distance by each of the actuators to vary slightly. To avoid this problem, the voltage steps of the same amplitude shall be used. This is incorporated in the electronic circuit of the linear motor. Figure 3.6 shows the block diagram of the electronic circuit.

The first block of the circuit is the triangular waveform generator [127], which generates a 60 Hz triangular-wave signal with an amplitude of 1.22 V. External waveforms can be selected by meaning of switch SW1. For this work, the built-in signal generator is used. The output of the signal generator is fed to a voltage clipper [128] to clip the

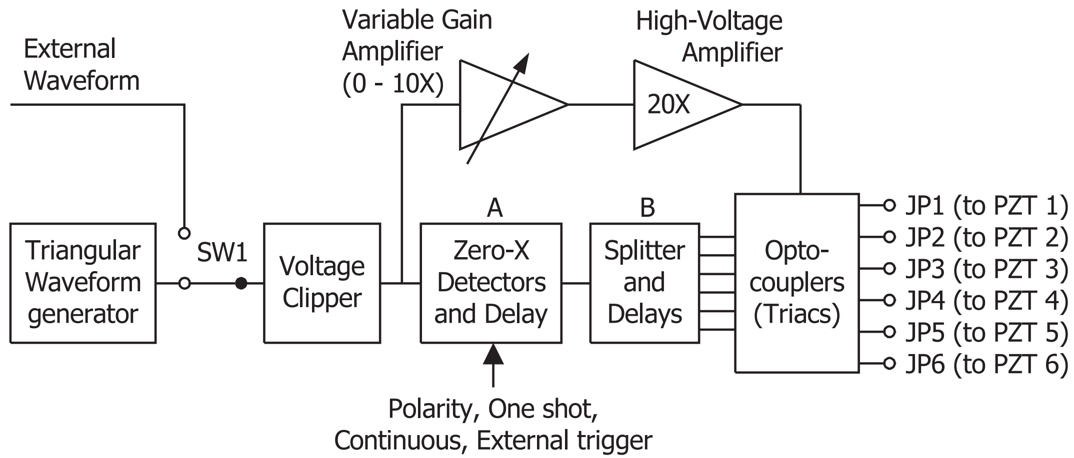

Figure 3.6: Block diagram of electronic circuit for the linear motor.

corners of the triangular-wave signal at +1 V and -1 V. The circuit diagram of the triangular waveform generator and the voltage clipper is shown in Fig. 3.7. The clipped signal is then fed to a variable gain amplifier and block A. At the variable gain amplifier, the clipped signal can be amplified up to 10 times by manually adjusting the gain of the amplifier. The output of the amplifier is furthered amplified by a 20 times gain high-voltage amplifier [129] before sending the amplified clipped signal to the inputs of six opto-couplers (triacs).

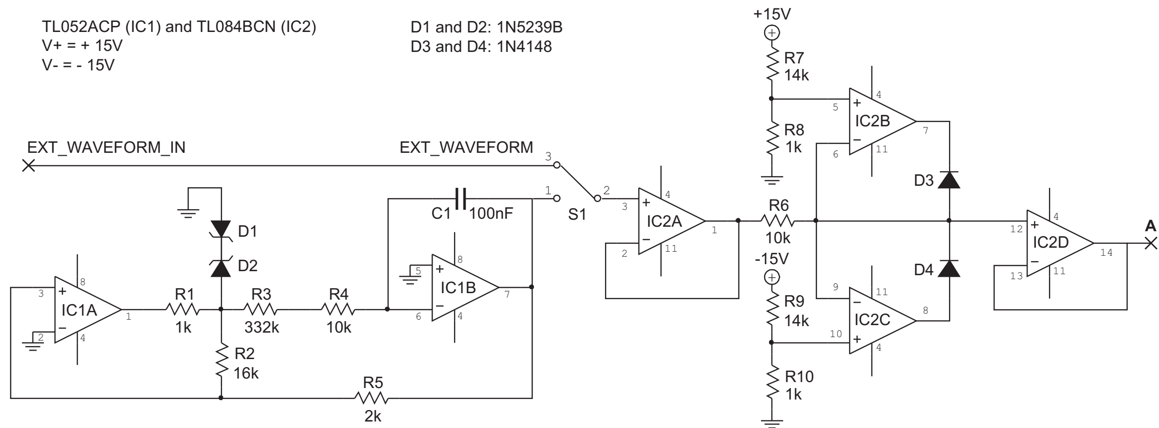

Figure 3.7: Circuit diagram of the triangular waveform generator and the voltage clipper.

At block A, user defined control settings such as the direction of motion (polarity) and the number of steps (one shot, continuous, or external trigger) of the motor can be selected. The zero-crossing of the clipped signal is performed by two comparators, one for each direction of motion. The outputs of the comparators are in square-wave signals with one of them inverted. The signals are then rectified to make a train of pulses (for multiple steps operation), of positive polarity only, corresponding to the rising edge of the square-wave signals. These pulses are shifted 16.67 ms apart, which is exactly equivalents to the period of the clipped signal or the cycle of the clipped signal. There will only be a single pulse (one step) for one shot operation. Each pulse is then delayed by 4.17 ms (a quarter-cycle of the signal) before sending it to block B. This time delay is to assure that the triacs are triggered in the appropriate quadrant of the signal arriving at the triacs. Figure 3.8 shows the circuit diagram of Block A as described above.

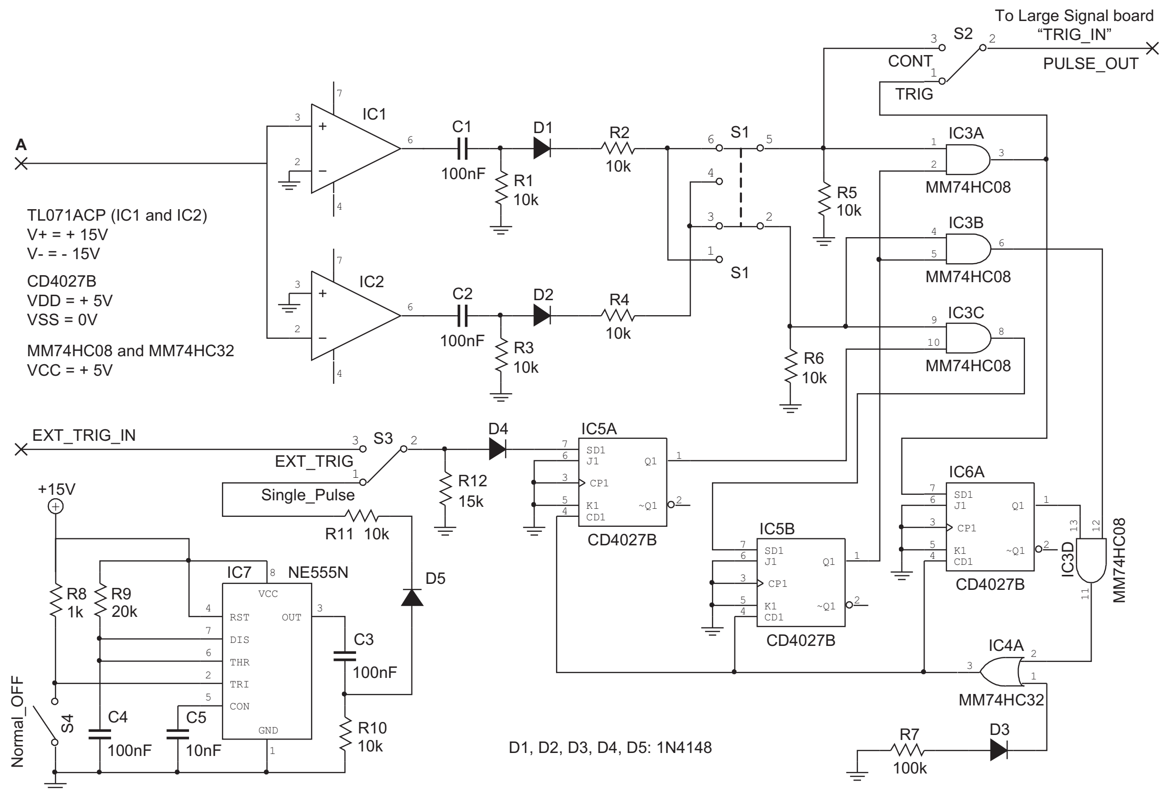

Figure 3.8: Circuit diagram of Block A.

At block B, each incoming pulse passes through a series of time delays to produce six more pulses with each one of them orderly delayed by about 108 μs. The time delay is to assure that each piezoelectric actuator has enough time to complete the sliding before the next actuator is activated. These orderly delayed pulses also have a pulse width of 108 μs. The pulses are then used for triggering the triacs to produce the waveforms needed for the motor. Figure 3.9 shows the circuit diagram of Block B and the triacs.

Triac functions as a bidirectional electronic switch, which can conduct current in either direction when triggered. Once triggered, it continues to conduct until the current through it drops below a certain threshold value, such as at the end of a half-cycle of AC signal. Depending on the type of loads, the triac may turn off prematurely for capacitive load such as piezoelectric actuator before the end of a half-cycle. This is because the current required by the piezoelectric actuator depends on the transient of the driving signal. To prevent this premature cutoff, a resistive load, as shown by the 50kΩ power resistor in Fig. 3.10, is added in parallel with the piezoelectric actuator to assure that the current through the triac stays above the threshold value and only drops below it at the very end of the half-cycle. This makes the triac a very convenient switch since the output waveform is always uni-polar of either positive or negative polarity only. This is particularly crucial for the linear motor because the direction of motion is controlled by the polarity of the applied voltage. Figure 3.10 shows the waveform shaping at one of the triacs for both forward and backward motion.

Since the triacs are trigerred orderly, the outputs of the triacs are six synchronized waveforms as shown in Fig. 3.11(a). These uni-polar waveforms shown in Fig. 3.11(a) are applied to the piezoelectric actuators according to the order shown in Fig. 3.11(b), for moving the alumina prism one step in the forward direction. For motion in the backward direction, the polarity of the waveforms is reversed.

The linear motor can be modeled as a mass (alumina prism) supported on six parallel springs (piezoelectric actuators). The alumina prism is assumed to be rigid and the base (support) of the actuator is assumed to be fixed. All actuators are assumed to have the same displacement and stiffness. The motor can be simplified to a spring-

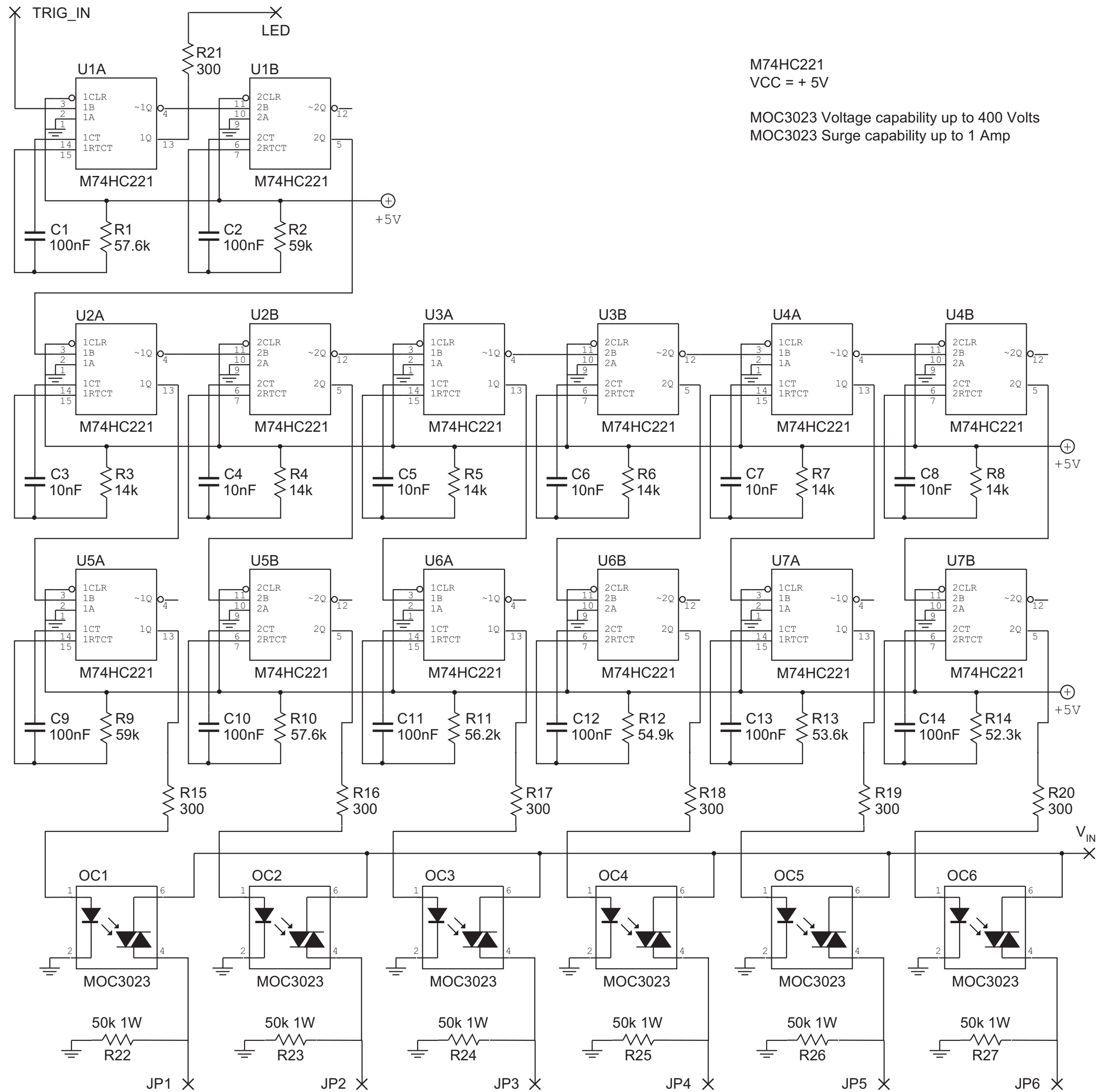

Figure 3.9: Circuit diagram of Block B and triacs.

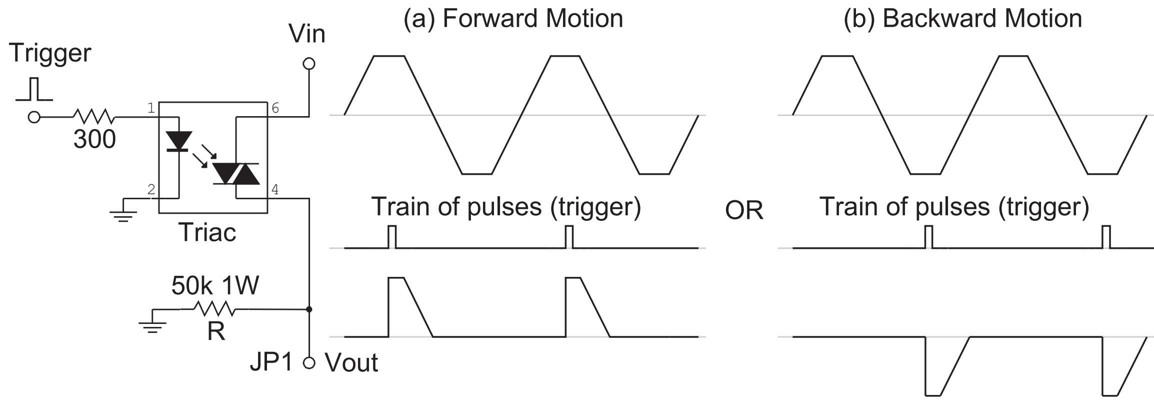

Figure 3.10: Schematic diagram of the bidirectional electronic switch and waveform shaping.

mass model as shown in Fig. 3.12.

The free or uncontrained displacement ΔL [nm], without any external restraints, of a shear-mode piezoelectric actuator with n active plates stacked in series for an applied voltage V [V] is given in Eq. (3.7) [130]. The parameter d_{15} [nm/V] is the shear-mode piezoelectric coefficient.

$$\Delta L = n d_{15} V \tag{3.7}$$

If all six piezoelectric actuators clamping on the alumina prism shear simultaneously in the same direction without sliding, the displacement of the prism is equivalent to the displacement of each individual actuator. The displacement of the actuator will be reduced if an external restraint (spring) is added to it. When a voltage is applied to one of the actuators, the alumina prism displaces by an amount of ΔL_p [nm] as given in Eq. (3.8), where, k_{pzt} [N/nm] is the stiffness of the actuator and k_s [N/nm] is the total stiffness of the remaining five actuators.

$$\Delta L_p = \Delta L \left(\frac{k_{pzt}}{k_{pzt} + k_s} \right) \tag{3.8}$$

$$k_s = 5 k_{pzt} \tag{3.9}$$

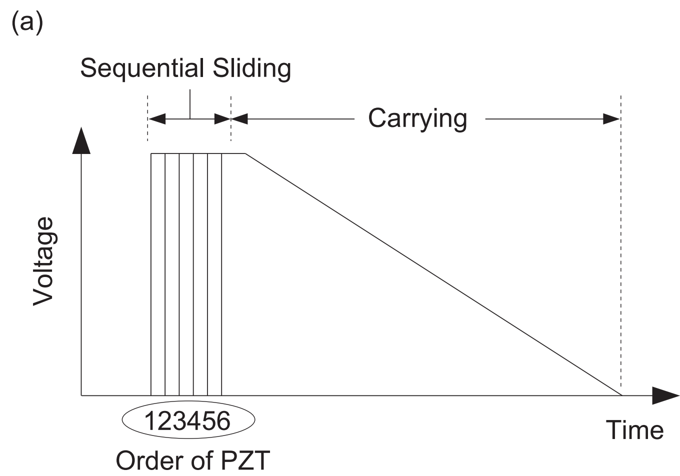

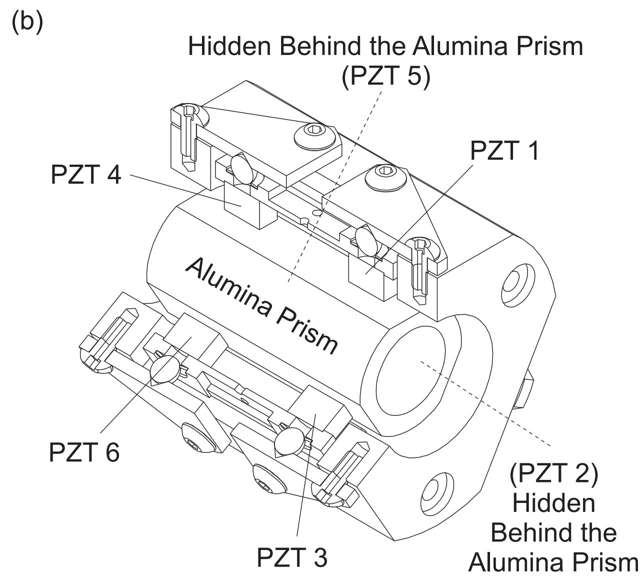

Figure 3.11: (a) Six synchronized waveforms used to move the alumina prism one step forward and (b) order of piezoelectric actuators.

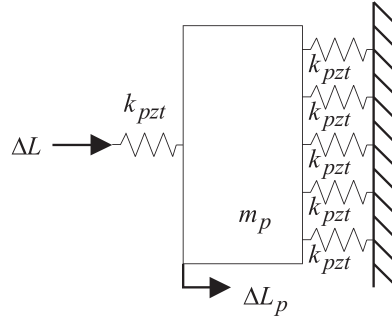

Figure 3.12: A simplified spring-mass model of the linear motor.

The free displacement of the prism reduces by an amount of ΔL_R as given in Eq. (3.10).

$$\Delta L_R = \Delta L - \Delta L_p \tag{3.10}$$

The lost displacement ΔL_R [nm], which is equal to $\frac{5}{6}\Delta L$, is caused by the stiffness of the remaining five actuators holding the prism. Work is done by the actuator to deform the remaining five actuators. Thus, the force generated by the actuator, F_{pzt} [N], is given in Eq. (3.11). This is the amount of force that exerts on the prism.

$$F_{pzt} = k_{pzt}\Delta L_R \tag{3.11}$$

If this force F_{pzt}, which is equal to $\frac{5}{6}k_{pzt}nd_{15}V$, exceeds the static frictional force F_s [N], given in Eq. (3.12), sliding occurs between the alumina end plate of the actuator and the alumina prism. Recall that μ_s is the coefficient of static friction, and P [N] is the preload force. Any variation in the preload forces acting on the actuators (for the motor oriented horizontally) is neglected since the weight of the alumina prism is only about 94 mN.

$$F_s = \mu_s P \tag{3.12}$$

The threshold voltage V_t [V] is the voltage that must be applied to the actuator to

generate a force equal to the static frictional force F_s. It can be obtained by equating Eq. (3.11) and Eq. (3.12). The relation between the threshold voltage V_t and the preload force P is given in Eq. (3.13). The physical parameters of the linear motor is listed in Table 3.2.

$$V_t = \frac{6\mu_s P}{5nd_{15}k_{pzt}} \tag{3.13}$$

Table 3.2: Physical parameters of the piezoelectric linear motor

Shear stiffness of actuator (FEA), k_{pzt}	0.135 N/nm
Coefficient of static friction, μ_s	0.203
Number of piezoelectric shear plates, n	2

The threshold voltage V_t obtained from Eq. (3.13) is the minimum voltage needed for a single actuator to slide on the alumina prism while held by the remaining five actuators. During sliding, the actuator becomes momentarily decoupled from the structure that forms the spring-mass system. This causes the force generation in the actuator to drop. However, the actuator will continue to exert a kinetic frictional force on the alumina prism. The sliding will eventually stall, forcing the actuator to couple back to the structure. Although the actuator slipped to a new position, the remaining force left in the actuator is still equal to the static frictional force (just like before sliding occured). Due the force-displacement relationship of the actuator pushing against a spring load, the remaining force left in the actuator would convert to a free displacement of ΔL_b [nm], as given in Eq. (3.14). This is the amount of displacement the actuator not able to slide on the alumina prism due to the static frictional force.

$$\Delta L_b = nd_{15}V_t \tag{3.14}$$

Similarly, this applies to the remaining five actuators. The sliding of the actuators on the prism eventually produces a reverse motion equals to Eq. (3.14). When the actuators move simultaneously forward (like the motion in scanning mode), the displacement of the prism is given in Eq. (3.7). Therefore, the motion per step ΔL_s [nm] of the linear

motor is given in Eq. (3.15).

$$\Delta L_s = \begin{cases} 0 & , \quad V \leq V_t \\ \Delta L - \Delta L_b & , \quad V > V_t \end{cases} \tag{3.15}$$

3.5 Experimental Setup

To characterize the performance of the linear motor, a noncontact capacitive displacement measuring system from Lion Precision was used. The system has a resolution of about 1 nm and the peak-to-peak noise of about 10 nm based on the default factory setting for high resolution. The peak-to-peak noise can further be reduced by setting the system to a lower bandwidth whenever a low noise and low speed measurement is required. The system measures the change of capacitance between a sensor (Lion Precision: C1-C) and a conducting target, which is mounted on the alumina prism of the linear motor. Changes in the capacitance are converted into output voltages by the sensor driver (Lion Precision: DMT 22). The sensitivities for high and low resolutions of the capacitive displacement measuring system are 2.54 μm/V and 12.7 μm/V, respectively. The dynamic ranges for high and low resolutions are 50.8 μm and 254 μm, respectively.

Three sensor arrangements were used depending on the direction of motion(s) being measured. The measurements were performed on the front side of the motor. Figure 3.13(a) shows the arrangement for axial motion measurement such as motion per step, linearity and also for calibrating the piezoelectric actuators of the motor. The sensor target, a small circular plate made of invar 36, is mounted on the alumina prism. The sensor holder for holding the displacement sensor is mounted on the motor housing. The axis of the displacement sensor must align with the axis of the motor to minimize the error due to Abbe's offset.

The arrangement in Fig. 3.13(b) was used for lateral motion measurements. The sensor target, shaped like a cubic also made of invar 36, is mounted on the alumina prism. Two displacement sensors orthogonal to each other are held by the sensor holder, which is mounted on the motor housing. The output of the displacement sen-

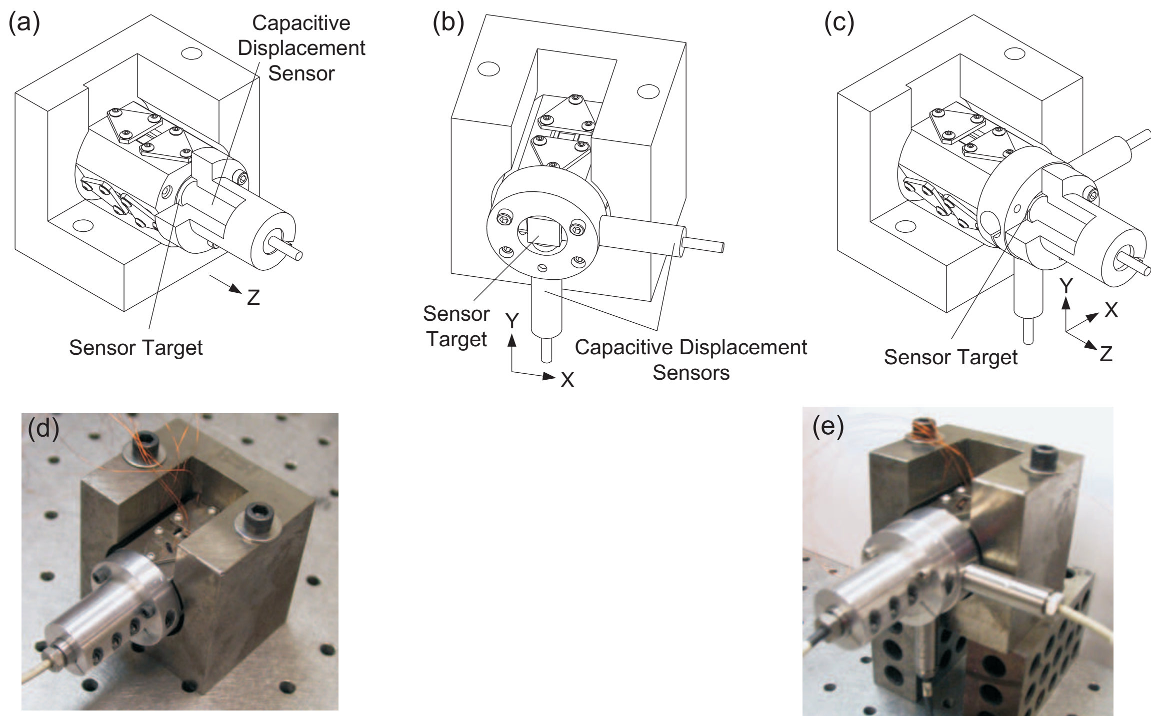

Figure 3.13: Arrangements for measuring the motion(s) in the (a) axial direction, (b) lateral directions, and (c) both axial and lateral directions. Photographs of experimental setups for (d) axial motion measurement and (e) axial and lateral motion measurements.

sor in the Y direction is inverted to be consistent with the coordinate system used in Fig. 3.13(b). The displacement sensors are placed 25.4 mm from the middle plane, between the front and rear preload planes, of the motor. For simultaneous axial and lateral motion measurements, the arangement in Fig. 3.13(c) with three displacement sensors can be used.

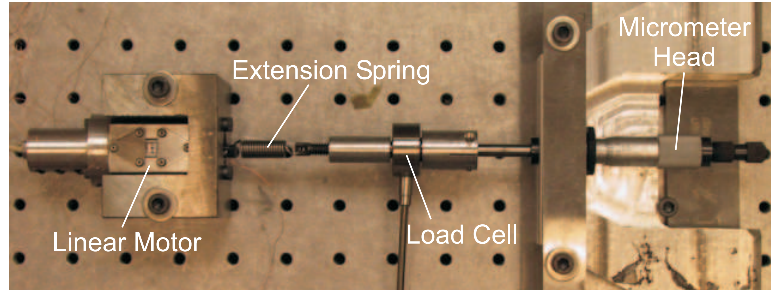

Figure 3.14: Photograph of the experimental setup for measuring the static holding force of the motor.

Figure 3.14 shows the experimental setup for measuring the static holding force of the motor. An extension spring anchored to the alumina prism is pulled by a micrometer head. The tension in the spring is adjusted until the alumina prism slipped while a load cell attached to the end of the micrometer head measures the tension in the spring. The measurement would require the axis of the prism to align with the axes of the load cell and the micrometer head. The load cell has a sensitivity of 88.35 N/V. The measured static holding force is then used to calculate the preload force applied on the alumina prism by using Eq. (3.6).

3.6 Calibration of Actuators

Piezoelectric materials show a considerable hysteresis [131] in open loop operation. The hysteresis exhibits the nonlinearity behavior in the displacement of a piezoelectric actuator. The nonlinearity is associated with the voltage dependent change in the piezoelectric sensitivity k_z [132, 133], which can be described fairly well by Eq. (3.16), where, k_0 is the small signal piezoelectric sensitivity and α is the rate of change in the

piezoelectric sensitivity with respect to a voltage sweep ΔV.

$$k_z = k_0 + \alpha \Delta V \tag{3.16}$$

Using the relations $k_z = nd_{15}$, $k_0 = nd_{15}^0$, and $\Delta V = nV$, where V is the applied voltage on each shear-mode piezoelectric plate and d_{15}^0 is the small signal shear-mode piezoelectric coefficient, Eq. (3.16) reduces to Eq. (3.17).

$$d_{15} = d_{15}^0 + \alpha V \tag{3.17}$$

From Eq. (3.17), the nonlinearity in the displacement of the shear-mode piezoelectric actuators is actually due to the voltage dependent change in the piezoelectric coefficient d_{15}. Since the shear displacement is independent on the dimensions of the shear-mode piezoelectric plate, the sensitivity k_z and the piezoelectric coefficient d_{15} are equivalent, which can be obtained experimentally. By fitting Eq. (3.7) to the measured displacement of the actuators using d_{15} given in Eq. (3.17), the values of d_{15}^0 and α can be obtained.

The piezoelectric coefficient d_{15} also varies slightly with the frequency and the waveform of the driving signal [131, 132]. It is therefore important to calibrate the actuators according to the 60 Hz driving waveform of the motor. The calibration of the actuators is performed in the scanning mode, where all actuators displace simultaneously in phase. The displacement of the alumina prism is then measured. Figure 3.15(a) shows the displacement of the actuators measured experimentally and the fitting using Eq. (3.7). The values of d_{15}^0 and α are determined to be 0.4949 nm/V and 9.611×10^{-4} nm/V^2, respectively. The small signal piezoelectric coefficient d_{15} agreed well with the manufacturer value of 0.5 nm/V.

Therefore, the relation between the piezoelectric coefficient d_{15} [nm/V] and the applied voltage V [V] is given in Eq. (3.18). The piezoelectric coefficient d_{15} calculated using Eq. (3.18) is plotted in Fig. 3.15(b).

$$d_{15} = 9.611 \times 10^{-4} V + 0.4949 \tag{3.18}$$

Substituting Eq. (3.18) and $n = 2$ into Eq. (3.7), one can obtain Eq. (3.19).

$$\Delta L = 1.9222 \times 10^{-3} V^2 + 0.9898V \tag{3.19}$$

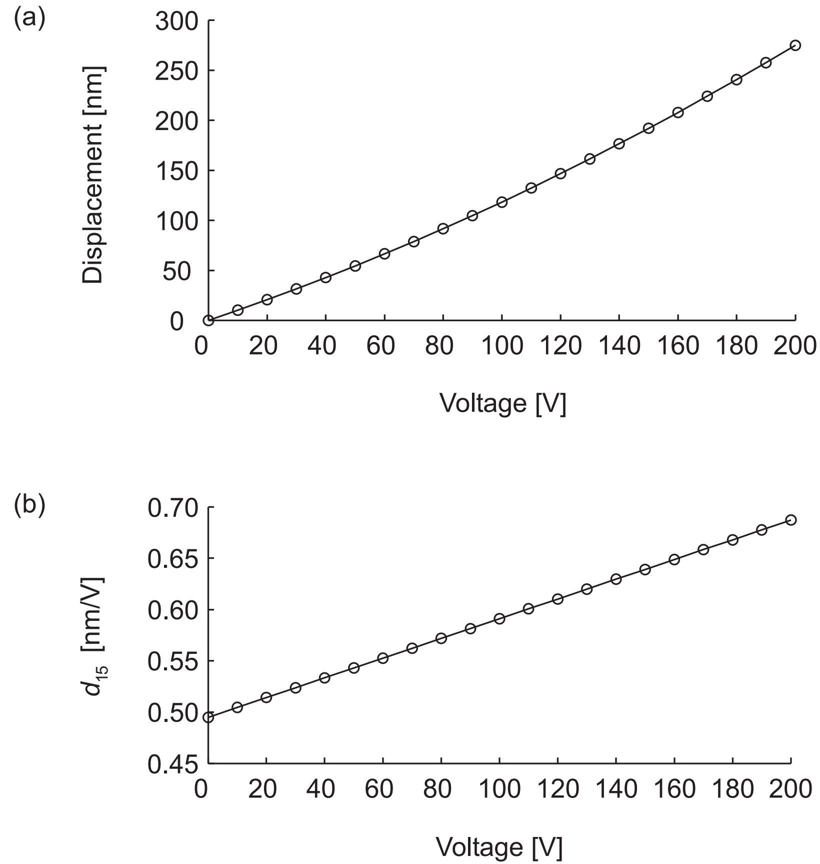

Figure 3.15: (a) Displacement of the actuactors versus applied voltage and (b) piezoelectric coefficient d_{15} versus applied voltage.

3.7 Motion Characteristics

3.7.1 Axial Motion

Scanning Mode

The motion characteristic of the motor in the scanning mode is directly related to the hysteresis in the piezoelectric actuators. For small motion, the effect of the hysteresis

is insignificant. An example of motion characteristics is shown in Fig. 3.16 for a 10 Hz square-wave input signal. The results show that shear strokes of 5 nm, 2 nm, and 1 nm can be achieved with applied voltages of 5 V, 2 V, and 1 V, respectively. The detection of smaller stroke values is limited by the resolution and noise of the capacitive displacement sensor. The actual stroke resolution of the motor depends on the noise of the high-voltage amplifier. The amplifier has a maximum peak-to-peak noise of about 5 mV, which corresponds to a movement of 5 pm.

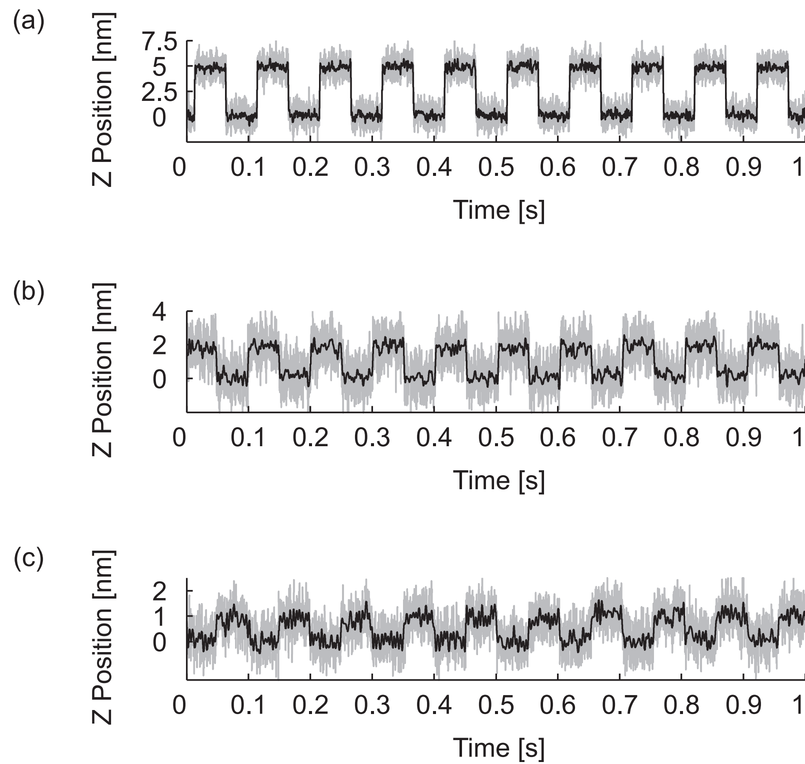

Figure 3.16: Motion characteristics of the motor for a 10 Hz square-wave input signal. The darker lines are the filtered data. (a) 5 nm stroke with cutoff at 500 Hz, (b) 2 nm stroke with cutoff at 275 Hz, and (c) 1 nm stroke with cutoff at 250 Hz.

For large motion, the effect of the hysteresis is significant. Furthermore, the hysteresis will vary with the frequency and the waveform of the driving signal [131, 132]. An example of the hysteresis loops of the motor is illustrated in Fig. 3.17 for a 10 Hz sinusoidal input with various voltage sweeps. The hysteresis clearly depends on the voltage sweep of the driving signal, it increases from 7.2% to 17.3% for an increase in

the voltage sweep from 40 V to 200 V.

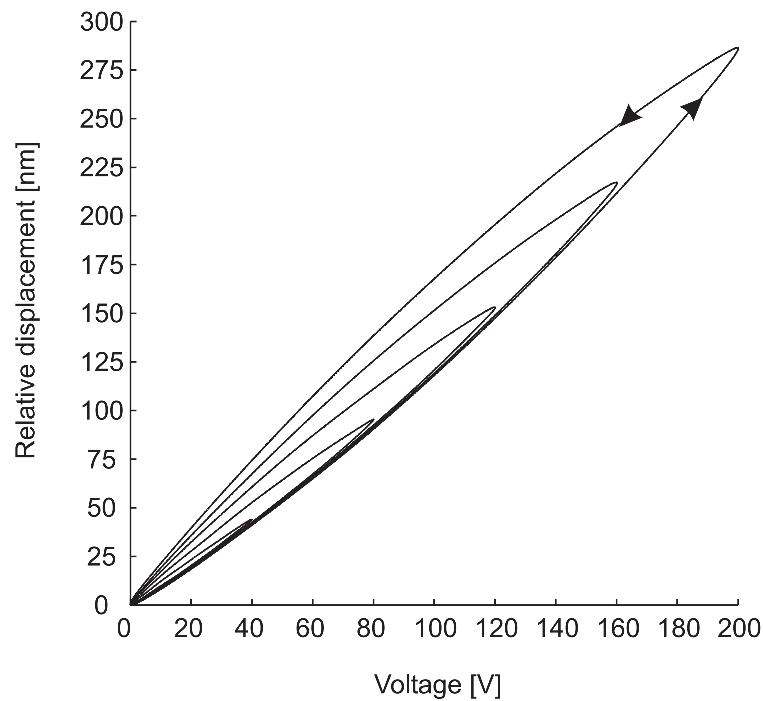

Figure 3.17: Hysteresis loops of the motor for a 10 Hz sinusoidal input with voltage sweeps of 40 V, 80 V, 120 V, 160 V, and 200 V.

Stepping Mode

An example of the axial motion of the linear motor in the stepping mode is shown in Fig. 3.18. It can be observed that the motions in the forward and backward directions are highly linear. The forward step motion of the linear motor is illustrated in Fig. 3.18(a). As expected and shown in Fig. 3.18(b), the backward step motion is inverted. The step motions show similar characteristic, and they are highly reproducible.

Each step, as shown in Fig. 3.19(a), begins with a momentarily reverve motion before advancing forward to complete the step. This is the intrinsic stepping motion characteristic for this type of linear motor. This characteristic cannot be realized by using the measurement methods utilized in the previous studies performed by others [114, 115].

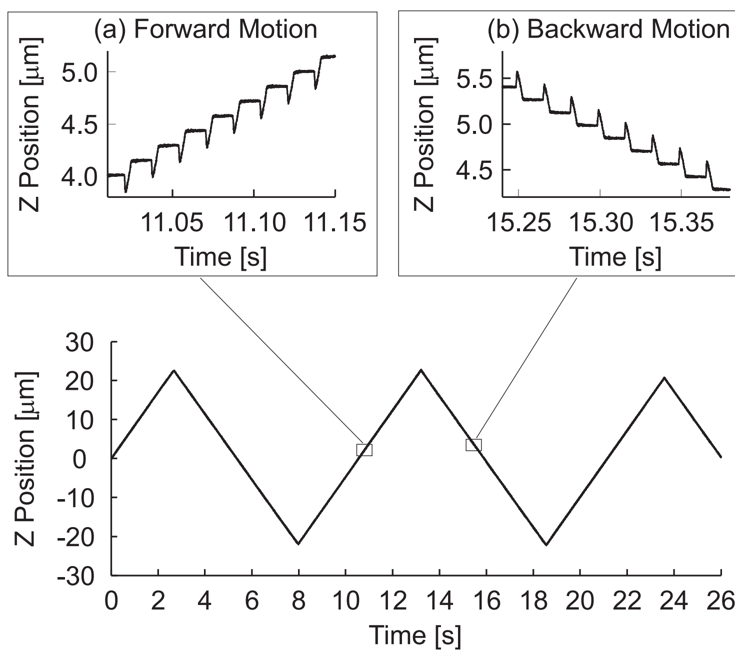

Figure 3.18: An example of the axial motion of the linear motor in the stepping mode. Step motions in the (a) forward and (b) backward directions. The preload force applied on the alumina prism is 24.5 N and the applied voltage is 196 V for both directions.

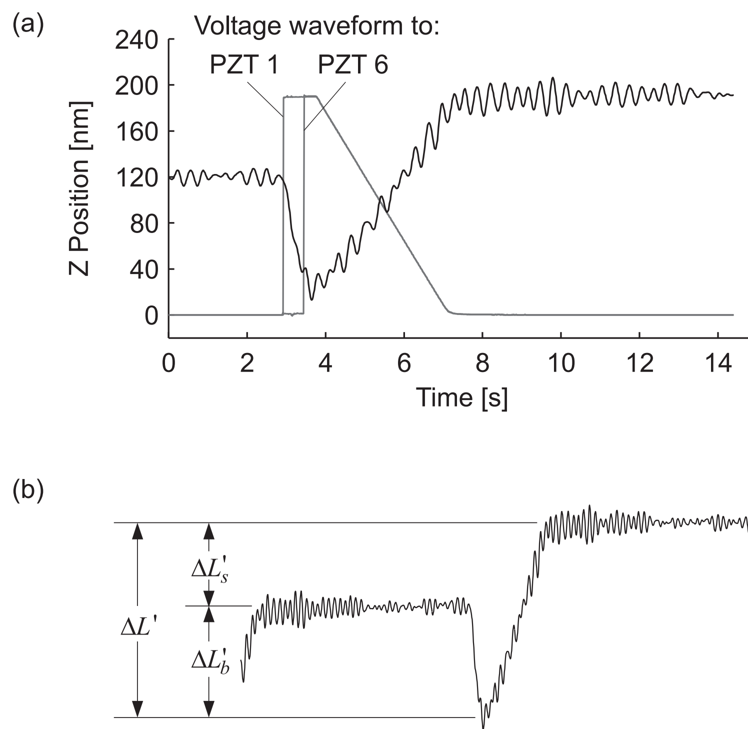

Figure 3.19: (a) Step Motion and (b) determination of step size.

Step motions for nine applied voltages of 43-196 V are shown in Fig. 3.20. The preload force applied on the alumina prism is 8.7 N. It can be seen from Fig. 3.20 the motion per step (step size) increases with the increasing in the applied voltage. The step motions of all 18 steps are highly reproducible with a very repeatable step size for each applied voltage. A maximum step size of 225 nm is obtained with an applied voltage of 196 V, which corresponds to a velocity of 13.5 μm/s. In the case for an applied voltage of 43 V, the step size is about 6 nm. Also observed in Fig. 3.20, the amount of reverse motion is almost independent on the applied voltage.

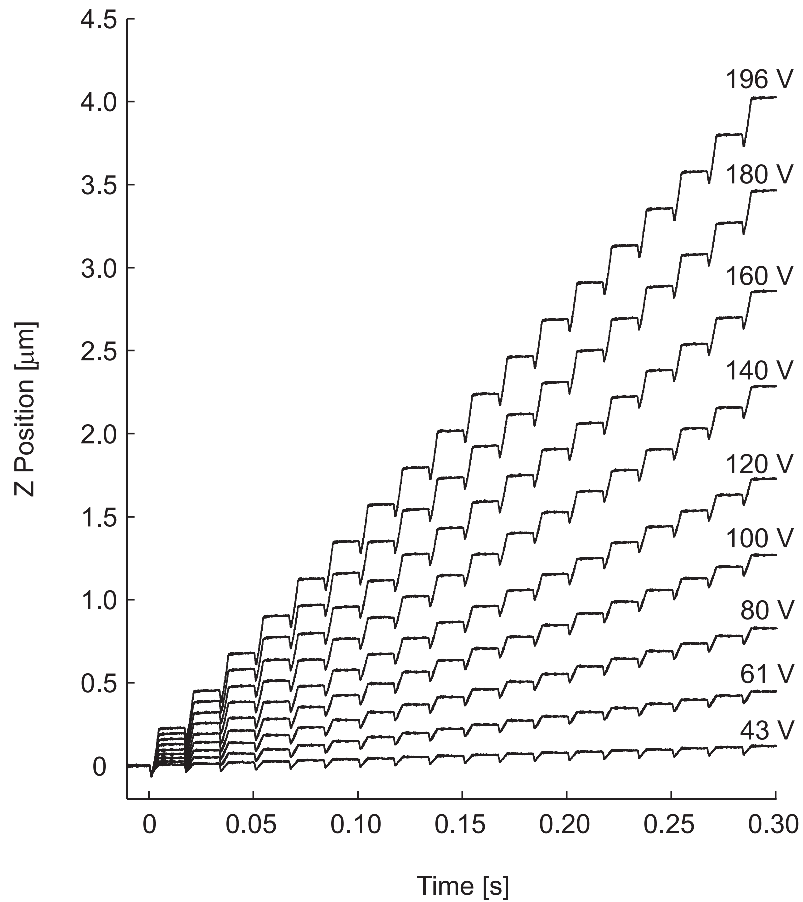

Figure 3.20: Step motions for various applied voltages.

The step size at various voltages and preload forces is measured for three different orientations: horizontal orientation, vertical orientation with front side of the motor facing up, and vertical orientation with front side the motor facing down. The mean step

size is calculated by averaging the step size for a known number of steps taken to travel about 50 μm. The step size is determined in the way as shown in Fig. 3.19(b).

Figure 3.21 shows the voltage dependent mean step size of various preload forces for all three orientations. For horizontal orientation, the step size for both forward and backward motions of a given preload force shows good similarity. For vertical orientations, the step size for a given preload force changes very slightly with a minute increase in the gravity assist direction when comparing to that of against gravity. The difference is the largest for the lighest preload force of 8.7 N at maximum voltage. Nevertheless, the orientations of the linear motor have very little effect on the step size. By increasing the preload force, the step size is reduced significantly, but it varies more linearly with the voltage.

As described early, each step begins with a reverve motion before advancing forward to complete the step. From Fig. 3.19(b), a relation between the step size $\Delta L'_s$, reverse motion $\Delta L'_b$, and advance motion $\Delta L'$ can be obtained as given in Eq. (3.20).

$$\Delta L'_s = \Delta L' - \Delta L'_b \tag{3.20}$$

The advance motion $\Delta L'$ is equivalent to Eq. (3.19) since it is independent on the preload force. By replacing the expected threshold voltage V_t in Eq. (3.14) with the experimental threshold voltage V'_t, the reverse motion $\Delta L'_b$ is then equivalent to Eq. (3.14). Using the d_{15} in Eq. (3.18) and V'_t = 42 V (for preload force of 8.7 N), the step size $\Delta L'_s$ becomes Eq. (3.21). The step size calculated using Eq. (3.21) is plotted in Fig. 3.21.

$$\Delta L'_s = 1.9222 \times 10^{-3} V^2 + 0.9898V - 44.96 \tag{3.21}$$

The expected threshold voltage calculated from Eq. (3.13) using the d_{15} (let V = V_t) given in Eq. (3.17) is listed in Table 3.3. The experimental threshold voltage is about 1.6 to 2.7 times higher than the expected value. The discrepancy in the threshold voltages has been reported by others [110, 114], they attributed the discrepancy to the deviations from the normal static friction limit when operating at such small-scale

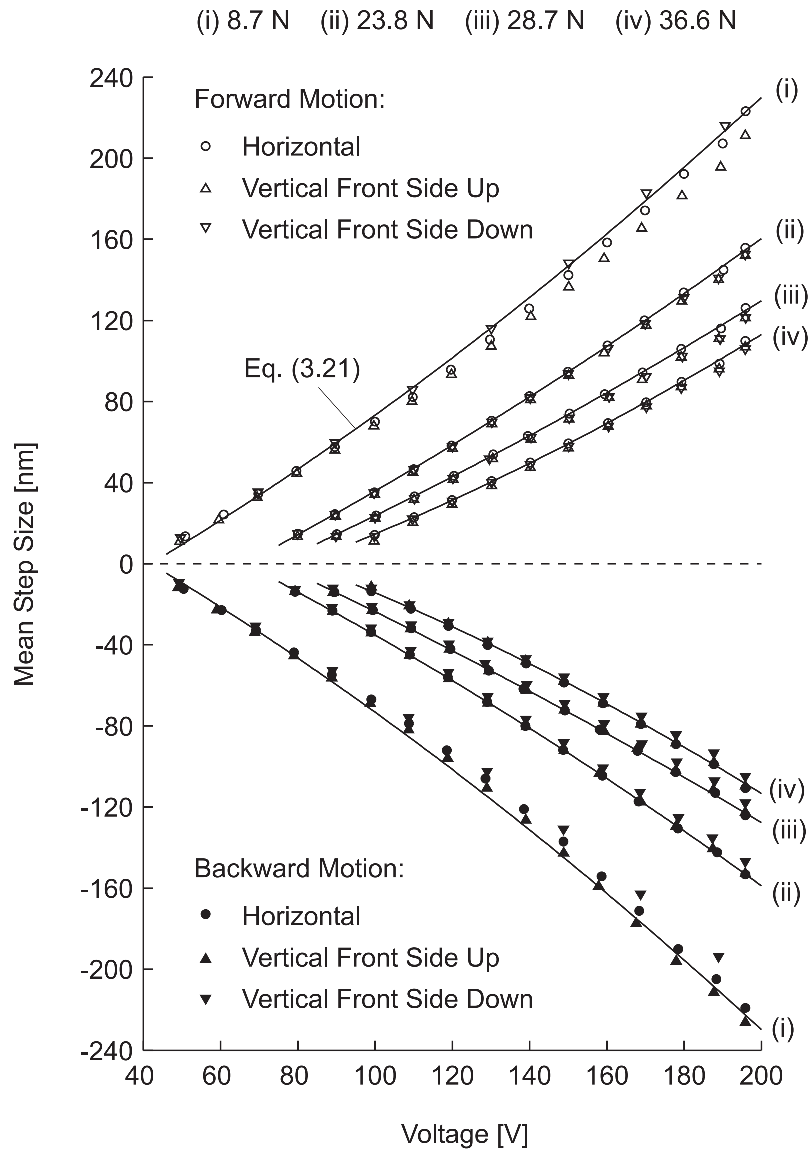

Figure 3.21: Voltage dependent mean step size of various preload forces for all three orientations of the piezoelectric linear motor.

motions. Gupta *et al*. [114] reported that the threshold voltage for his motor is about 21 to 29 times higher than the expected value. It is believed that the discrepancy is also contributed from the over simplified model of the linear motor. The effect of the moment is unaccounted in the model.

Table 3.3: Expected and experimental threshold voltages for various preload forces

Preload force, P	8.7 N	23.8 N	28.7 N	36.6 N
Expected V_t [V]	15.4	40.2	47.9	59.8
Experimental V_t' [V]	42	72	85	95

From Fig. 3.22, the probability plot suggests that the variation in the step size resembles a Gaussian distribution. Figure 3.23 shows that the standard deviation increases from about 0.4 nm to 1.2 nm as mean step size increases from about 10 nm to 225 nm. The step size is highly repeatable and the standard deviation is typically less than 1.2 nm.

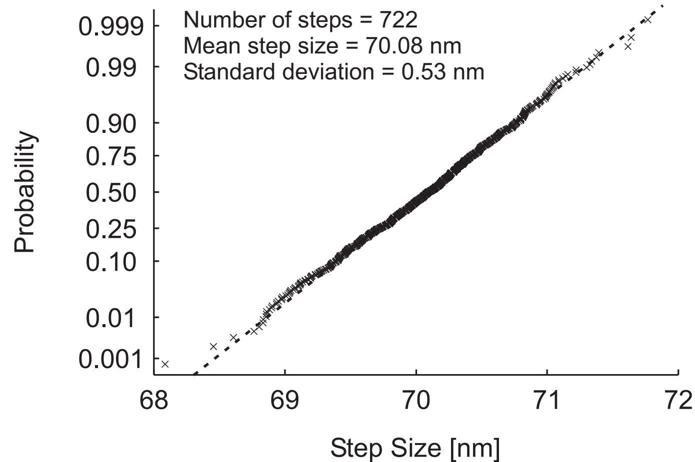

Figure 3.22: Probability plot of step size variation for applied voltage and preload force of 100 V and 8.7 N, respectively.

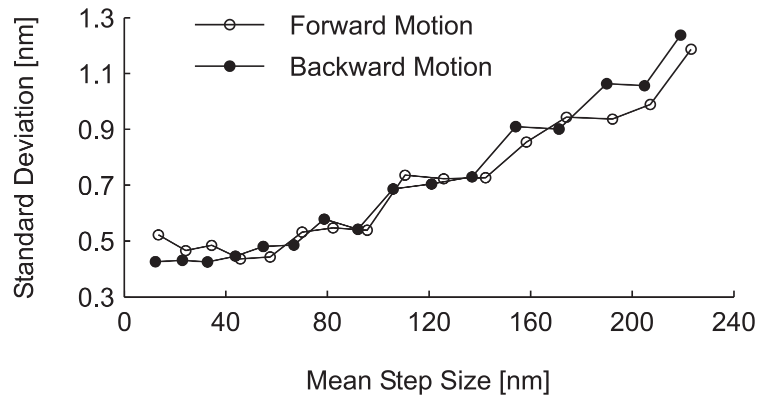

Figure 3.23: Mean step size versus standard deviation for preload force of 8.7 N.

Linearity

The linearity (position error) is defined as the deviation of the measured position from the ideal position along the Z-axis over a given travel range. The maximum deviation is used to calculate the linearity error, which is often expressed as a percentage over a given range. Due the measurement range of the capacitance displacement sensor, the linearity of the motor is based on a total travel range of about 250 μm. Figure 3.24 illustrates the linearity of the motor in the forward and backward directions for the horizontal orientation with a mean step size of about 100 nm under various preload conditions. The linearity error is the least for the preload force of 8.7 N, which is less than 0.3% in both directions. Overall, the linearity error of the motor is less than 1% over a travel range of 250 μm.

Looking at Fig. 3.24, one can observe an interesting characteristic of the motor which is its intrinsic hysteresis loop. The hysteresis for the preload forces of 8.7, 23.8, 28.7, and 36.6 N are 0.35%, 0.60%, 0.84%, and 0.84%, respectively. The results show that using a light preload force will minimize the hysteresis and linearity error of the motor.

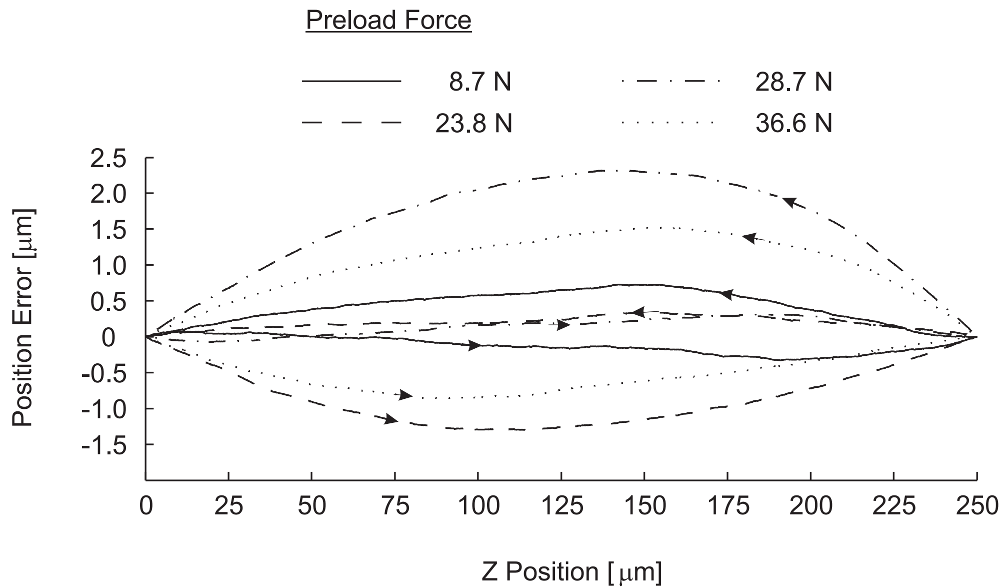

Figure 3.24: Linearity of the motor in the forward (arrow pointed to the right) and backward (arrow pointed to the left) directions for a mean step size of about 100 nm under various preload conditions.

3.7.2 Lateral Motion

The lateral motions were measured at a distance of 25.4 mm from the middle plane, between the front and rear preload planes, of the motor. For a preload force of 15 N, the characteristics of the lateral motions, for the motor to step almost two steps forward in the positive Z direction, are shown in Fig. 3.25.

The shearing of the piezoelectric actuators generate impulsive force that excites the resonant (tilt mode) of the motor. The oscillations in the X and Y directions occur at frequencies of 1.925 kHz and 2.038 kHz, respectively, regardless of the magnitude of the voltage step. This indicates the axis of the prism wobbles around the axis of the motor during stepping. The mechanical vibration is at its peak when the voltage step is at maximum. The amplitude of vibration reduces when operating at lower voltages, but the resonants remain unchanged. If the stepping direction of motor is reversed (negative Z direction), the lateral motions in Fig. 3.25 are inverted.

Similarly, for a higher preload force of 28 N, the characteristics of the lateral motions

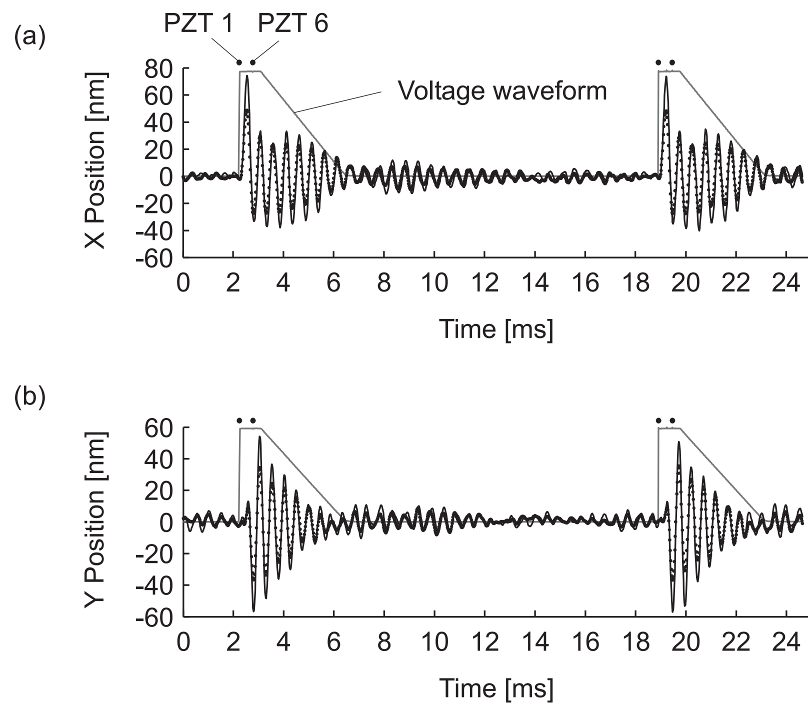

Figure 3.25: Lateral motions for preload force of 15 N (a) X direction (b) Y direction. The dots and solid lines are the lateral motions for voltage steps of 60 V and 196 V, respectively.

are shown in Fig. 3.26. The oscillations in the X and Y directions are more intense compare to the lighter preload but occur at slightly higher frequencies of 2.159 kHz and 2.337 kHz, respectively. It can be seen from Fig. 3.26, the lateral motions in the x and y directions indicated a beating phenomenon. This is due the exchange of energy between the X and Y directions because the difference in the natural frequencies is small. In general, the lateral motion is mainly due to the excitation of the natural frequency and the amplitude of the vibration are typically less than 100 nm.

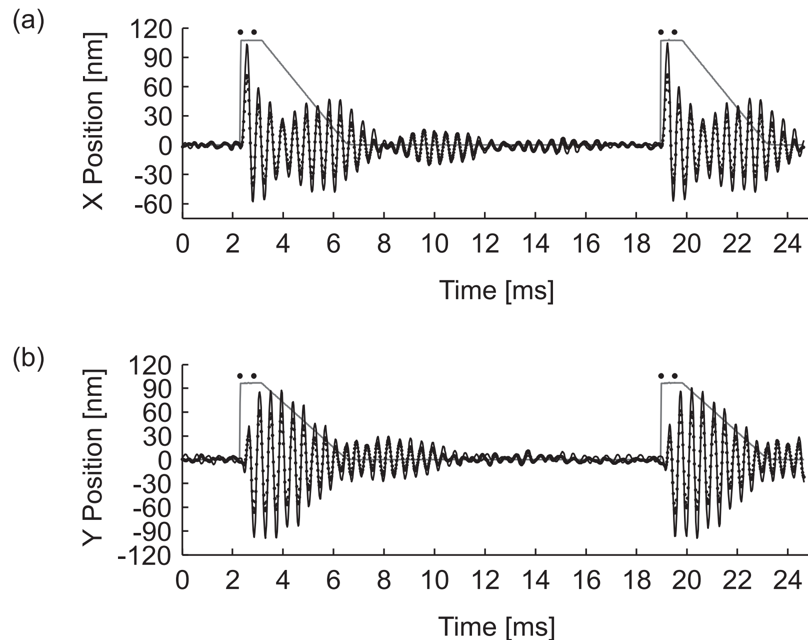

Figure 3.26: Lateral motions for preload force of 28 N (a) X direction (b) Y direction. The dots and solid lines are the lateral motions for voltage steps of 90 V and 196 V, respectively.

There is another kind of lateral motion, which is due to reversing the stepping direction of the motor. It causes a point on the alumin prism to shift gradually from one equilibrium position to the other. Figure 3.27 shows an example of the lateral motions in the X and Y directions caused by changing the stepping direction from forward to backward. The preload force is 24.5 N. The applied voltage is 196 V for both forward and backward motions. The shift in the X and Y directions are about $\pm$180 nm and $\pm$250 nm, respectively.

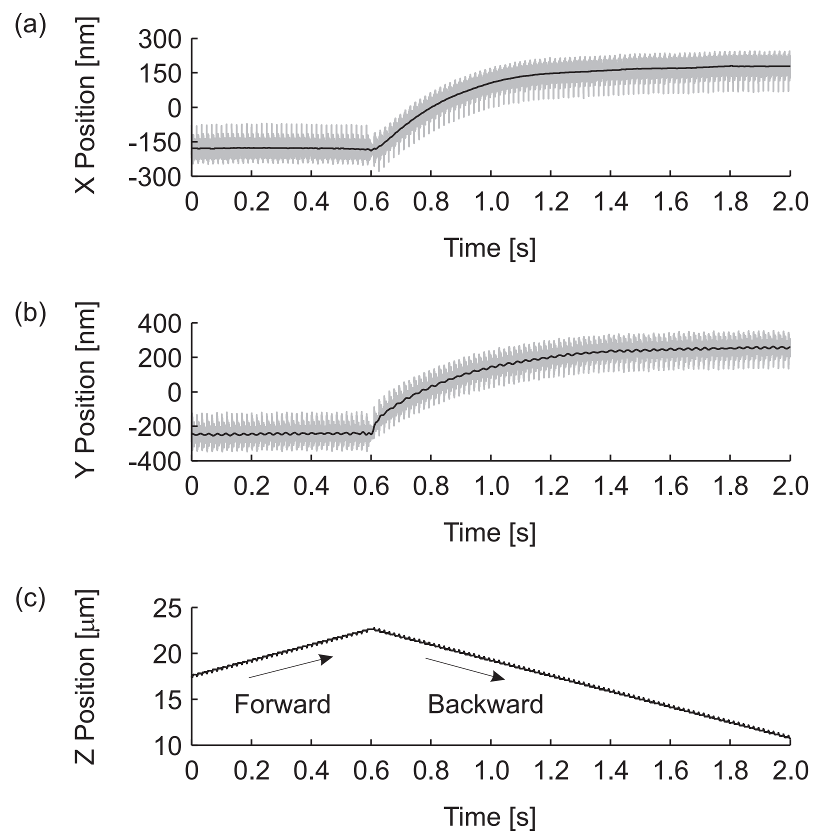

Figure 3.27: Lateral motions in the (a) X direction and (b) Y direction due to reversal in the (c) stepping direction. The darker lines are the filtered data with a cutoff frequency of 58 Hz.

When the motion direction is reversed, the axis of the prism shifts between two equilibrium positions. The gradual shift in the lateral direction may result from the residual moment caused by the uneven sliding of the actuators. This moment is then balanced by the driving mechanisms and belleville disc springs (reaction moment) in order to reach the equilibrium. The shift is typically less than $\pm$200 nm for low applied voltage and preload force.

3.8 Thermal Stability

Thermal stability measurement of precision instruments, especially those with thermal symmetric design, can be a very challenging task. The common method for measuring the thermal stability of an instrument is to use a displacement measurement sensor to detect any changes in position due to the change in temperature over a periond of time. This will produce reliable thermal stability measrement for instruments that are non-symmetry and rather large in size. For small and thermally symmetrical instruments, a single measurement in the direction of interest will be inadequate and can lead to an erroneous interpretation of the stability of the instrument under test. This is because the thermal expansion, contraction, and drift of the sensor, sensor target, and mounts are also temperature dependent. The resultant (combination) of these expansion, contraction, and drift can be much larger than the thermal stability of instrument. Thus, in oder to measure the thermal stability of an instrument accurately, proper tools with optimal arrangement and technique must be used.

The arrangement for the thermal stability measurement in the X direction near the front side of the linear motor is shown in Fig. 3.28(a). A photograph of the experimental setup is shown in Figure 3.28(b). The displacement sensors are held by a holder which is mounted to the invar housing, and the sensor target mounted on the alumina prism. Two identical sensors must be used and they must be aligned with each other with their length of protrusions kept the same from their holder. Similarly, the axis of the sensor target must be coincide with the axis of the alumina prism. To further minimize the thermal expansion, the target and sensors holder are made of invar 36. The sensor

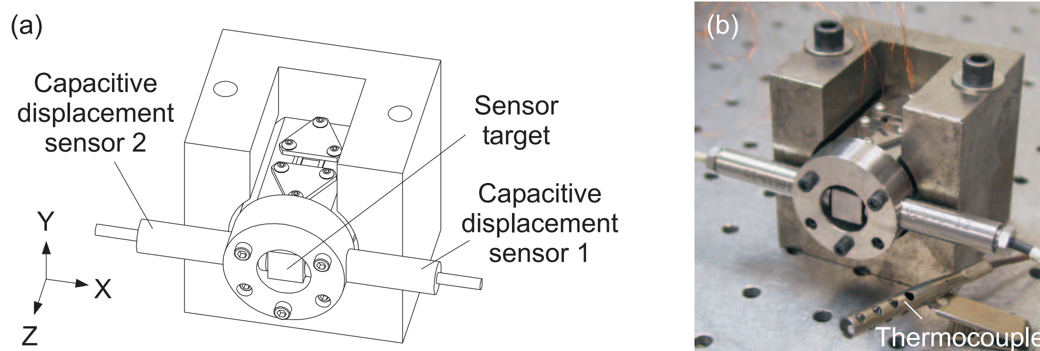

Figure 3.28: Experimental setup for measuring thermal stability in the X direction.

outputs for a given fixed position along the Z-axis include the thermal drift of the prism, the expansion of the sensor target, and the expansion of the sensors themselves. To eliminate the target and sensors thermal expansions, a cancellation technique is used.

As shown in Fig. 3.29, in order to apply this cancellation technique, two simultaneous measurements are required on both side of the sensor target. The sign convention follows the convention used for the sensors, which is positive with diminishing gap in between the surfaces of the sensor and target. And, the thermal drift is positive in the positive X direction.

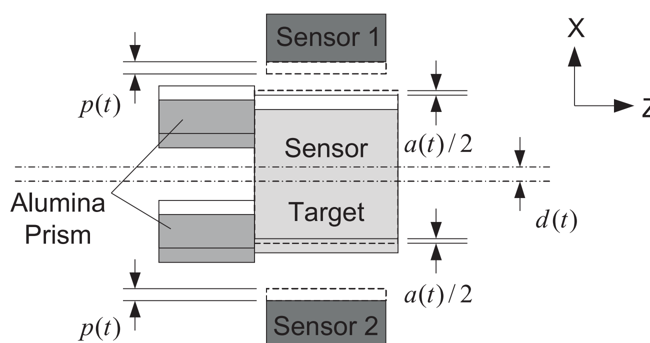

Figure 3.29: Schematic for thermal stability measurement in the X direction.

From the schematic in Fig. 3.29, the measurement from sensor 1, $m_1(t)$, is given in Eq. (3.22). Where, the parameters $p(t)$, $a(t)$, and $d(t)$ are thermal expansion/contrac-

tion of the sensors, sensor target, and thermal drift of the alumina prism, respectively.

$$m_1\left(t\right) = p\left(t\right) + \frac{a\left(t\right)}{2} + d\left(t\right) \tag{3.22}$$

Similarly, the measurement from sensor 2, $m_2(t)$, is given in Eq. (3.23).

$$m_2\left(t\right) = p\left(t\right) + \frac{a\left(t\right)}{2} - d\left(t\right) \tag{3.23}$$

The thermal drift in the X direction is thus given in Eq. (3.24).

$$d\left(t\right) = \frac{m_1\left(t\right) - m_2\left(t\right)}{2} \tag{3.24}$$

To minimize the electrical noise in the sensor outputs, the bandwidths of the sensor drivers are set to the lowest cutoff frequency at 100 Hz. The outputs are further filtered using a 0.1 Hz low-pass filter. The lateral thermal drift as given in Eq. (3.24) is a combination of radial thermal drift, which is the displacement perpendicular to the Z-axis in the X direction, and tilt thermal drift, which is the translation in the X direction caused by the rotation of the prism about Y-axis of the linear motor.

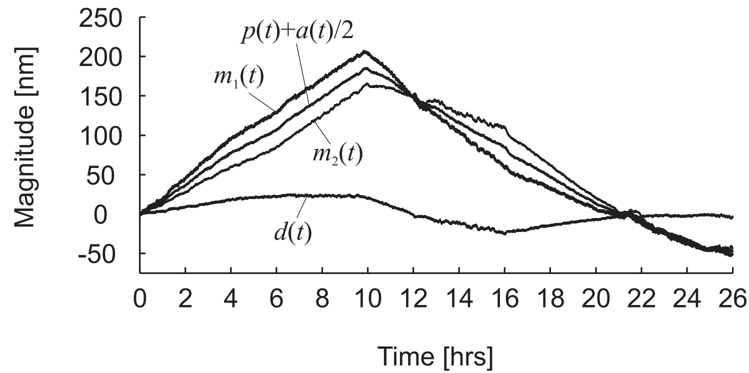

Figure 3.30: Cancellation technique for determining the thermal drift.

Figure 3.30 illustrates application of the separation technique for the lateral thermal drift and the thermal expansion. The ambient temperature profile are shown in Fig. 3.32. Both of the sensor outputs, $m_1(t)$ and $m_2(t)$, indicate that the gaps between

the sensors and the sensor target decrease and increase in a similar fashion. This is an obvious indication that the thermal expansion and contraction of the sensor and the target are dominant and much larger than the thermal drift. This shows that the thermal stability measurement using a single sensor would be inadequate. The cancellation technique using two simultaneous measurements would produce a more reliable thermal stability measurement. Ideally, if the sensor outputs $m_1(t)$ and $m_2(t)$ are the same, then there would be zero thermal drift.

The short-term thermal stability in the X direction is shown in Fig. 3.31. The thermal drift is typically less than 3 nm over a period of 20 minutes. This drift is acceptable for STM applications given that the usual duration of an image acquisition is typically less than 15 minutes.

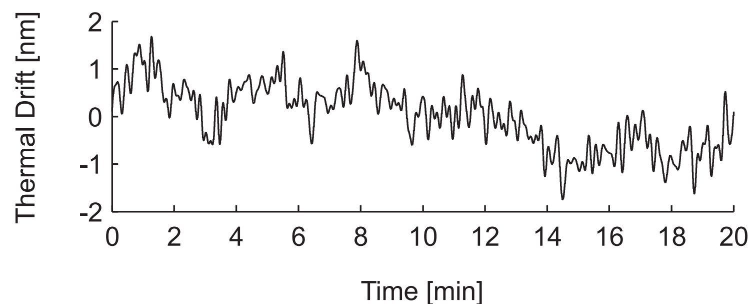

Figure 3.31: Short-term thermal stability of the motor in the X direction over a period of 20 minutes.

The long-term thermal stability in the X direction over a period of 26 hours is shown in Fig. 3.32. The preload force applied on the alumina prism is about 17 N. The thermal drift is about $\pm$25 nm over a temperature change of 1.8 $^{\circ}$C. This drift is equivalent to a change of about 10 milivolts in the sensor output. A careful observation of Fig. 3.32 reveals that the thermal drift roughly follows the trend of the ambient temperature. Theoretically, there shall be zero thermal drift because of the symmetric design. However, in practice, the motor may not be perfectly symmetry as indicated by the slight different in the resonants between the X and Y directions of the motor. Other reasons include sensor drivers may have internal electronic drifts and the sensors holder would have

some thermal drift associated with it.

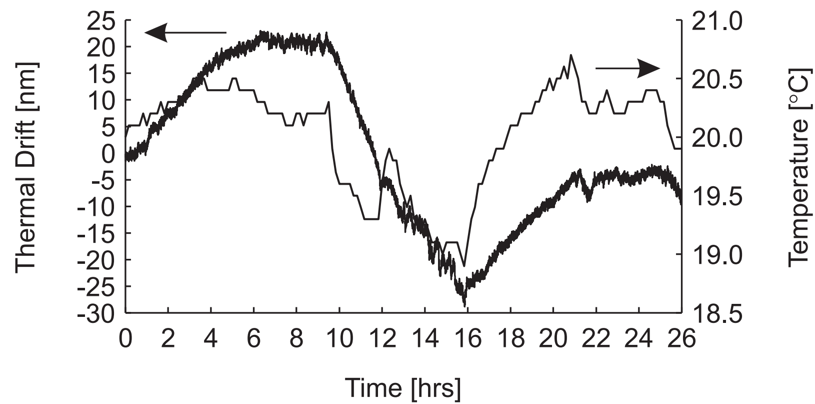

Figure 3.32: Long-term thermal stability of the motor in the X direction over a period of 26 hours.

3.9 Chapter Summary

A piezoelectric linear motor was fabricated and experimentally characterized. The results reveal the motion characteristic of the motor is unlike any other motors. Individual step motion consists of a momentarily reverse motion followed by a forward motion to complete the step. The step size can be adjustable by varying the magnitude of the applied voltage and the preload force clamping on the alumina prism. This provides two independent mechanisms for adjusting the size of a single step and provides for a unique step in which the translating prism actually moves backward before it moves forward. This attribute is particularly beneficial in some applications like SPM where the tip must not be crashed into the sample surface. The motor was found to exhibit some small hysteresis as well in stepping mode. The lateral motions were primarily due to the excitation of the linear motor lowest natural frequnecy. The step size is highly repeatable with standard deviation of less than 1.2 nm. The motor also shown good thermal stability in the lateral direction. For the of light preload force, a simple analytical model for calculating the step size shows good agreement with the experimental results when the experimental threshold voltage is used.

Chapter 4

Instrument for Nanolithographic Techniques Using Field-Emitted Electron Beams

4.1 Introduction to the Chapter

The previous chapter presented an important component of the instrument, which is the piezoelectric linear motor for coarse positioning that brings the tip close to the sample surface. In this chapter, several others essential components of the instrument are presented. The chapter begins with one of the most essential components, that is the scanner that provides the fine motions of the tip in the xyz directions. Another essential component of the instrument, vibration isolation, is also covered. The chapter concludes with demonstrating that the instrument can be used to measure surface topography as done in scanning probe microscopes.

4.2 Piezoelectric Scanner

The scanner is the device that moves the tip, whether used for field emission or scanning probe microscopy (SPM), above the sample surface in the lateral directions (x, y), and it controls the tip-sample separation distance in the axial direction (z). The design criteria and requirements for a good scanner are:

1. high resolution - the necessary resolution is less than 1 Å in the lateral directions (x, y) and 0.05 Å in the axial direction (z);

2. orthogonality - movement of each of the three axes should be independent or

decoupled;

3. linearity - the displacement should be linearly proportional to an applied voltage;

4. mechanical rigidity - a rigid scanner should have a high resonant frequency, which is favorable for both vibration isolation and feedback performance;

5. symmetrical design and configuration - it is essential to cancel or minimize thermal drift; and

6. large scan range - it is desirable to cover as large a sample area as possible without sacrificing the resolution.

It is impossible to meet all of these design criteria and requirements with a simple and cost effective design. Scanners made from piezoelectric actuators meet most of these design specifications. The commercially available piezoelectric ceramics such as lead zirconate titanate (PZT) is suitable and frequently used in scanning tunneling miscroscopy (STM) scanners. The maximum displacement of a piezoelectric actuator is ultimately limited by the piezoelectric material and the size of the actuator. The desired piezoelectric constant (sensitivity) for the piezoelectric elements should be determined by considering the desired scan range and resolution, as well as the output voltage range and noise level of the driving circuits. The driving circuits have a certain amount of electrical noise associated with them, and this translates into uncertainty in the tip position, which ultimately limits the resolution of the scanner.

There are three main types of piezoelectric scanners used in SPM: (a) tripod scanner, (b) single tube scanner, and (c) scanner with mechanical flexural stage. A tripod scanner with three piezoelectric rectangular bars mounted perpendicularly to each other was the type first used in STM [8]. It has a reasonably high resonant frequency, and it is reasonably orthogonal. But, it is rather sensitive to thermal drift because of its non-symmetrical design. The first single piezoelectric tube scanner was developed [118] to minimize the thermal drift problem inherent in the tripod scanner - at least in the raster scanning directions (x, y).

The single piezoelectric tube scanner has become popular due to its simple and compact structure, its thermal stability in the lateral directions (x, y), its high sensitivity, and its high resonant frequency. The tube scanner is engineered to produce both lateral and axial motions. A tube scanner is made from a single piezoelectric tube polarized radially with electrodes on the inner and outer wall surfaces. The outer wall electrode of the tube is often divided into four quadrants of equal area. By applying mirror-symmetric driving signals across two diagonally opposite electrodes, the tube bends perperdicularly to its axis, producing lateral motions (x, y). If the driving signal is applied to only one quadrant of the electrode, the orthogonolity is degraded significantly, which will be illustrated later in the section. This is partially due to the asymmetric stress developed in the tube and partially due to the charge on the inner electrode, which is not cancelled by the electrode on the opposite quadrant.

There are two ways to produce axial motion (z) of the tube scanner. The first is by applying the $z-$motion driving signal to the inner wall electrode of the tube, causing the tube to elongate or contract. The second is by summing the axial driving signal directly to the lateral driving signals with the inner wall electrode of the tube grounded. Both ways produce axial motion. The only disadvantage of these is the dynamic (scan) ranges of the lateral motions are shared with the axial motion. This may not be a problem for small scanning area and a relatively flat sample surface. But, for large scanning area and a relatively rough sample surface, one or more of the driving signals could be saturated due to the limited dynamic range of the driving circuits. This can be avoided by adding an additional portion of the piezoelectric element to the tube scanner for the axial motion. The trade-off is that the resonant frequency of the tube scanner is reduced slightly due to the additional length of the tube scanner that is added for the axial motion.

Scanners made from mechanical flexural stages coupled with stacked piezoelectric actuators and positioning sensors are more suitable for scanning large objects over large areas ($>$ 10 μm) [131, 134], yet most of these scanners have relatively low mechanical resonant frequencies ($<$ 1 kHz) and are usually bulky. Although with the addition of position sensors in a closed-loop scanner, one can improve linearity and orthog-

onality significantly, the resolution of the scanner suffers due to the additional electrical noise in the position sensors. Such a scanner typically costs ten times more than a single piezoelectric tube scanner. It is usually used in more demanding applications that require large scanning areas such as machined surfaces [135] and semiconductor microfabrication [136], and they are commonly found in atomic force microscopes (AFM).

By comparing these three types of scanners, it is most appropriate to use a single piezoelectric tube scanner in this work because of its cost effectiveness, reasonable performance, and integration with the piezoelectric linear motor. Selecting the proper material for the piezoelectric scanner depends on its working environment. Piezoelectric materials are available in a variety of properties and compositions. The PZT-5H and PZT-5A types are commonly used in STM because of their high sensitivities. The PZT-5H has a higher piezoelectric sensitivity than PZT-5A, but is less suitable for high temperature applications due to its low Curie temperature of about 200 °C. Since the instrument will be used in the UHV environment which would require occasional bake-out, it is essential to use piezoelectric materials with the highest Curie temperature possible to prevent depoling of the material. The PZT-5A meets this specification with a Curie temperature of 350 °C. Another advantage of using PZT-5A is that its piezoelectric coefficient d_{31} is less temperature dependent.

Many useful articles have reported on modeling the behavior of piezoelectric tube scanners for electromechanically producing displacement (analytically [137, 138, 139, 140, 141] or numerically [142]), their nonlinearity and hysteresis [132, 143, 144], their temperature effects [137, 145, 146], and their dynamics [138, 147, 148, 149]. These studies show that a piezoelectric tube scanner can be properly calibrated and controlled when used in the scanning probe microscopes (SPM) and other precision applications.

4.2.1 Tube Scanner Displacement

Simple analytical expressions for the displacements of a piezoelectric tube are obtained for one end fixed at its base and another end fixed to a rigid block, but allowed to move freely. The evaluation of the displacement in the axial direction (z) is fairly

straightforward. Because the piezoelectric tubes are poled in the radial direction, by the definition [150] of the piezoelectric coeeficient d_{31}, the z displacement of the tube shown in Fig. 4.1(a) is given by Eq. (4.1), where V is the voltage applied to the outer electrode with the inner electrode grounded, L is the length, and t is the wall thickness of the piezoelectric tube.

$$\Delta z = d_{31}VL/t \tag{4.1}$$

The sensitivity of the piezoelectric tube in the axial direction K_z is obtained by differentiating Eq. (4.1) with respect to the applied voltage V as given in Eq. (4.2).

$$K_z = d_{31}L/t \tag{4.2}$$

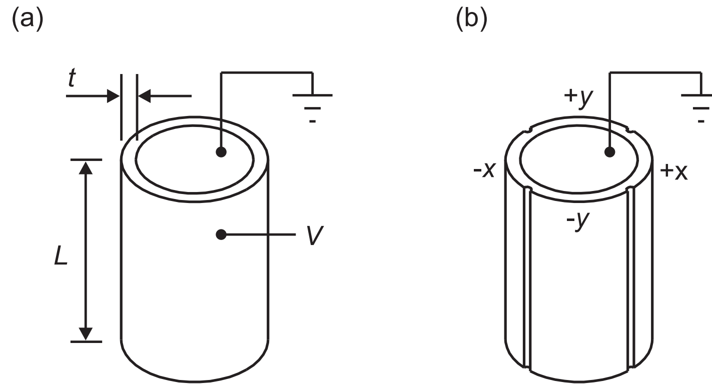

Figure 4.1: (a) A single piezoelectric tube for axial motion and (b) A single piezoelectric tube for lateral motions (x, y).

The evaluation of the lateral displacements (x, y) is slightly more complicated. The outer electrode of the piezoelectric tube is divided into four quadrants of equal area as illustrated in Fig. 4.1(b). The diagonally opposite pairs of the electrodes are labeled as $+x$ and $-x$, and as $+y$ and $-y$. By using mirror-symmetric driving signals, a voltage V is applied to the $+x$ quadrant and $-V$ is applied to the $-x$ quadrant with the inner and y-quadrants electrodes grounded. The $+x$ quadrant of the tube contracts and the

$-x$ quadrant of the tube elongates, presumably by the same amount, causing the end of the tube to bend in the $+x$ direction, perpendicular to the axis of the tube. Figure 4.2 illustrates the generation of lateral displacements by bending within a piezoelectric tube scanner.

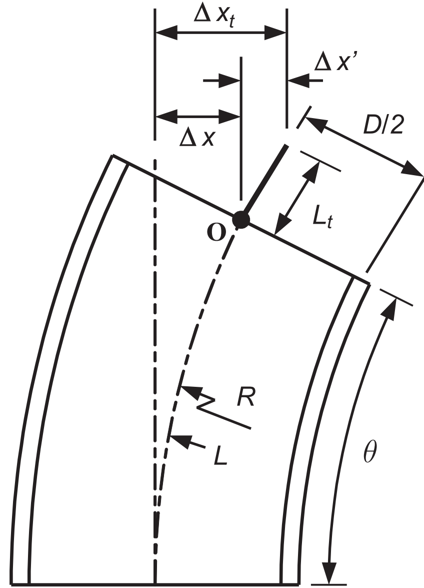

Figure 4.2: Generation of the lateral displacement in the x direction by bending within a piezoelectric tube scanner.

Chen *et al*. [139] found that the bending radius-of-curvature of the tube is given by Eq. (4.3), where D is the mean diameter, $D = (D_o + D_i)/2$, of the tube.

$$R = \frac{\pi D t}{4\sqrt{2} d_{31} V} \tag{4.3}$$

From Fig. 4.2, the lateral displacement at the end of the tube in the x direction is given by Eq. (4.4) [139] since $\cos\theta = 1 - \theta^2/2! + \cdots$ (Maclaurin series) and $\theta = L/R$.

$$\Delta x = R(1 - \cos\theta) \approx \frac{L^2}{2R} = \frac{2\sqrt{2} d_{31} V L^2}{\pi D t} \tag{4.4}$$

Similarly, the lateral displacement at the end of the tube in the y direction is identical as given in Eq. (4.5).

$$\Delta y = \frac{2\sqrt{2} d_{31} V L^2}{\pi D t} \tag{4.5}$$

The piezoelectric sensitivity in the lateral direction is then given by Eq. (4.6).

$$K_x = K_y = \frac{2\sqrt{2} d_{31} L^2}{\pi D t} \tag{4.6}$$

If the voltage is applied to only one of the four quadrants, the lateral displacement becomes one-half of the displacement in Eqs. (4.4) and (4.5). It is simply the consequence of symmetry [139]. Although using a single quadrant can improve resolution by reducing the scan range by half, it is usually not recommended because: (1) the orthogonality is degraded significantly and (2) asymmetric heating of the quadrants during operation can cause undesirable thermal drift.

Because of the way the lateral displacement of a tube scanner is generated by shortening and elongating two opposite quadrants simultaneously, the placement of the tip or field emitter at the end of the tube is very crucial. As shown in Fig. 4.2, the ideal placement of the tip or field emitter is at the end of the tube and coincides with the axis of the tube, as denoted by point O. This is the location where the coupling in between the lateral (x, y) and axial (z) motions is minimal and is also the thermal center of the tube.

Realistically, the tunneling tip or field emitter protrudes a finite distance from point O. The length of the protrusion has some effect on the lateral displacement at the end of the tip. The protruding length of the tip amplifies the lateral displacement at the end of the tip. The influence of the tip length mounted at the end of the tube can be evaluated rather easily. From Fig. 4.2, the additional lateral displacement at the end of the tip caused by the bending of the tube is given by Eq. (4.7), where L_t is the length of the tip.

$$\Delta x' = \theta L_t = \frac{L}{R} L_t = \frac{4\sqrt{2} d_{31} V L}{\pi D t} L_t \tag{4.7}$$

Thus the lateral displacement at the end of the tip is given by Eq. (4.8) and its sensitivity is given by Eq. (4.9). The formula for the lateral displacement in the y direction

is identical.

$$\Delta x_t = \Delta x + \Delta x' = \frac{2\sqrt{2}d_{31}V\left(L + 2L_t\right)L}{\pi Dt} \tag{4.8}$$

$$K_{x_t} = \frac{2\sqrt{2}d_{31}\left(L + 2L_t\right)L}{\pi Dt} \tag{4.9}$$

It can be seen from Eq. (4.8) that the lateral displacement at the end of the tip also depends on the length of the tip. This is a big disadvantage of using piezoelectric tube scanner; tip lengths will vary and hence the sensitivities K_{x_t} and K_{y_t} will be uncertain and require calibration. One should use the same tip length when changing a tip, otherwise the lateral displacement at the end of the tip will need to be recalibrated. Although the motion at the end of the tip follows a circular arc trajectory during lateral scanning, this circular arc motion produces a relatively small error in the axial direction [140].

One can use these displacement formulas, Eqs. (4.1), (4.4), (4.5), and (4.8), as a good approximation for small driving signals, given that the piezoelectric coefficient d_{31} is known and is assumed to be constant. For larger driving signals, the piezoelectric coefficient d_{31} is no longer constant and it varies with the range of the applied voltage. Furthermore, the standard tolerances of the piezoelectric coefficient d_{31} are $\pm 20\%$ of the typical manufacturer values [139]. Thus, the piezoelectric coefficient d_{31} should be measured experimentally for a given piezoelectric tube scanner, preferably for all three axes or directions.

4.2.2 Tube Scanner Calibration

Common problems with piezoelectric actuators include nonlinearity, hysteresis, creep, and aging. Piezoelectric ceramics are ferroelectric materials, and thus their response to applied electric fields is nonlinear. This leads to undesirable characteristics such as hysteresis and creep. The effects become increasingly noticeable at higher electric fields. For small scanning areas, which can be provided by low electric fields, the non-linear effects are minimal. For larger scanning areas, the nonlinearity and hysteresis

become more noticeable due to higher elctric fields required to produce larger strains.

Piezoelectric creep is the slow motion of the actuator over time after a change in the applied electric field. These nonlinearity, hysteresis, and creep effects can be minimized by controlling the total charge applied to the piezoelectric actuators rather than the voltage [151, 152]. However, even with this method, the scanner still has non-ideal mechanical motions due to stresses generated during scanning. A more elaborate method is to use independent position sensors such as an optical sensor or a capacitive displacement sensor for all the axes.

In this work, high-voltage amplifiers are used to drive the piezoelectric tube scanner. Thus, the displacements in all three axes of the scanner as a funtion of the applied voltage must be measured experimentally. These displacement measurements can then be used to correct: (1) the positioning error of the tunneling tip or field emitter over the sample, and (2) the distortion in the STM images.

Figure 4.3 shows the piezoelectric tube scanner used in the instrument for providing three-dimensional motions of the tip or field emitter. The upper portion of the tube scanner has its outer electrode (on the outer circumferential surface of the tube) segmented into four equal quadrants, and it is used to provide the lateral motions in the x and y directions. The lower portion of the tube scanner has a single outer electrode wrapped around the outer circumferential surface of the tube, and it is used to provide the axial motion in a z direction. The inner electrode on the inner circumferential surface of the tube is electrically grounded. Thus, the piezoelectric tube scanner is actually a xy scanner stacked on top of the z scanner. One can still apply the displacement formulas given in the previous section, Eqs. (4.1), (4.4), (4.5), and (4.8), for this tube scanner, but now L corresponds to the length of the electrodes and not the length of the tube.

The purpose of using the lower portion of the tube scanner as the z scanner, which is closer the scanner support, is to minimize the tip length effect, as one has learned from the previous section that the overall length of the tip (measured from the end of the tip to the end of the xy scanner) can significantly amplify the lateral displacements of the xy scanner. The directional assignment of the outer electrodes on the outer circumferential surface of the tube scanner is shown in Fig. 4.3(a). A photograph of

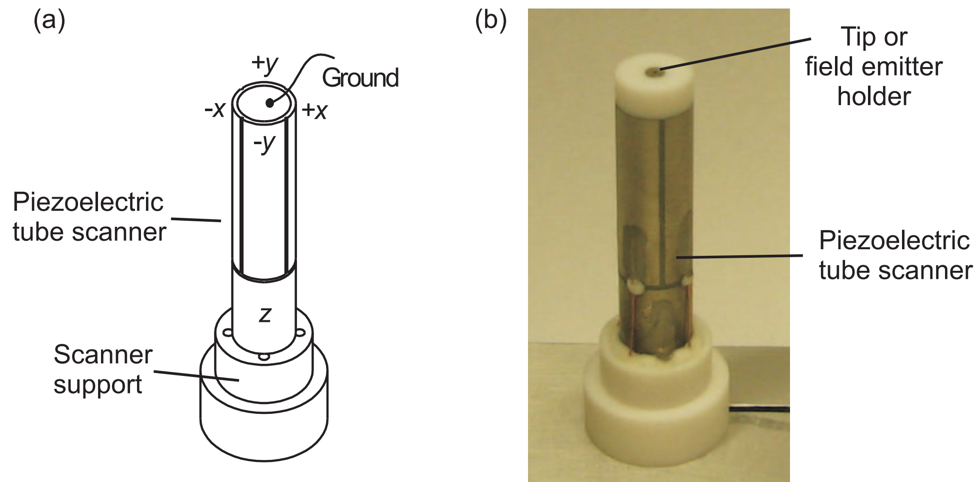

Figure 4.3: Piezoelectric tube scanner used in the instrument. (a) Directional assignment of the outer electrodes and (b) Photograph of the tube scanner.

the tube scanner assembly is shown in Fig. 4.3(b). The dimensional parameters of the piezoelectric tube scanner are tabulated in Table 4.1, and the expected values for the sensitivities in the axial (z) and lateral (x, y) directions, predicted using Eqs. (4.2) and (4.9) for L_t = 5 mm based on small driving signal, are 3 nm/V and (25 - 26) nm/V, respectively.

Table 4.1: Specifications and dimensions of the piezoelectric tube scanner

Material	PZT-5A
Piezoelectric coefficient, d_{31}	0.200 nm/V^a
Outer diameter, D_o	6.350 mm
Inner diameter, D_i	5.334 mm
Mean diameter, D	5.842 mm
Wall thickness, t	0.508 mm
Length of z scanner, L_z	7.62 mm
Length of xy scanner, L_{xy}	15.80 mm

^{a} approximated value

Figure 4.4 illustrates the experimental setup for measuring the displacements of the piezoelectric tube scanner in the axial (z) and lateral (x, y) directions. The dis-

placement measurements are the initial effort in calibrating the tube scanner. The final calibration of the tube scanner shall be performed and fine tuned using a standard tube scanner calibrator by operating the instrument in the STM mode. The details of the displacement measurement system were given in Chapter 3. The sensor target for the capacitive displacement sensor is a cube made from invar. The sensor target is mounted at the end of the piezoelectric tube scanner as shown in Fig. 4.4. The support of the tube scanner is clamped in the fixture. The fixture also holds the displacement sensor. The displacement of the tube scanner in the respective axis can be measured by clamping the displacement sensor on the fixture in the direction of interest as shown in Fig. 4.4.

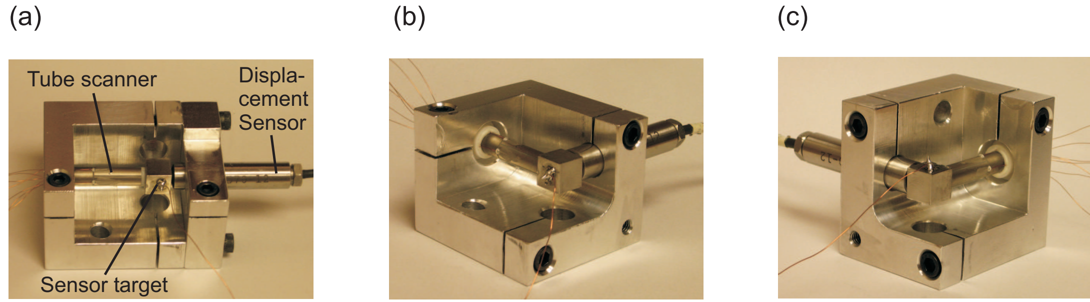

Figure 4.4: Experimental setup for measuring the displacements of the piezoelectric tube scanner in the (a) axial z-direction, (b) lateral x-direction, and (c) lateral y-direction.

The experimental setup shown in Fig. 4.4(a) was used for measuring the displacement of the z scanner. It is common to use a polynomial function to describe the displacement of a piezoelectric actuator [131]. The displacement of the z scanner, ΔL_z, as a function of the applied voltage, V_z, can be described fairly well by a 3rd-order polynomial, as given in Eq. (4.10), where p_1^z, p_2^z, and p_3^z are the coefficients of the polynomial. The coefficients of the polynomial can be determined by curve fitting the 3rd-order polynomial to the experimentally measured displacement.

$$\Delta L_z = p_1^z V_z + p_2^z V_z^2 + p_3^z V_z^3 \tag{4.10}$$

The piezoelectric sensitivity of the z scanner, K_z^l, can be described by Eq. (4.11),

where K_z^s is the small signal piezoelectric sensitivity of the z scanner, which is similar to Eq. (4.2), and α_z and β_z are the nonlinearity parameters of the z scanner.

$$K_z^l = K_z^s + \alpha_z V_z + \beta_z V_z^2 \tag{4.11}$$

The displacement of the z scanner, ΔL_z, can be rewritten as Eq. (4.12), which is the multiplication of the piezoelectric sensitivity, K_z^l, by the applied voltage, V_z.

$$\Delta L_z = K_z^l V_z = K_z^s V_z + \alpha_z V_z^2 + \beta_z V_z^3 \tag{4.12}$$

It can be noticed that Eq. (4.12) has the same form as Eq. (4.10). Thus, by equating the coefficients of the polynomials, the small signal piezoelectric sensitivity, K_z^s, and the nonlinearity parameters, α_z and β_z, of the z scanner can be found.

It is also convenient to give the piezoelectric coefficient of the z scanner, d_{31}^z, since it is independent of the dimension of the z scanner. Substituting the relations $K_z^l = d_{31}^z \frac{L_z}{t}$ and $K_z^s = d_{31}^{zs} \frac{L_z}{t}$ into Eq. (4.11), the piezoelectric coefficient, d_{31}^z, can be expressed as Eq. (4.13), where d_{31}^{zs} is the small signal piezoelectric coefficient of the z scanner.

$$d_{31}^z = d_{31}^{zs} + \alpha_z \left(\frac{t}{L_z}\right) V_z + \beta_z \left(\frac{t}{L_z}\right) V_z^2 \tag{4.13}$$

Substituting d_{31}^z, Eq. (4.13), into the relation: $K_z^l = d_{31}^z \frac{L_z}{t}$, and then substituting K_z^l into Eq. (4.12), the displacement of the z scanner, ΔL_z, can also be rewritten as Eq. (4.14).

$$\Delta L_z = d_{31}^{zs} \left(\frac{L_z}{t}\right) V_z + \alpha_z V_z^2 + \beta_z V_z^3 \tag{4.14}$$

It can also be noticed that Eq. (4.14) has the same form as Eq. (4.10). The small signal piezoelectric coefficient, d_{31}^{zs}, and the nonlinearity parameters, α_z and β_z, of the z scanner can also be found by equating the coefficients of the polynomials.

Figure 4.5 shows the measured displacement (forward hysteresis curve) produced by the z scanner for a triangular waveform input at 2 Hz, with an input voltage range of 200 V. By fitting the 3rd polynomial in Eq. (4.10) to the data in Fig. 4.5, the displacement

of the z scanner, ΔL_z [nm], is given by Eq. (4.15). Using the dimension of the z scanner listed in Table 4.1, the calculated values of K_z^s, d_{31}^{zs}, α_z, and β_z, of the z scanner for a triangular waveform input at 2 Hz are listed in Table 4.2.

$$\Delta L_z = 2.934V_z + 9.951 \times 10^{-3}V_z^2 - 1.008 \times 10^{-5}V_z^3 \tag{4.15}$$

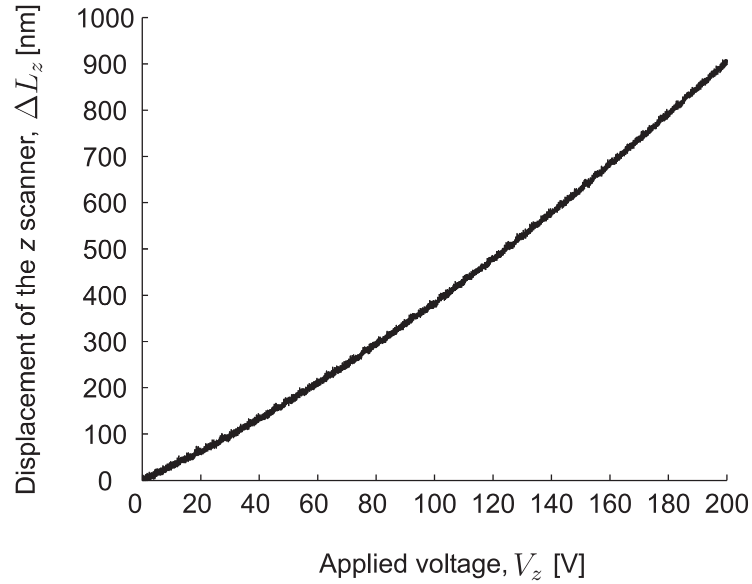

Figure 4.5: Displacement (forward hysteresis curve) of the z scanner for a triangular waveform input at 2 Hz.

Table 4.2: The values of K_z^s, d_{31}^{zs}, α_z, and β_z, of the z scanner for a triangular waveform input at 2 Hz

K_z^s (nm/V)	d_{31}^{zs} (nm/V)	α_z (nm/V^2)	β_z (nm/V^2)
2.934	0.196	9.951 $\times$ 10^{-3}	-1.008 $\times$ 10^{-5}

To linearize the displacement ΔL_z of the z scanner, a preshaped waveform is generated in two steps: (a) the voltages V_z needed to produce the positive ramp of the z scanner are obtained by solving the root (0 $\leq V_z \leq$ 100) of Eq. (4.15) and (b) the voltages V_z needed to produce the negative ramp are obtained by inverting the voltages V_z

obtained in (a). These voltages are then combined to produce the preshaped waveform needed for the nonlinearity correction. Figure 4.6(a) shows the displacement of the z scanner with a triangular input waveform at 2 Hz for an input voltage range of 100 V (without nonlinearity correction). The linearity in the displacement of the z scanner is much improved with a preshaped input waveform as demonstrated in Fig. 4.6)(b). The residual plots of Fig. 4.6)(c) indicate that an improvement in the linearity of at least 5 times can be achieved by this method. This is a fairly simple method, but it can be very useful in STM applications for correcting the lateral displacements of the piezoelectric tube scanner.

For calibration of lateral displacements of the xy scanner, the displacements were measured at about 5 mm from the end of the piezoelectric tube scanner. The experimental setups shown in Figs. 4.4(b) and 4.4(c) were used for measuring the lateral displacements in the x and y directions of the xy scanner, respectively.

Similarly, the lateral displacement of the xy scanner in the x-direction, ΔL_{x_t}, as a function of the applied voltage, V_x, can be described by a 3rd-order polynomial, as given in Eq. (4.16), where p_1^x, p_2^x, and p_3^x are the coefficients of the polynomial.

$$\Delta L_{x_t} = p_1^x V_x + p_2^x V_x^2 + p_3^x V_x^3 \tag{4.16}$$

The piezoelectric sensitivity of the xy scanner in the x-direction, $K_{x_t}^l$, can be described by Eq. (4.17), where $K_{x_t}^s$ is the small signal piezoelectric sensitivity of the xy scanner in the x-direction, which is similar to Eq. (4.9), and α_{x_t} and β_{x_t} are the nonlinearity parameters of the xy scanner in the x-direction.

$$K_{x_t}^l = K_{x_t}^s + \alpha_{x_t} V_x + \beta_{x_t} V_x^2 \tag{4.17}$$

The lateral displacement of the xy scanner in the x-direction, ΔL_{x_t}, can be rewritten as Eq. (4.18), which is the multiplication of the piezoelectric sensitivity, $K_{x_t}^l$, by the applied voltage, V_x.

$$\Delta L_{x_t} = K_{x_t}^l V_x = K_{x_t}^s V_x + \alpha_{x_t} V_x^2 + \beta_{x_t} V_x^3 \tag{4.18}$$

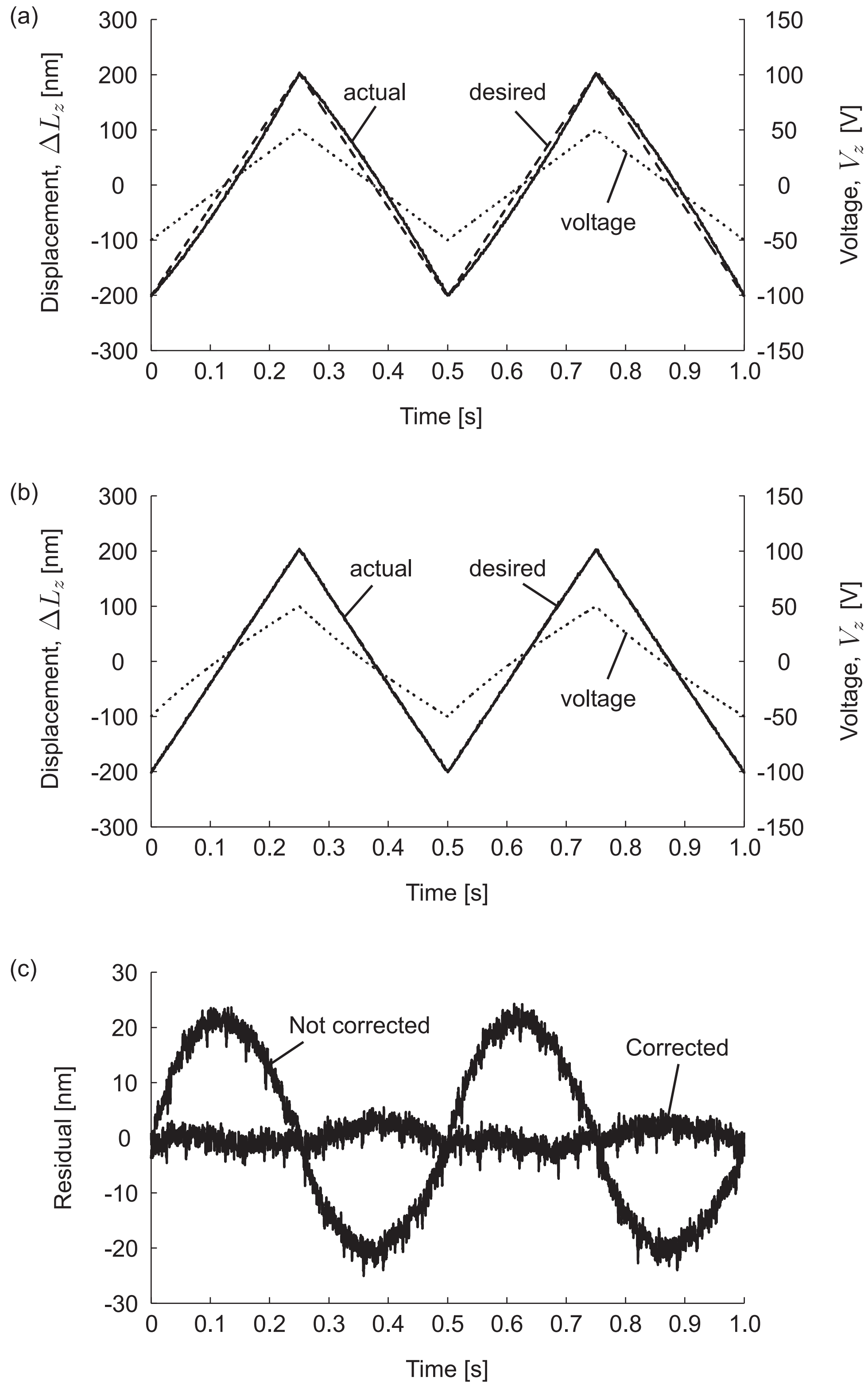

Figure 4.6: Nonlinearity correction with a preshaped waveform: (a) without correction, (b) with correction, and (c) residual plots.

It can be noticed that Eq. (4.18) has the same form as Eq. (4.16). Thus, by equating the coefficients of the polynomials, the small signal piezoelectric sensitivity, $K_{x_t}^s$, and the nonlinearity parameters, α_{x_t} and β_{x_t}, of the xy scanner in the x-direction can be determined.

It is also convenient to give the piezoelectric coefficient of the xy scanner in the x-direction, d_{31}^x, since it is independent of the dimension of the xy scanner and the length of the tip, L_t. Substituting the relations $K_{x_t}^l = \frac{2\sqrt{2}d_{31}^x(L_{xy}+2L_t)L_{xy}}{\pi Dt}$ and $K_{x_t}^s = \frac{2\sqrt{2}d_{31}^{xs}(L_{xy}+2L_t)L_{xy}}{\pi Dt}$ into Eq. (4.17), the piezoelectric coefficient, d_{31}^x, can be expressed as Eq. (4.19), where d_{31}^{xs} is the small signal piezoelectric coefficient of the xy scanner in the x-direction.

$$d_{31}^x = d_{31}^{xs} + \alpha_{x_t}\left(\frac{\pi Dt}{2\sqrt{2}\left(L_{xy}+2L_t\right)L_{xy}}\right)V_x + \beta_{x_t}\left(\frac{\pi Dt}{2\sqrt{2}\left(L_{xy}+2L_t\right)L_{xy}}\right)V_x^2 \quad (4.19)$$

Substituting d_{31}^x, Eq. (4.19), into the relation: $K_{x_t}^l = \frac{2\sqrt{2}d_{31}^x(L_{xy}+2L_t)L_{xy}}{\pi Dt}$, and then substituting $K_{x_t}^l$ into Eq. (4.18), the lateral displacement of the xy scanner in the x-direction, ΔL_{x_t}, can also be rewritten as Eq. (4.20).

$$\Delta L_{x_t} = \frac{2\sqrt{2}d_{31}^{xs}\left(L_{xy}+2L_t\right)L_{xy}}{\pi Dt}V_x + \alpha_{x_t}V_x^2 + \beta_{x_t}V_x^3 \quad (4.20)$$

It can also be noticed that Eq. (4.20) has the same form as Eq. (4.16). The small signal piezoelectric coefficient, d_{31}^{xs}, and the nonlinearity parameters, α_{x_t} and β_{x_t}, of the xy scanner in x-direction can also be determined by equating the coefficients of the polynomials. The formula for the lateral displacement of the xy scanner in the y-direction, ΔL_{y_t}, as a function of the applied voltage, V_y, can be obtained in a similar manner.

Figure 4.7 shows the hysteresis curves of the xy scanner in the x-direction for a triangular waveform input at various input frequencies, with an input voltage range of 200 V. The lateral displacement of the xy scanner in the x-direction depends slightly on the frequency of the driving signal. The corresponding lateral displacements (forward

hysteresis curves) of the xy scanner are plotted in Fig. 4.8. By fitting the 3rd-order polynomial of Eq. (4.16) to the each of the forward hysteresis curves in Fig. 4.8, the coefficients of the polynomial can be determined.

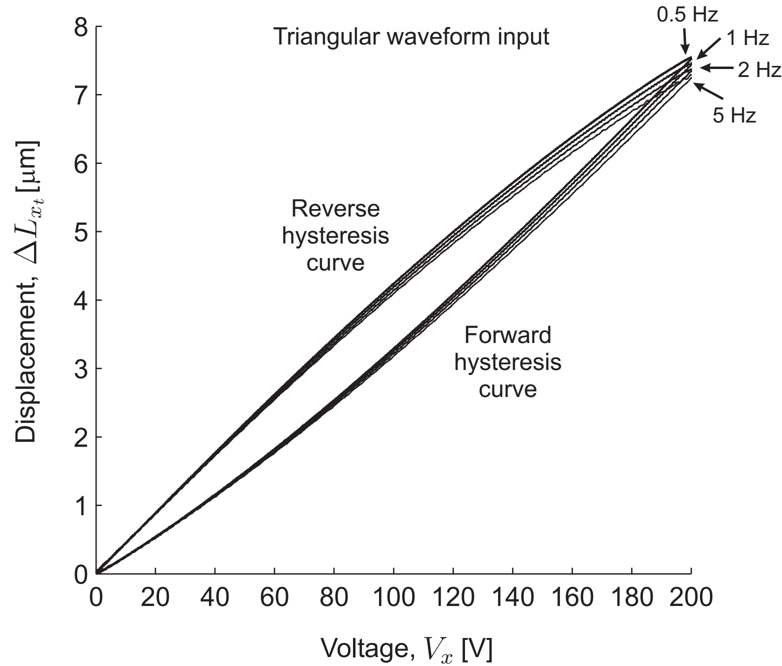

Figure 4.7: Hysteresis curves of the xy scanner in the x-direction for a triangular waveform input at various input frequencies.

The coefficients of the polynomial, and the calculated values of $K^s_{x_t}$, α_{x_t}, β_{x_t}, and d^{xs}_{31} (using the dimension of the xy scanner listed in Table 4.1), of the xy scanner in the x-direction for a triangular waveform input at various input frequencies, are listed in Table 4.3. The value of $K^s_{x_t}$ is based on a tip length L_t of 5 mm, and the value of d^{xs}_{31} is independent of the tip length L_t. Figure 4.9 shows a residual plot of the lateral displacement (forward hysteresis curve) of the xy scanner in the x-direction for a triangular waveform input at 5 Hz.

Similarly, the hysteresis curves of the xy scanner in the y-direction for a triangular waveform input at various input frequencies, with an input voltage range of 200 V, are shown in Fig. 4.10. The lateral displacement of the xy scanner in the y-direction also depends slightly on the frequency of the driving signal. The corresponding lateral

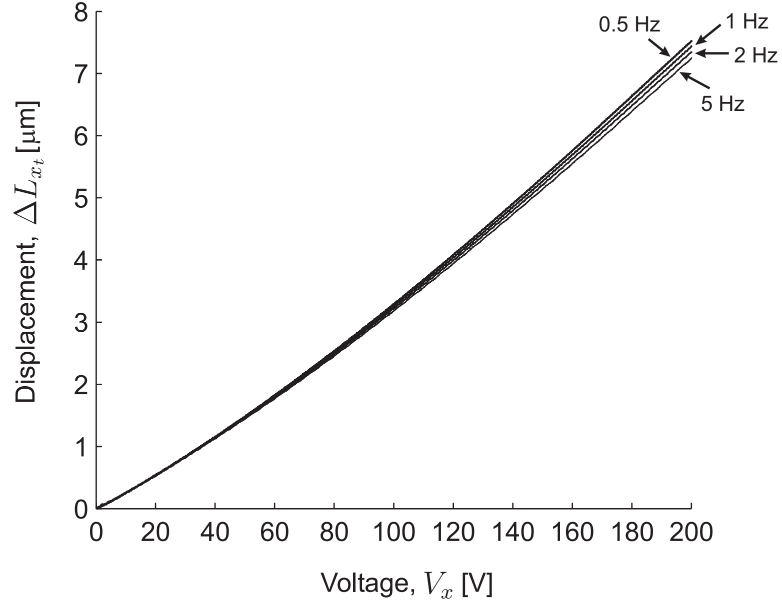

Figure 4.8: Lateral displacement (forward hysteresis curve) of the xy scanner in the x-direction for a triangular waveform input at various input frequencies.

Table 4.3: Polynomial coefficients and calculated values of $K^s_{x_t}$, α_{x_t}, β_{x_t}, and d^{xs}_{31}, of the xy scanner in the x-direction for a triangular waveform input at various input frequencies

Frequency (Hz)	$p^x_1 = K^s_{x_t}$ (nm/V)	$p^x_2 = \alpha_{x_t}$ (nm/V^2)	$p^x_3 = \beta_{x_t}$ (nm/V^3)	d^{xs}_{31} (nm/V)
0.5	26.330	7.753×10^{-2}	-10.306×10^{-5}	0.213
1.0	26.097	7.608×10^{-2}	-10.083×10^{-5}	0.211
2.0	25.869	7.449×10^{-2}	-9.846×10^{-5}	0.209
5.0	25.563	7.237×10^{-2}	-9.454×10^{-5}	0.207

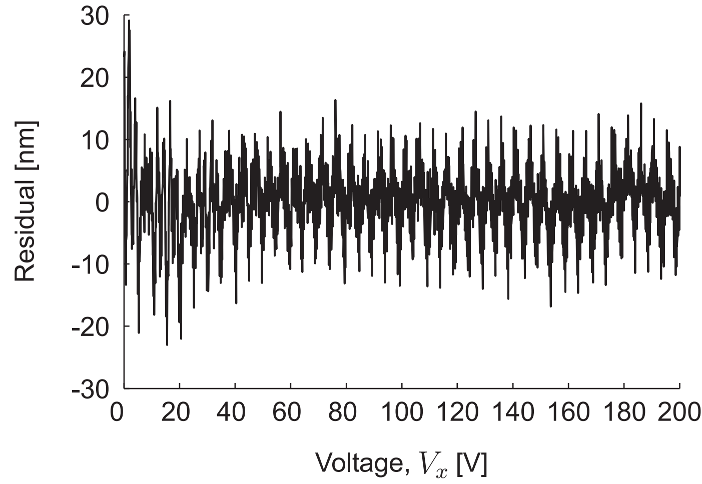

Figure 4.9: Residual plot of the lateral displacement (forward hysteresis curve) of the xy scanner in the x-direction for a triangular waveform input at 5 Hz.

displacements (forward hysteresis curves) of the xy scanner are plotted in Fig. 4.11. By fitting a 3rd-order polynomial to the each of the forward hysteresis curves in Fig. 4.11, the coefficients of the polynomial can be found.

The coefficients of the polynomial, and the calculated values of $K_{y_t}^s$, α_{y_t}, β_{y_t}, and d_{31}^{ys}, of the xy scanner in the y-direction for a triangular waveform input at various input frequencies, are listed in Table 4.4. The value of $K_{y_t}^s$ is based on a tip length L_t of 5 mm, and the value of d_{31}^{ys} is independent of the tip length L_t.

Table 4.4: Polynomial coefficients and calculated values of $K_{y_t}^s$, α_{y_t}, β_{y_t}, and d_{31}^{ys}, of the xy scanner in the y-direction for a triangular waveform input at various input frequencies

Frequency (Hz)	p_1^y = $K_{y_t}^s$ (nm/V)	p_2^y = α_{y_t} (nm/V^2)	p_3^y = β_{y_t} (nm/V^3)	d_{31}^{ys} (nm/V)
0.1	27.988	7.984 $\times$ 10^{-2}	-9.816 $\times$ 10^{-5}	0.226
0.5	27.443	7.591 $\times$ 10^{-2}	-9.347 $\times$ 10^{-5}	0.222
1.0	27.117	7.526 $\times$ 10^{-2}	-9.264 $\times$ 10^{-5}	0.219
2.0	26.882	7.348 $\times$ 10^{-2}	-8.897 $\times$ 10^{-5}	0.217

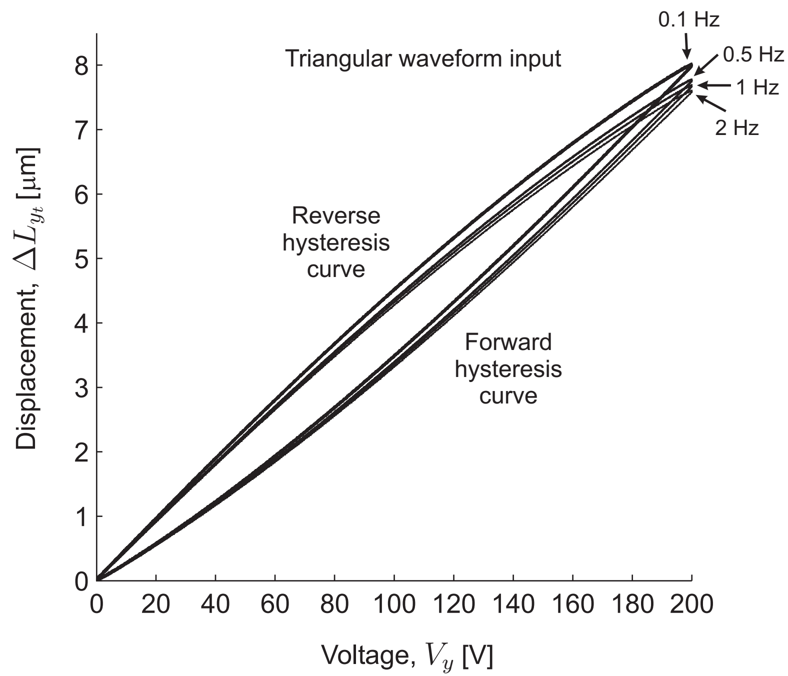

Figure 4.10: Hysteresis curves of the xy scanner in the y-direction for a triangular waveform input at various input frequencies.

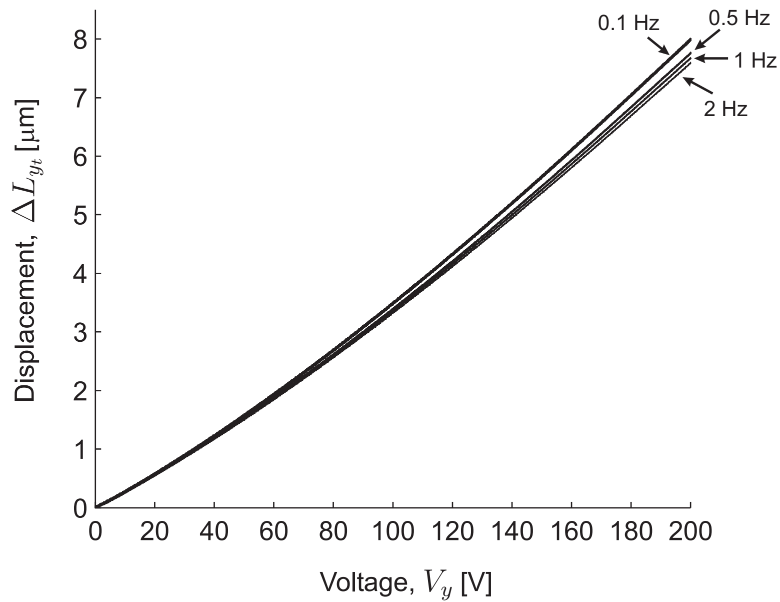

Figure 4.11: Lateral displacement (forward hysteresis curve) of the xy scanner in the y-direction for a triangular waveform input at various input frequencies.

4.3 Design and Construction of Instrument

Figure 4.12(a) shows the assembly of the entire system. A better view of the assembly is given in Fig. 4.12(b), but without the Ø14.0 cm aluminum tube enclosure. The structure is primarily made of aluminum. The system is for future installation in the UHV chamber as decribed in Chapter 2. Figure 4.12(b) shows that a floated stage assembly is suspended on three extension springs from the top of the Ø14.0 cm aluminum tube enclosure. This provides a single-stage vibration isolation system that isolates the instrument from external vibrations of the UHV chamber. A better view of the vibration isolation system is provided in Fig. 4.13.

The floated stage assembly, shown in Fig. 4.14, consists of the loadable instrument assembly, a heater assembly, an electrical connector assembly, and a Ø11.4 cm stainless steel plate. The loadable instrument assembly, shown in Fig. 4.15, consists of the instrument and a stainless steel structure with three hardened stainless steel hemispherical balls mounted on the bottom side of the structure. These hemispherical balls form a kinematic coupling [153] with the three vee-grooves made of tungsten carbide that are mounted on the Ø11.4 cm stainless steel plate. The kinematic coupling, together with a mechanical grounding mechanism as shown in Fig. 4.12(b), and a vacuum chamber load-lock transfer mechanism (not shown in these figures) will be added as an upgrade of the system to enable the transfer of the loadable instrument assembly into the UHV chamber. The heater assembly consists of a UHV heater (HeatWave Labs, TB-175) for radiative heating of the sample, and it remains to be an upgrade if needed.

On the bottom side of the floated stage assembly, three copper plates are mounted on the Ø11.4 cm stainless steel plate. These copper plates are placed with an equal radial distance from the center of the circular plate and are angularly spaced 120° apart. The copper plates together with six square samarium-cobalt magnets (Type 2-17) are for eddy current damping of the floated stage assembly. The arrangement of the copper plates and the magnets can be seen in Fig. 4.13, with a pair of magnets for each copper plate. The dimensions (length $\times$ width $\times$ thickness) of the copper plate and the magnet

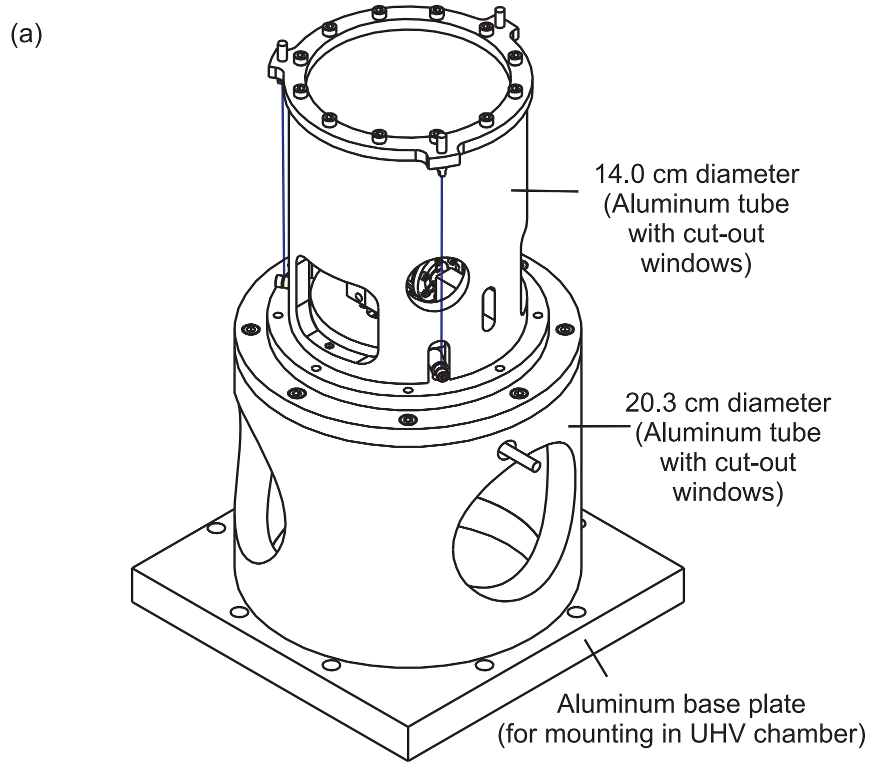

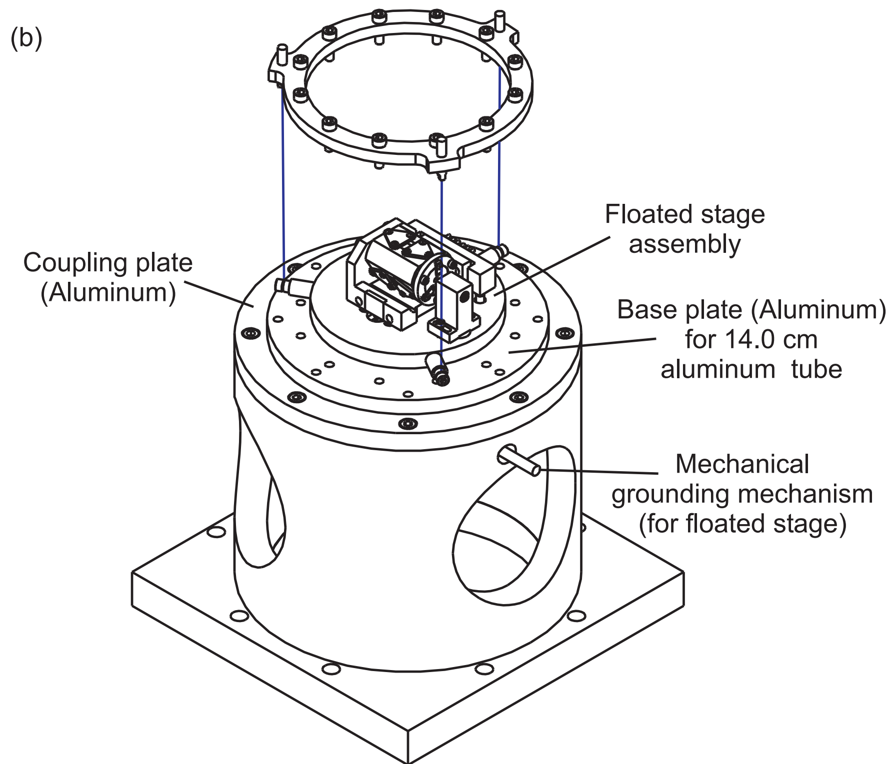

Figure 4.12: Assembly of the entire system.

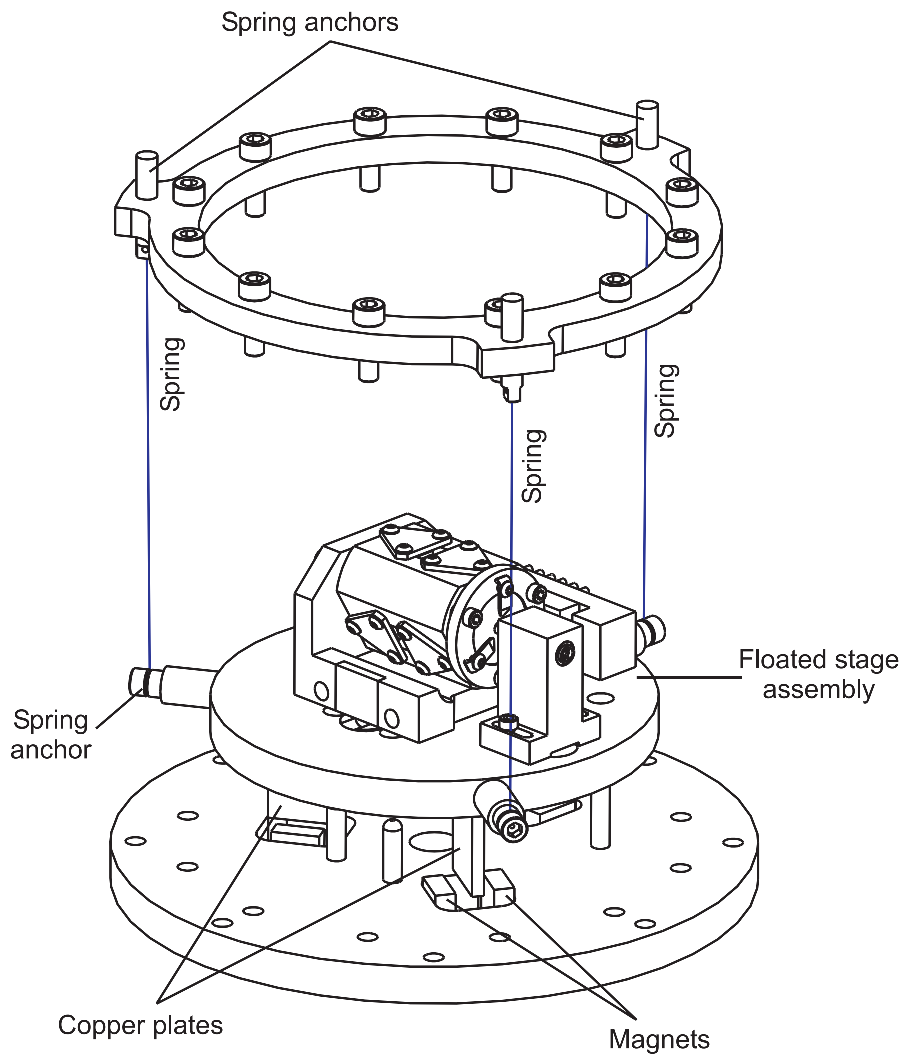

Figure 4.13: Single-stage vibration isolation with eddy current damping.

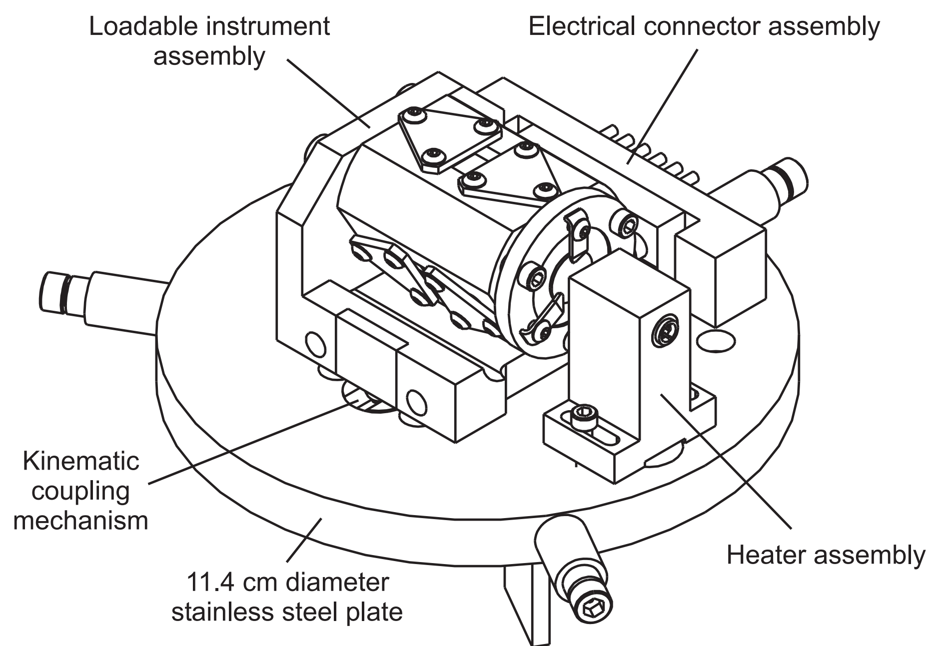

Figure 4.14: Floated (springs suspended) stage assembly.

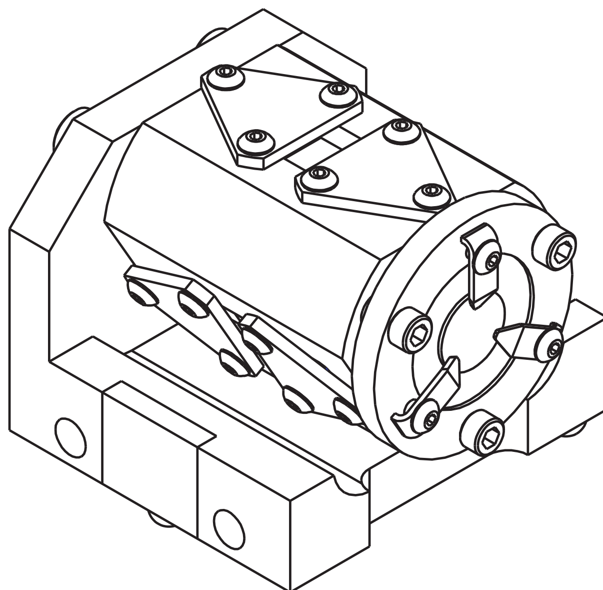

Figure 4.15: Loadable instrument assembly.

are (27.94 $\times$ 19.05 $\times$ 3.18) mm and (12.7 $\times$ 12.7 $\times$ 5.33) mm, respectively. Each pair of the magnets, spaced about 10 mm apart, is capable of producing a minimum magnetic field of 0.255 Tesla along the center axis.

Damping forces are generated by the eddy currents induced in the copper plates, when the copper plates move in the magnetic field created by the magnets. When the copper plates move parallel to the magnets, the damping constant c can be calculated with Eq. (4.21), where B is the magnetic field in Tesla, S is the cross sectional area of the magnets in m^2, t_c is the thickness of the copper plate in m, and ρ_c is the resistivity of the copper plate in Ωm [154]. The dimensionless constant C_0 depends on the geometry of the copper plate and the magnet. Typically, values of C_0 are between 0.1 and 0.5 [154].

$$c = \frac{B^2 S t_c C_0}{\rho_c} \tag{4.21}$$

Table 4.5: Physical parameters of the instrument's eddy current damper

Parameter	Value
Magnetic field, B (Tesla)	0.255
Cross sectional area of the magnets, S (m^2)	1.613 $\times$ 10^{-4}
Thickness of the copper plate, t_c (m)	0.00318
Resistivity of the copper, ρ_c (Ωm)	1.56 $\times$ 10^{-8}
Dimensionless constant, C_0	0.31[a]

[a]estimated from Ref. [154]

The physical parameters of the instrument's eddy current damper are listed in Table 4.5, and based on these values, the damping constant c is predicted to be 0.66 Ns/m. Since there are three copper plates, the total damping constant c_2 of the damping system becomes 1.98 Ns/m. The floated stage assembly is suspended by three extension springs of equal stiffness. It is important for the floated stage assembly to have a center-of-mass at the center of these springs, to avoid tilting of the floated stage assembly. The total stiffness k_2 of the extension springs is 142 N/m, and the total mass m_2 of the floated stage assembly is about 1.34 kg. Therefore, the resonant frequency f_2 of the single-stage vibration isolation is 1.64 Hz, which corresponds to

$\omega_2 = 2\pi f_2 = 10.3$ rad/s. The total length L_s of the springs after stretching is about 14.58 cm. These calculated values of the vibration isolation system are used in Section 4.4.

The piezoelectric tube scanner assembly that provides the three-dimensional fine motion of the tip is shown in Fig. 4.16(a), and it is also shown in the photograph of Fig. 4.3(b). The tip holder is a stainless steel tube with an inner diameter of 0.5 mm, and it is also provides the electrical connection. The tip holder is designed for holding 0.5 mm diameter tungsten wire, which is also the wire used for making the tip or field emitter. The diameter of the tungsten wire is actually slightly larger than the inner diameter of the tip holder. To ensure a tight press fit of the tip or emitter, it is required to electrochemically etch the tungsten wire slightly so that the end of the wire is of a tapered shape, which helps with the insertion of the wire into the tip holder.

The tip holder is glued to a cylindrical macor block using a UHV-compatible epoxy (Torr-Seal from Varian, Inc.) so that the axis of the tip coincides with the axis of the piezoelectric tube scanner. The macor block, together with the tip holder, is mounted at end of the tube scanner, which also serves as an electrical insulator for the tip. Another cylindrical macor block (scanner support) is mounted to the base of the tube scanner using the same epoxy, which also serves as an electrical insulator as well as the coupler to the alumina prism of the piezoelectric linear motor.

An exploded view of the instrument is shown in Fig. 4.16(a). The scanner support is designed for a tight fit to the alumina prism with a shoulder for alignment so that the axis of the tube scanner coincides with the axis (thermal center) of the piezoelectric linear motor that provides coarse positioning. The scanner support, including the tube scanner assembly, is mounted at the rear end of the alumina prism using Torr-Seal epoxy. Figure 4.16(b) demonstrates the assembly.

The sample holder assembly, as shown in Fig. 4.16, consists of a macor disc with a hole at the center and three sample clips made of molybdenum. The sample clips are used for holding a sample against the macor disc. It is also used for making electrical connection with the sample. A sample can be held on either side of the macor disc. The sample holder assembly can be mounted to the front end of the piezoelectric

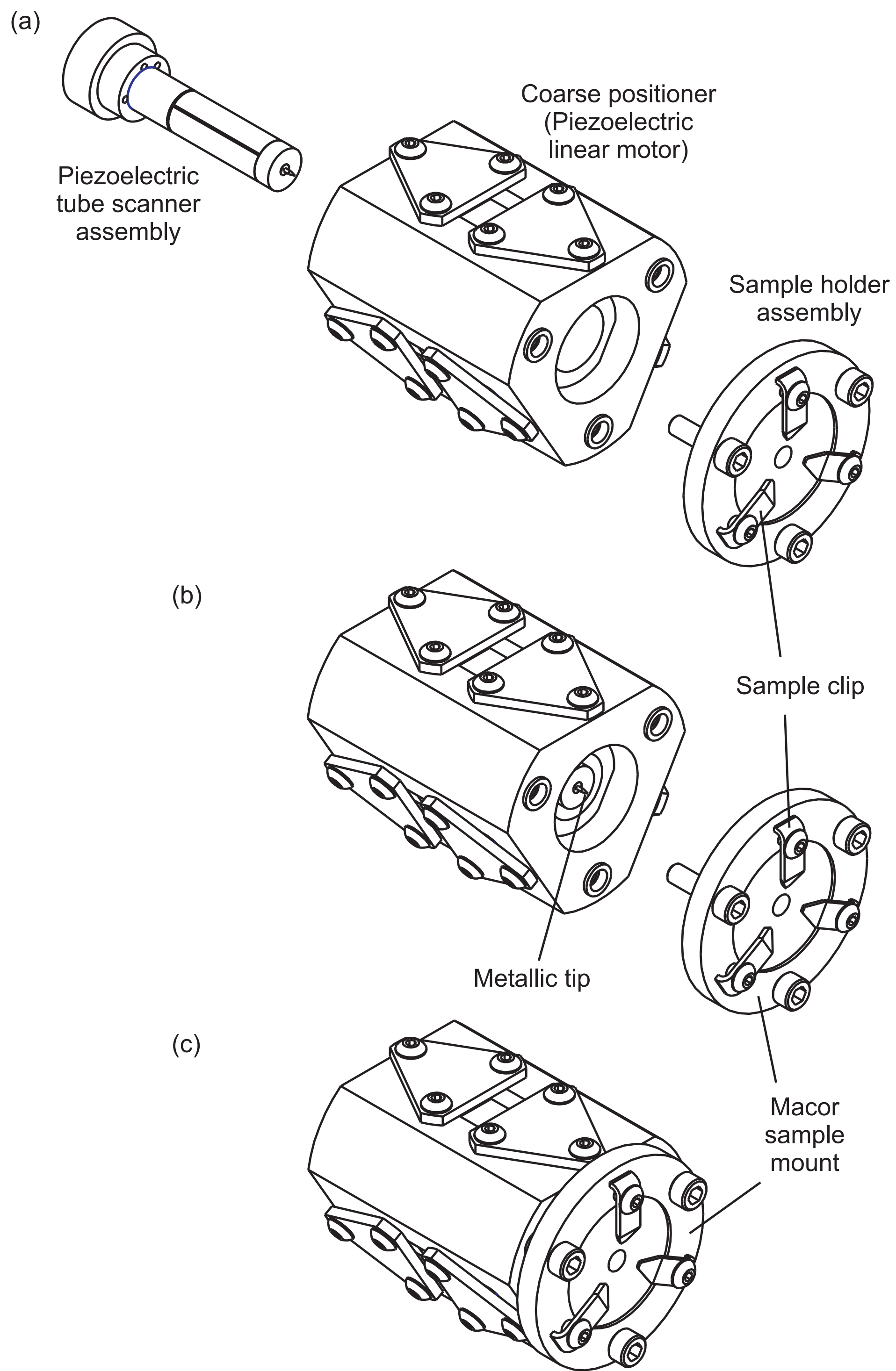

Figure 4.16: Assembly of the instrument: (a) exploded view, (b) exploded view with the piezoelectric tube scanner assembly mounted, and (c) unexploded of the instrument assembly.

linear motor with three screws. Figure 4.16(c) shows the complete assembly of the instrument. This symmetrical design for the instrument should have minimal thermal drift in the lateral (x, y) directions. A photograph of the instrument assembly with a tip mounted but no sample holder is given in Fig. 4.17.

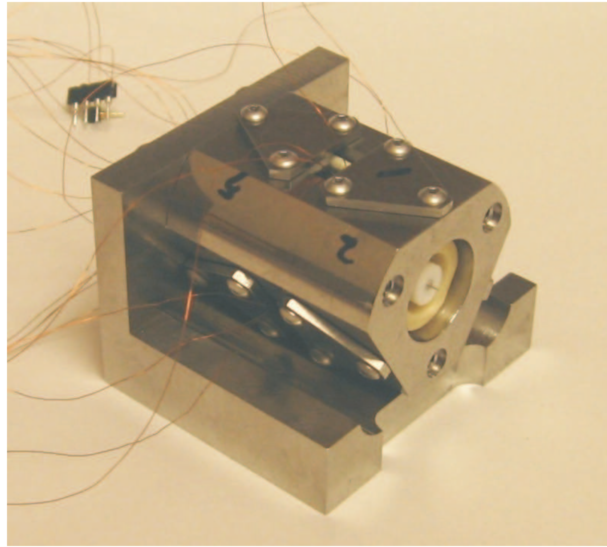

Figure 4.17: Photograph of the instrument assembly with tip or field emitter mounted but without the sample holder.

The materials used in the construction of the instrument have low coefficients of thermal expansion (CTE) to ensure good thermal stability. Low thermal drift between the tip and the sample surface in the axial (z) direction of the instrument is accomplished by using a compensating structure. From Chapter 3, one can assume that the thermal center (TC) plane of the piezoelectric linear motor along the axial (z) direction is at the mid-plane between the front and rear preload planes. This TC plane is used to estimate the thermal drift between the tip and the sample surface as shown in Fig. 4.18.

The thermal expansion sensitivity of the sample surface from the TC, τ_s, is given by Eq. (4.22). The dimensional parameters and the CTE values are tabulated in Table 4.6.

$$\tau_s = \alpha_{In} L_{In} + \alpha_m L_{ms} \tag{4.22}$$

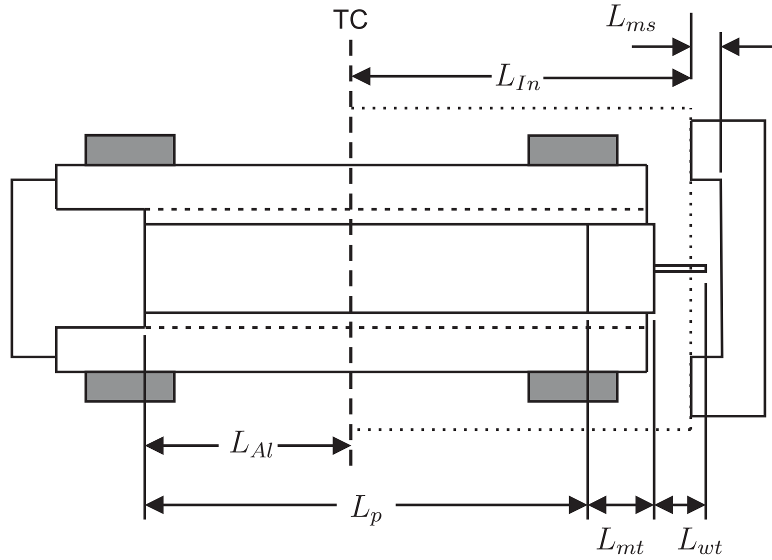

Figure 4.18: Axial thermal stability of the instrument using a compensating structure.

The thermal expansion sensitivity of the tip from the TC, τ_t, is given by Eq. (4.23).

$$\tau_t = -\alpha_{Al} L_{Al} + \alpha_p L_p + \alpha_m L_{mt} + \alpha_w L_{wt} \tag{4.23}$$

Thus, the thermal expansion sensitivity between tip and sample surface, τ_{st}, can be calculated using Eq. (4.24).

$$\tau_{st} = \tau_s - \tau_t \tag{4.24}$$

If the length of the tungsten tip is assumed to be 2.4 mm and the thermal expansion of the sample is neglected, then the thermal expansion sensitivity between the tip and the sample surface, τ_{st}, is approximately -7.8 nm/°C. For a tip length of 5.0 mm (L_{Al} = 12.265 mm), the thermal expansion sensitivity between the tip and the sample surface, τ_{st}, is approximately +0.8 nm/°C. These calculations were based on the sample being mounted on the inside of the macor disc. A positive sign means that the tip and the sample are moving away from each other with increasing temperature or vice verse.

The resonant frequency of the piezoelectric tube scanner assembly was determined

Table 4.6: Dimensional parameters and coefficients of thermal expansion (CTE)

CTE of invar, α_{In} (/°C)	1.72×10^{-6}
CTE of macor, α_m (/°C)	9.3×10^{-6}
CTE of alumina, α_{Al} (/°C)	7.8×10^{-6}
CTE of PZT-5A, α_p (/°C)	2.0×10^{-6a}
CTE of tungsten, α_w (/°C)	4.5×10^{-6}
Effective length of invar, L_{In} (mm)	18.034
Effective length of macor (invar to sample), L_{ms} (mm)	4.572[b]
Effective length of macor (invar to sample), L_{ms} (mm)	2.032[c]
Effective length of alumina prism, L_{Al} (mm)	9.665[d]
Length of piezoelectric tube scanner, L_p (mm)	24.13
Length of macor (tube scanner to tip), L_{mt} (mm)	2.591
Length of tungsten tip, L_{wt} (mm)	2.4[e]

[a]based on isotropic property
[b]sample mounted on the outside
[c]sample mounted on the inside
[d]for tungsten tip length given in [e]
[e]assume tungsten tip length

using finite element analysis (ProMechanica). It was found that the lowest resonant frequency of the assembly is 3.82 kHz), corresponding to the bending mode of the tube scanner, as shown in Fig. 4.19.

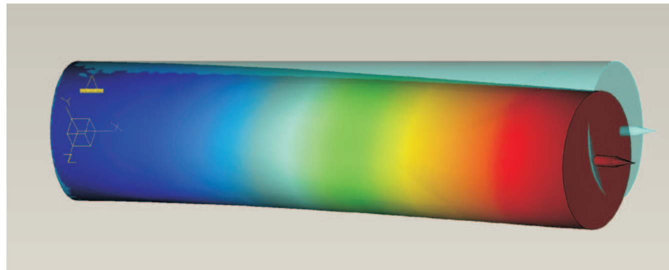

Figure 4.19: Bending mode of the piezoelectric tube scanner assembly.

The axial (z) stiffness of the piezoelectric linear motor was measured experimentally to be about 15.55 N/μm. The total mass of the piezoelectric tube scanner assembly, the alumina prism, and the driving mechanisms is about 24.3 grams. The calculation of the resonant frequency is rather straightforward. The resonant frequency f_n of the instrument in the axial (z) direction was determined to be 4.03 kHz or $\omega_n = 2\pi f_n =$

25.3×10^3 rad/s.

4.4 Vibration Isolation

Vibration isolation is another essential component of the instrument, especially when operating the instrument in STM mode. Floor vibration can transmit through the structure and into the instrument affecting the performance. The amplitude of the floor vibration is typically a few thousand angstroms for low frequency components [154]. A vibration isolation with an attenuation of at least 10^{-5} is required in order to attenuate the vibration level to below 0.5 Å [9]. Often, a component can have many degrees of freedom, which makes it difficult to trace all the motions. In general, analyzing one or two motions of the components will decribe the entire system effectively.

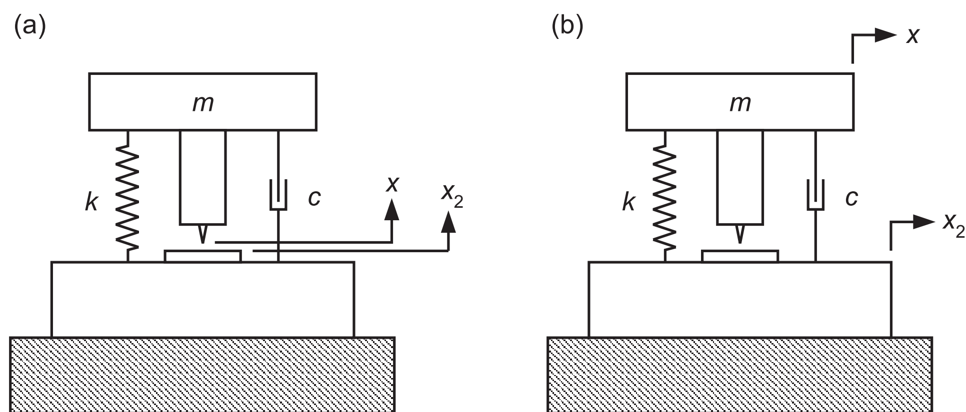

Figure 4.20: Model of the instrument in STM mode: (a) axial (z) direction and (b) lateral (x, y) directions. The system has been reduced to a simple damped harmonic oscillator.

In order to understand the tolerable level of mechanical vibration and how much vibration isolation is required, the mechanical system of the instrument (in STM mode operation) must first be examined. As illustrated in Fig. 4.20, the model of the instrument includes the sample, the sample holder, the tip-sample approach mechanism (piezoelectric linear motor), the piezoelectric tube scanner, and the tip. The system has been reduced to a simple damped harmonic oscillator. The equation of motion can be written in the form given in Eq. (4.25), where m is the effective mass, c is the damping

factor, k is the spring constant, x is the motion of the tip, and x_2 is the motion of the sample or instrument structure. The relative motion of the tip-sample junction is given by ($x - x_2$).

$$m\ddot{x} + c\left(\dot{x} - \dot{x}_2\right) + k\left(x - x_2\right) = 0 \tag{4.25}$$

To simpify the analysis, the resonant frequency ω_n and the damping ratio ζ of the system are defined as Eq. (4.26) and Eq. (4.27), respectively.

$$\omega_n = \sqrt{\frac{k}{m}} \tag{4.26}$$

$$\zeta = \frac{c}{2m\omega_n} \tag{4.27}$$

Using these relations, Eqs. (4.26) and (4.27), the equation of motion Eq. (4.25) can be rewritten as Eq. (4.28).

$$\ddot{x} + 2\zeta\omega_n\left(\dot{x} - \dot{x}_2\right) + \omega_n^2\left(x - x_2\right) = 0 \tag{4.28}$$

When the structure of the instrument is excited harmonically, $x_2\left(t\right) = X_2 e^{i\omega t}$, the steady state harmonic solution $x\left(t\right) = X e^{i\omega t}$ can be used to obtain the relationship between the variation in ($X - X_2$) and the excitation amplitude (X_2). Or, equivalently, taking the Laplace transform of Eq. (4.28) and replacing $s = -i\omega$. The complex frequency response or transfer function (transmissibility) then becomes Eq. (4.29). The solution can also be found in many vibration textbooks [155, 156].

$$T_1\left(\omega\right) = \frac{\left(X - X_2\right)}{X_2} = \frac{\omega^2}{\omega_n^2 - \omega^2 + 2\zeta\omega_n i\omega} \tag{4.29}$$

For the mechanical vibration in the axial z direction of the instrument, as shown in Fig. 4.20(a), $T_1\left(\omega\right)$ is the response of the tip normal to the sample surface (gap distance) to a periodic external vibration or excitation. The resonant frequency ω_n of instrument in the axial z direction has been calculated in the previous section and it was determined to be 25.3 $\times 10^3$ rad/s (or f_n = 4.03 kHz). To be conservative, the damping

ratio ζ is assumed to be 0.05, which is reasonable for inherent structural damping of the instrument. The frequency response of the tip normal to the sample surface (gap distance) to external vibrations is plotted in Fig. 4.21.

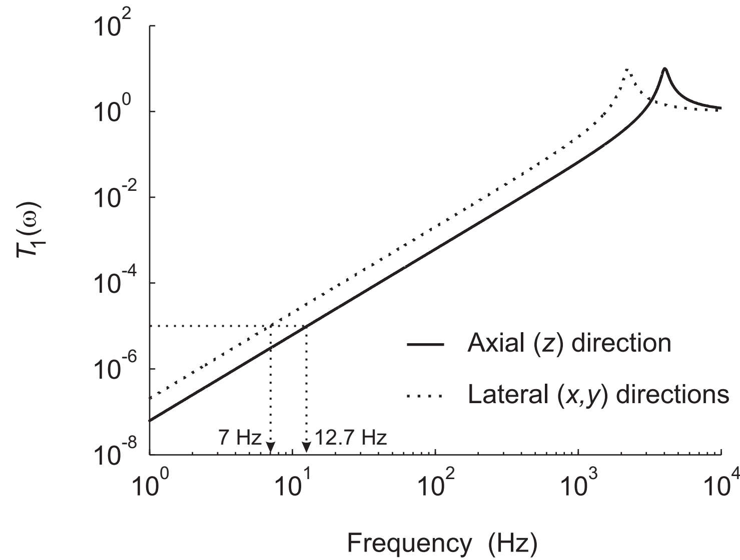

Figure 4.21: Frequency response of the instrument to external mechanical vibrations.

Similarly, the mechanical vibration in the lateral (x, y) directions of the instrument, as shown in Fig. 4.20(b), $T_1(\omega)$ is the response of the tip parallel to the sample surface to an external vibration. To be conservative, the resonant frequency ω_n and the damping ratio ζ of the instrument in the lateral (x, y) directions are taken to be 13.9 $\times 10^3$ rad/s (or f_n = 2.2 kHz) and 0.05, respectively. These values are based on the lateral resonant frequency of the piezoelectric linear motor, from Chapter 3. The frequency response of the tip parallel to the sample surface to external vibrations is plotted in Fig. 4.21.

It can be seen from Fig. 4.21 that the transmissibility (relative motion of the tip to the sample surface) is less than $\times 10^{-5}$ for excitation frequencies below 7 Hz. This is adequate considering that the typical floor vibration amplitude is few thousand angstroms. For vibration frequencies above 10 Hz, it is obvious that a vibration isolation system is required.

The vibration isolation system shown in Fig. 4.13 can be modeled by the systems shown in Fig. 4.22. For simplicity, only the translational motion and the pendulum motion of the vibration isolation system are considered. These systems can be described in a similar manner as before. For the system shown in Fig. 4.22(a), the equation of motion can be written as Eq. (4.30). Equation (4.30) has the same form as Eq. (4.25), except that $x_1(t) = X_1 e^{i\omega t}$ is the external excitation (floor vibration) at the base of the vibration isolation system and $x_2(t) = X_2 e^{i\omega t}$ is the steady state harmonic solution of m_2, which is the mass of the floated stage assembly.

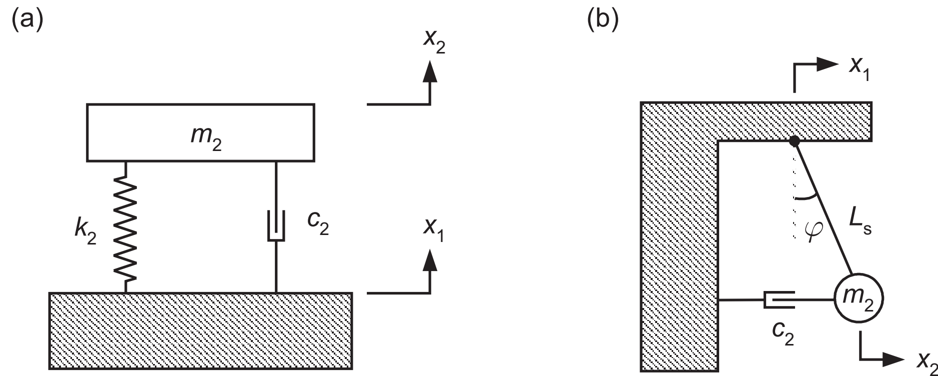

Figure 4.22: Model of a single-stage vibration isolation system. The vibration isolation system shown in Fig. 4.13 can be represented by (a) a translation system and (b) a pendulum system.

$$m_2\ddot{x}_2 + c_2(\dot{x}_2 - \dot{x}_1) + k_2(x_2 - x_1) = 0 \tag{4.30}$$

The amplitude ratio of X_2/X_1 is of interest, which is the vibrational amplitude attenuation of the system. The transfer function of the single-stage vibration isolation system is given by Eq. (4.31), where ω_2 and ζ_2 are given by Eq. (4.32) and Eq. (4.33), respectively.

$$T_2(\omega) = \frac{X_2}{X_1} = \frac{\omega_2^2 + 2\zeta_2\omega_2 i\omega}{\omega_2^2 - \omega^2 + 2\zeta_2\omega_2 i\omega} \tag{4.31}$$

$$\omega_2 = \sqrt{\frac{k_2}{m_2}} \tag{4.32}$$

$$\zeta_2 = \frac{c_2}{2m_2\omega_2} \tag{4.33}$$

The resonant frequency ω_2 has been determined in the previous section to be 10.3 rad/s (or f_2 = 1.64 Hz). The damping ratio ζ_2 can be calculated using Eq. (4.33). Recall that m_2 = 1.34 kg and c_2 = 1.98 Ns/m for the vibration isolation system. Thus, the damping ratio, ζ_2 = 0.072.

Similarly, the equation of motion for the pendulum system shown in Fig. 4.22(b) is written in Eq. (4.34) using $x_2 = x_1 + L_s\varphi$. The difference between Eq. (4.34) and Eq. (4.30) is $k_2 = m_2 g/L_s$, where L_s is the stretched length of the springs and g is the acceleration due to gravity.

$$m_2\ddot{x}_2 + c_2\left(\dot{x}_2 - \dot{x}_1\right) + \frac{m_2 g}{L_s}\left(x_2 - x_1\right) = 0 \tag{4.34}$$

The length L_s of the springs after stretching is 14.58 cm, thus the resonant frequency of the pendulum system is $\omega_2 = \sqrt{g/L_s} =$ 8.2 rad/s (or f_n = 1.31 Hz). And, the damping ratio ζ_2 of the pendulum system is assumed to be 0.05.

The magnitude of the product of $T_1(\omega)$ and $T_2(\omega)$, gives the amplitude ratio of $(X - X_2)/X_1$, which can be used to evaluate the response of the relative motion between the tip and the sample to external vibrations. The product $T_1(\omega)T_2(\omega)$ is plotted in Fig. 4.23.

It can be seen from Fig. 4.23, the vibration attenuation of the instrument in the axial (z) direction (gap distance) is better than $\times 10^{-5}$ for floor vibration frequencies of less than 1 kHz. The vibration attenuation in the lateral (y) direction (tip moves parallel to the sample surface) is at least $\times 10^{-4}$ for frequencies less than 1 kHz. Thus, a single-stage vibration isolation system is sufficient for the instrument considering that the amplitude of the floor vibration usually decreases as the frequency increases. It is interesting to note that the efficiency of a single-stage vibration isolation system solely depends on the ratio of ω_n and ω_2.

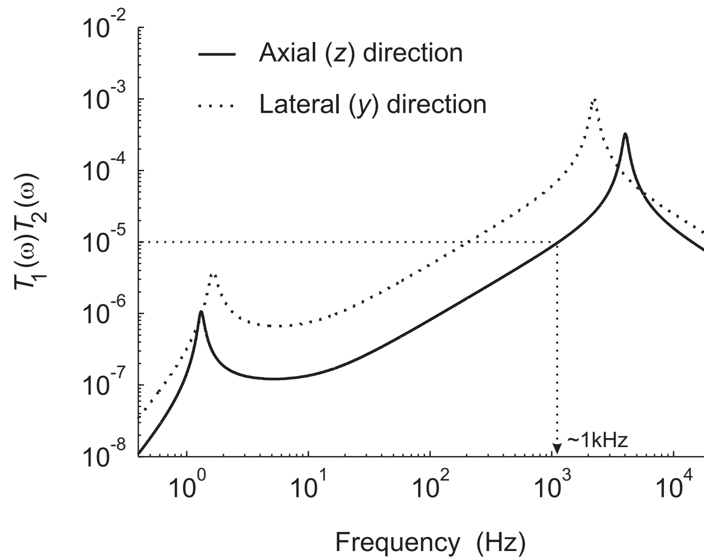

Figure 4.23: Vibration attennuation of the instrument combined with a single-stage vibration isolation system.

4.5 Preliminary Test of Instrument in STM mode

The ability of the instrument to scan the sample surface before and after writing/patterning by a field-emitted electron beam is an important feature of the instrument. This enables the detection of any surface modifications by the electron beam. Furthermore, it minimizes the step, time, and effort to verify any surface modifications by other high-resolution microscopes such as AFM, SEM, and transmission electron microscope (TEM). Thus, it is important to carry out the preliminary test of the instrument in STM mode to verify and ensure its capability to take reasonable surface images of a sample.

For operation of the instrument in STM mode, a commercially available SPM controller (RHK Technology, Model SPM 1000) was used to test the instrument. A photograph of the SPM controller is shown in Fig. 4.24. After reviewing the operator manual and electronic circuit diagrams of the controller, it was found that the SPM controller has a proportional gain controller followed by an integral controller (RC network, i.e. first-order (one-pole) low-pass filter). This is a common compensator used for feed-

back control of many existing STMs, and it was also used in the first STM [8] due to its simplicity. The proportional controller can be used to adjust the gain, and the RC network, which acts as an integrator, can be used to adjust the time constant (τ = RC). The adjustable ranges of the gain and time constant for the controller are (0 - 2) and (1 - 20) ms, respectively.

Figure 4.24: A photograph of a commercial universal SPM controller from RHK Technology.

The z-motion, which is the motion of the tip perpendicular to the sample surface, is controlled by negative feedback as schematically shown in the block diagram of Fig. 4.25. In a constant-current mode of operation, the gap separation between the tunneling tip and a sample surface is set by comparing the tunneling current $I(s)$ to the reference current $R(s)$ and is regulated by the feedback loop. $G_1(s)$, $G_2(s)$, $G_3(s)$, and $G_4(s)$ are the transfer functions of the proportional controller, the integral controller, the proportional controller (if there is one), and the high-voltage amplifier, respectively. For most systems, a proportional controller $G_3(s)$ is typically not used.

$H_1(s)$, $H_2(s)$, and $H_3(s)$ are the transfer functions for the piezoelectric z-scanner, the tunneling junction (gap), and the preamplifier (including the logarithmic amplifier

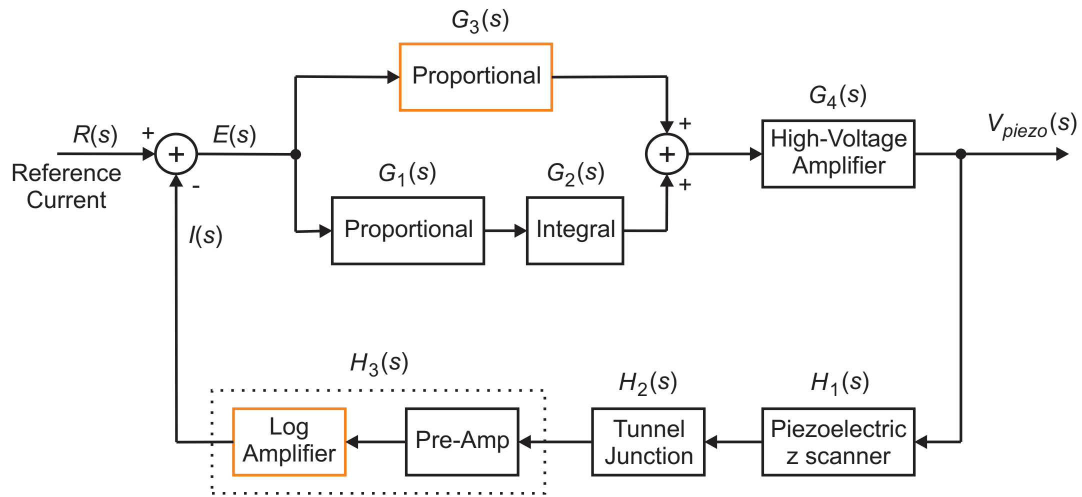

Figure 4.25: Block diagram of STM feedback control system.

if there is one), respectively. The motion of the tip can be obtained by multiplying the voltage signal $V_{piezo}(s)$ applied to the z-scanner by the piezoelectric sensitivity K_z given in Eq. (4.2) of the z-scanner, to obtain the topography of the sample surface. Linearization can be obtained with a logarithmic amplifier to help the feedback loop responds more linearly because of the exponential dependence of the tunneling current on the gap distance, but it is not necessarily required. In fact, a logarithmic amplifier was not used in these preliminary tests.

In order to bring the tip to within the range of the z-axis of the tube scanner, the universal SPM controller can be programmed to perform an automatic tip-sample approach routine. The procedure for automatic tip-sample approach is as follows: (1) disable the feedback loop and retract the z scanner fully, (2) take one step forward with the piezoelectric linear motor, and (3) activate the feedback loop, which will extend the z scanner automatically, if a tunneling current is detected, then stop. Otherwise, repeat the loop. In this way, the tip is automatically brought to within the tunneling range of the tip without crashing the tip into the sample surface.

The step size of the piezoelectric linear motor was set to about 100 nm. The rate of the linear motor during the automatic coarse approach was hence about 2-3 steps per

second. Typically, it will take one to three hours to complete the tip-sample approach, depending on the initial tip-sample separation distance. Once the sample is within the tunneling range of the tip, the gain and time constant of the controller are adjusted manually to prevent oscillation due to instability of the feedback loop. Improper setting of the proportional gain and time constant can cause feedback oscillation.

Figure 4.26 illustrates an axample of the feedback oscillations in the tunneling current due to improper gain and time constant settings of 1.3 and 6 ms, respectively. The oscillation frequency and amplitude are about 3.85 kHz and 2 nA, respectively, and the background high frequency signal is due to switching in the lighting and computer monitor. The feedback oscillation in the system can be alleviated by reducing the gain or by increasing the time constant.

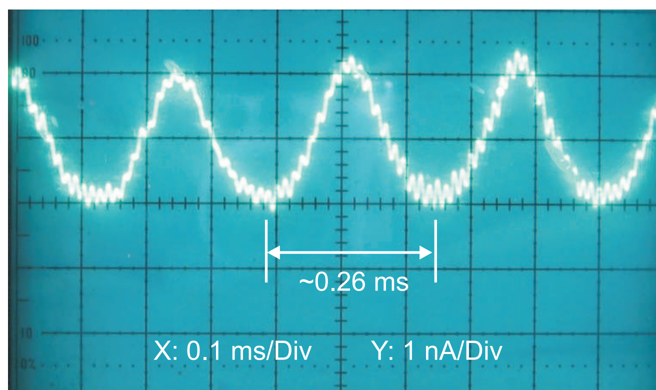

Figure 4.26: Feedback oscillation in the tunneling current due to improper gain and time constant settings at 1.3 and 6 ms, respectively.

The preliminary test of the instrument for operation in the STM mode was carried out using two types of samples, one made of highly ordered pyrolytic graphite (HOPG) and another one made of replicated holographic grating (Optometric, Inc.). The experiments were carried out in a rather poor vacuum condition of (10^{-2} to 10^{-3}) Torr with a single-stage vibration isolator, similar to the one shown in Fig. 4.13, along with a pneumatic isolation table. All images were taken with a bias voltage of 1 V applied to the sample and a reference current of 1 nA. The fast scan direction is in the x-axis (triangular

waveform) and the slow scan direction is in the y-axis (ramp).

For the HOPG, the length of the tungsten tip, measured from the end of the piezoelectric tube scanner, was about 5.0 mm. Thus, the piezoelectric sensitivities of the xy scanner based on small signals (0 - 10 V) in the x and y directions were taken to be the same with a value of 25 nm/V. The piezoelectric sensitivity of the z scanner, which is independent of the tip length, based on small signals (0 - 10 V), was taken to be 3 nm/V. The proportional gain and time constant of the controller were set to about 1.0 and 8 ms, respectively.

Figure 4.27 displays the two-dimensional and three-dimensional images of the HOPG surface, made up of 256 $\times$ 256 pixels, over a scan area of about 500 x 500 nm^2. These images were taken with a scan time of about 200 seconds. The image shown in Fig. 4.27(a) was recorded while scanning the tungsten tip to the right ($+x$ direction) and the image shown in Fig. 4.27(b) was recorded while scanning the tungsten tip to the left ($-x$ direction). It is clear that these images show remarkable similarity, which means the instrument is operating properly in the STM mode. However, these images appear distorted slightly, which is due to nonlinearity and hysteresis in the piezoelectric tube scanner. Correction or compensation to the distortion and the slope in these images was not attempted.

A separate scan over a smaller area of the HOPG surface was also conducted at the upper left quadrant of Fig. 4.27(a) using the same scan settings as before. Figure 4.28 shows the two-dimensional and three-dimensional images of the HOPG surface for the zoom-in scan area of about 250 x 250 nm^2. Similarly, the image shown in Fig. 4.28(a) was recorded while scanning the tungsten tip to the right ($+x$ direction) and the image shown in Fig. 4.28(b) was recorded while scanning the tungsten tip to the left ($-x$ direction). These images show remarkable similarity and review greater detail of the features on the HOPG surface, which proves that the instrument is operating properly in the STM mode. The distortion in these images are less, which is to be expected since the nonlinearity and the hysteresis in the piezoelectric tube scanner are minimal for smaller scan areas.

The surface corrugation (profile) between point A and point B of the HOPG surface

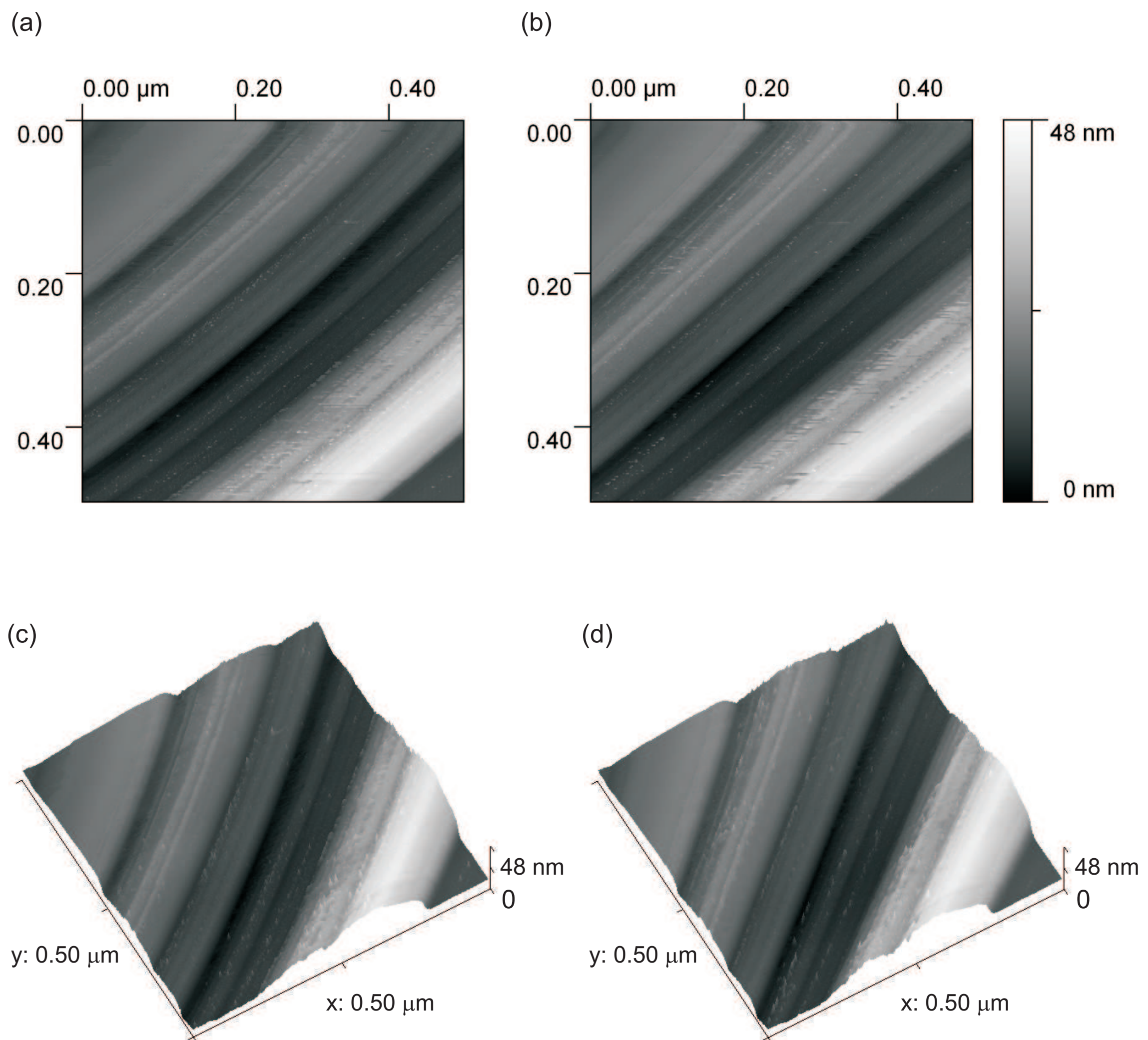

Figure 4.27: STM images of the HOPG surface for a scan area of about 500 x 500 nm^2. (a) Image recorded while scanning the tungsten tip to the right ($+x$ direction), (b) image recorded while scanning the tungsten tip to the left ($-x$ direction), (c) the corresponding three-dimensional image of the image in (a), and (d) the corresponding three-dimensional image of the image in (b).

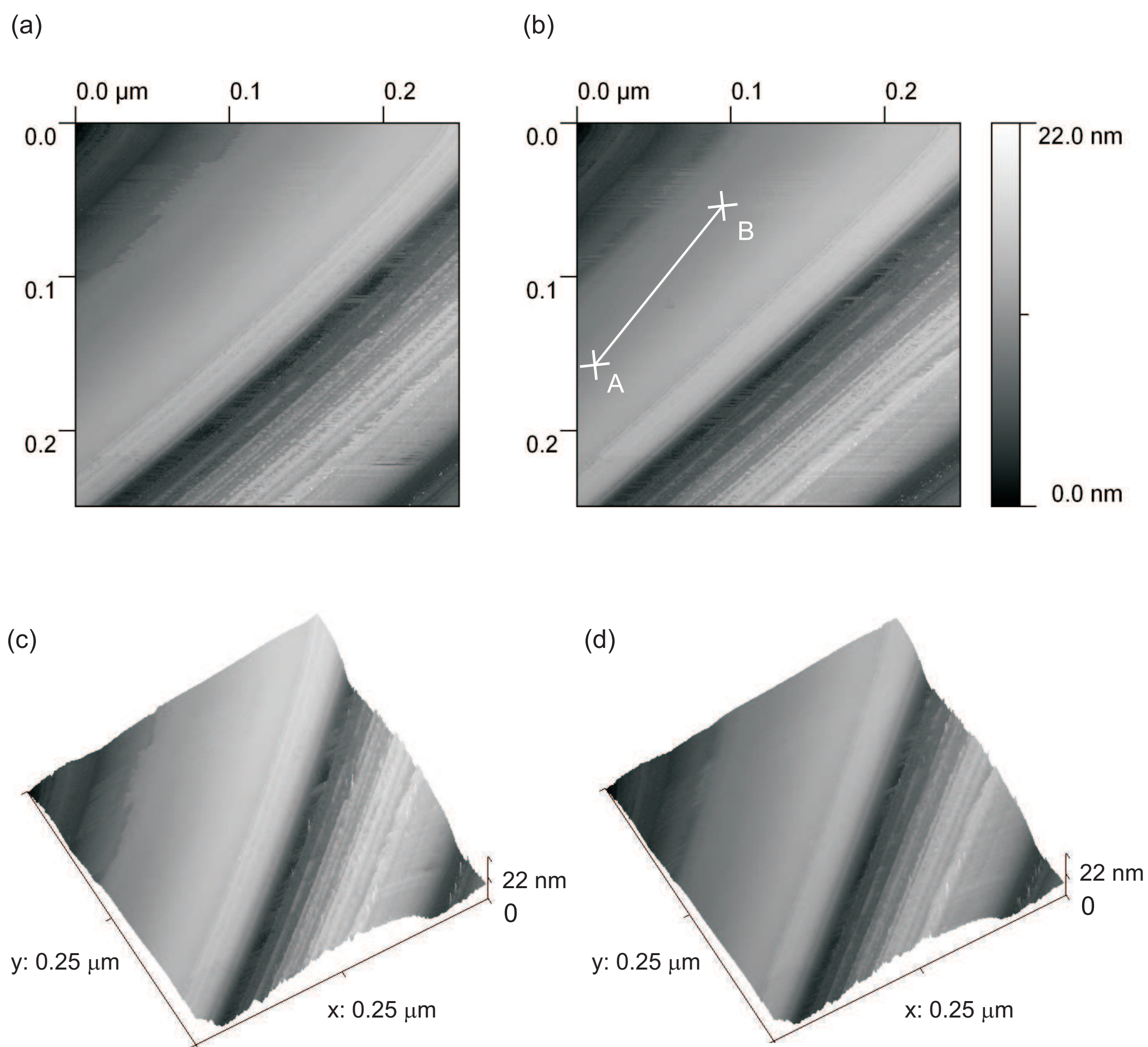

Figure 4.28: STM images of the HOPG surface for a smaller scan area of about 250 x 250 nm^2. (a) Image recorded while scanning the tungsten tip to the right ($+x$ direction), (b) image recorded while scanning the tungsten tip to the left ($-x$ direction), (c) the corresponding three-dimensional image of the image in (a), and (d) the corresponding three-dimensional image of the image in (b).

given in Fig. 4.28(b) is plotted in Fig. 4.29. A cleaved HOPG surface is known to have atomically flat surfaces as well as steps (terraces). Although the profile shows no atomic features due to large scan area (compared to the atomic imaging scan area of typically on the order of a few nanometers), the profile shows a surface height variation of about 2 Å over a distance of about 130 nm. Thus, one can conclude that the instrument has a resolution of better than 2 Å in the z direction, considering that the experiment was conducted in a rather poor vacuum condition.

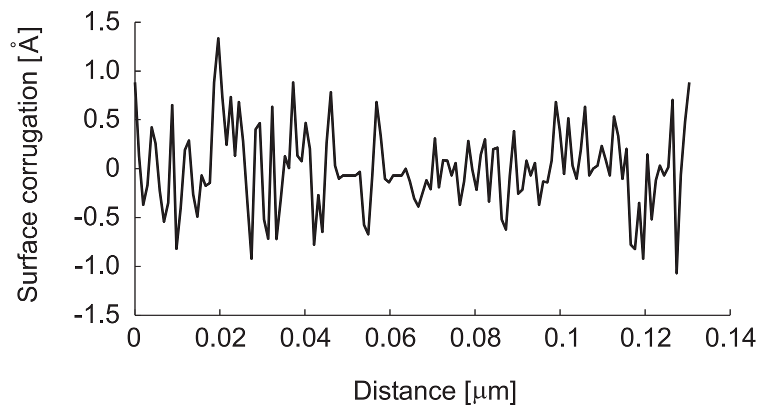

Figure 4.29: Surface corrugation (profile) between point A and point B of the HOPG surface (refer to Fig. 4.28(b)).

For the holographic grating, the length of the tungsten tip was about 4.6 mm. Thus, the piezoelectric sensitivities of the xy scanner based on small signals in the x and y directions are both about 25 nm/V. The piezoelectric sensitivity of the z scanner was taken to be 3 nm/V, based on small signals. The proportional gain and time constant of the controller were set to (0.6 - 1.0) and (10 - 12) ms, respectively. The holographic grating is a replicated grating covered (deposited) with a thin film of gold. It has 3600 grooves per millimeter, which corresponds to a pitch of 278 nm. The height (amplitude) of the grooves is 110 nm.

Figure 4.30 demonstrates the two-dimensional and three-dimensional images of the grating surface, made up of 256 $\times$ 256 pixels, for a scan area of about 260 x 260 nm^2. These images were taken with a scan time of about 500 seconds. The image shown in

Fig. 4.30(a) was recorded while scanning the tungsten tip to the right ($+x$ direction) and the image shown in Fig. 4.30(b) was recorded while scanning the tungsten tip to the left ($-x$ direction). Similarly, these images show remarkable similarity regardless of the scan directions for a fairly rough surface. Gold clusters or islands, measuring between 20 nm and 30 nm, are clearly visible on the grating surface, which is not uncommon for a thermally evaporated thin gold layer.

A larger scan area of about 660 x 660 nm^2 of the grating surface is shown in Fig. 4.31. The image shown in Fig. 4.31(a) was recorded while scanning the tungsten tip to the right ($+x$ direction) and the image shown in Fig. 4.31(b) was recorded while scanning the tungsten tip to the left ($-x$ direction), and Figs. 4.31(c) and (d) show the corresponding three-dimensional images of the grating surface. These images were taken with a scan time of about 1300 seconds. The grooves of the grating are clearly visible, and the images also show remarkable similarity regardless of the scan directions.

Figure 4.32 shows the two-dimensional and three-dimensional images of the grating surface for an even larger scan area of about 2.09 x 2.09 μm^2. These images were recorded with a scan time of about 2050 seconds. The image shown in Fig. 4.32(a) was recorded while scanning the tungsten tip to the right ($+x$ direction) and the image shown in Fig. 4.32(b) was recorded while scanning the tungsten tip to the left ($-x$ direction). There are about 8.5 grooves in these images. The distortion due to nonlinearity and hysteresis in the piezoelectric tube scanner is clearly visible. Nevertheless, the images clearly indicate the features on the grating surface.

Three profiles, Profile 1, Profile 2, and Profile 3, demonstrating the surface height of the grating surface for the image given in Fig. 4.32(a), are plotted in Fig. 4.33. It is obvious that the grating sample is tilted. Nevertheless, the profiles clearly show the sinusoidal surface of the holographic grating.

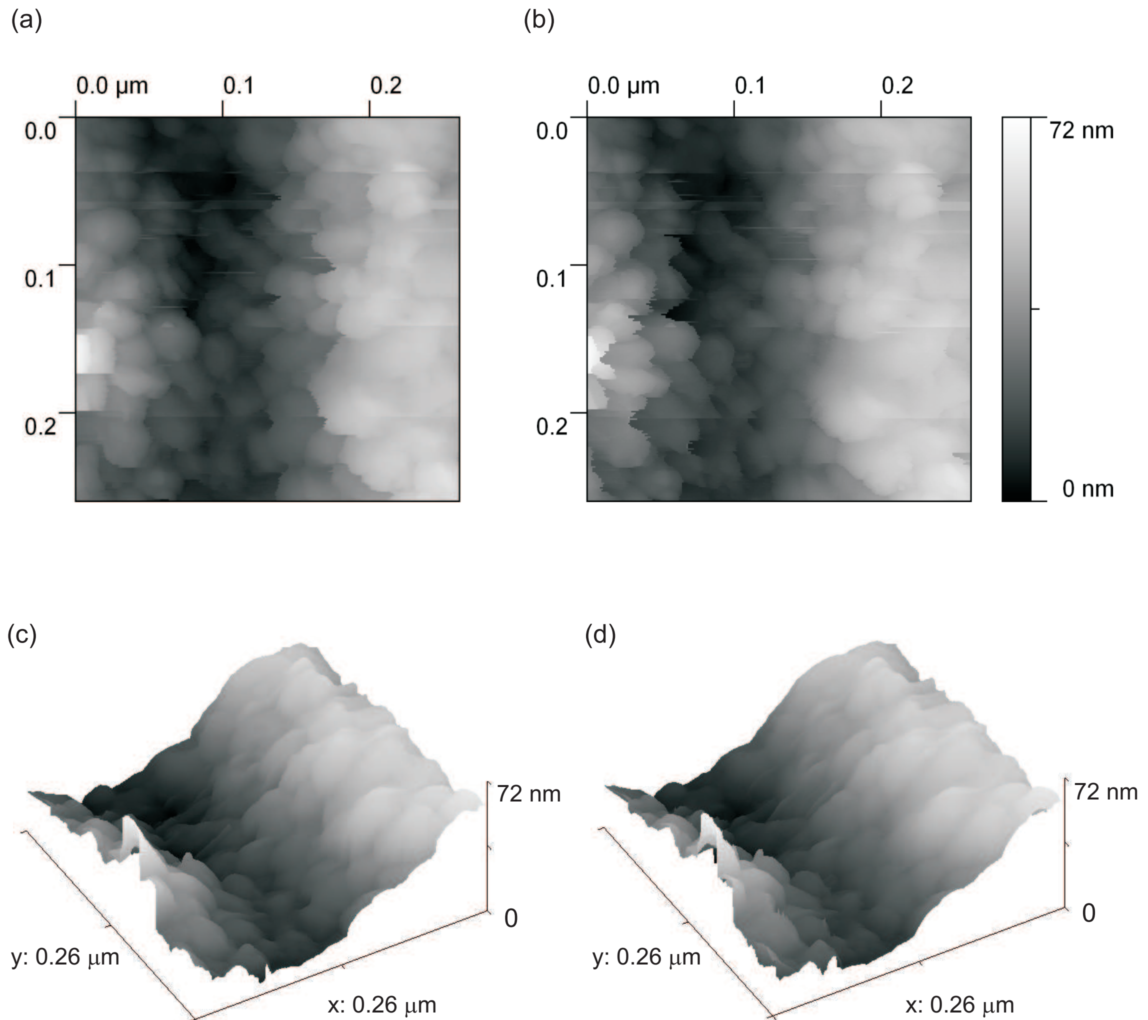

Figure 4.30: STM images of the holography grating surface for a scan area of about 260 x 260 nm^2. (a) Image recorded while scanning the tungsten tip to the right ($+x$ direction), (b) image recorded while scanning the tungsten tip to the left ($-x$ direction), (c) the corresponding three-dimensional image of the image in (a), and (d) the corresponding three-dimensional image of the image in (b).

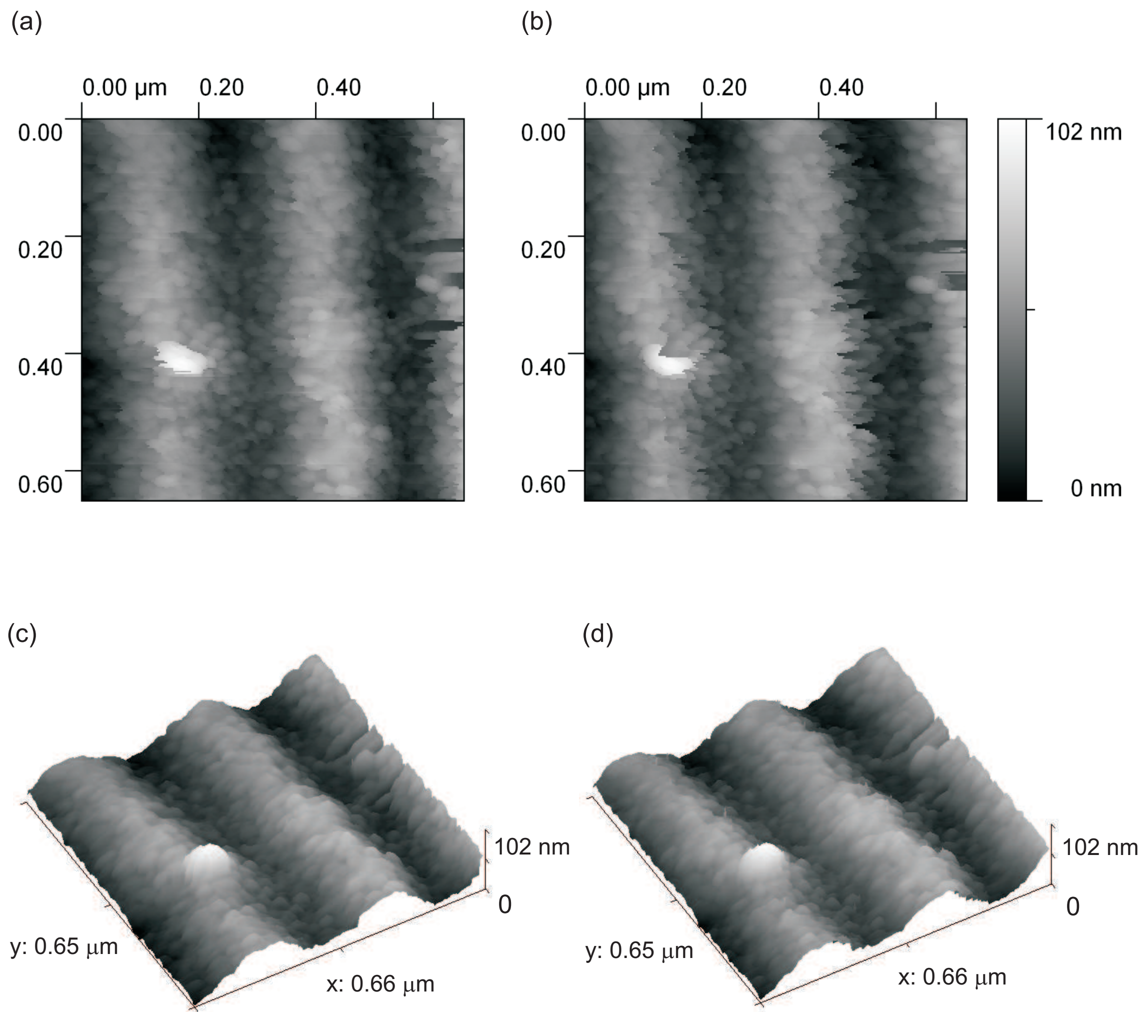

Figure 4.31: STM images of the holography grating surface for a scan area of about 660 x 660 nm^2. (a) Image recorded while scanning the tungsten tip to the right ($+x$ direction), (b) image recorded while scanning the tungsten tip to the left ($-x$ direction), (c) the corresponding three-dimensional image of the image in (a), and (d) the corresponding three-dimensional image of the image in (b).

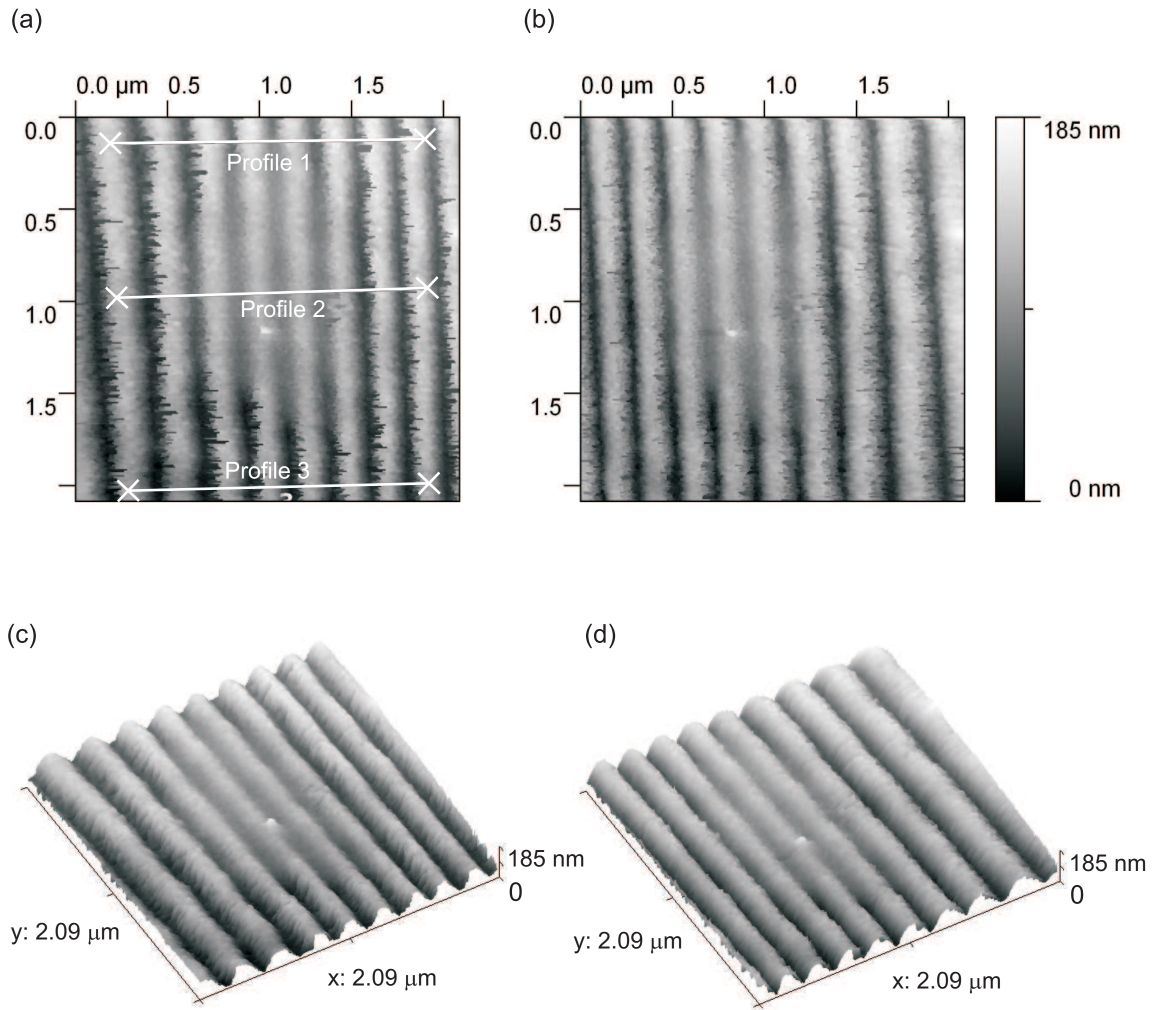

Figure 4.32: STM images of the holography grating surface for a scan area of about 2.09 x 2.09 μm^2. (a) Image recorded while scanning the tungsten tip to the right ($+x$ direction), (b) image recorded while scanning the tungsten tip to the left ($-x$ direction), (c) the corresponding three-dimensional image of the image in (a), and (d) the corresponding three-dimensional image of the image in (b).

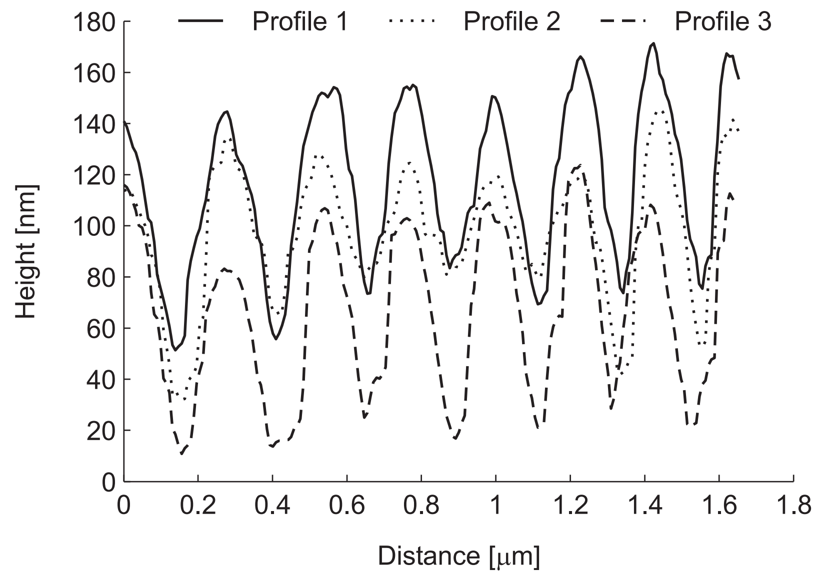

Figure 4.33: Profiles of the grating surface (refer to Fig. 4.32(a)).

4.6 Chapter Summary

Initial experiments indicate that the instrument is operating properly in STM mode with a resolution less than 2 Å in the direction normal to the sample surface. The vibration isolation analyses show that a single-stage vibration isolation system will be adequate for isolating the instrument from floor vibrations. Based on the analytical and experiment results, the length of the tip mounted on the end of a piezoelectric tube scanner can significantly amplify the lateral displacements of the tube. Thus, it is essential to calibrate the tube scanner. A simple technique using a preshaped driving signal minimizes the nonlinearity and the hysteresis of the tube scanner.

Chapter 5

Conclusions and Future Work

This dissertation emerges as the result of a concept to utilize a field-emitted electron beam from a CNT or a sharp tungsten tip to pattern nanoscale features on the surface of a metal. The following sections give the conclusions obtained from this research and suggest topics for future research.

5.1 Conclusions

In conclusion, this dissertation proved the hypothesis that states a precision instrument can enable the integration of direct-write nanolithography by a field-emitted electron beam with dimensional metrology by scanning tunneling microscopy. Furthermore, this instrument is not only for research into nanolithographic techniques using field-emitted electron beams, but also for charaterizing field emission of various field emitters from extremely small distances to distances of a few milimeters.

Also, from this research, it was learned that field emission from 1D nanostructures can be characterized as a function of the applied voltage and the separation distance at small separation distances. This was demonstrated using a technique that employs an apparatus to precisely adjust the separation with respect to a datum distance established between the tip of the emitter and an electron collector. It was found that field emission depends strongly on the separation distance and both the field amplification factor and turn-on voltage decrease as the separation distance decreases. The dependence of the field amplification factor on separation distance is well modeled by the modified Miller equation.

In addition, both a CNT field emitter and a sharp tungsten field emitter show that field emission currents on the order of a few hundred nanoamperes are easily obtained at separation distances ranging from sub-micrometer up to a few micrometers. These emission currents are sufficient for electron-beam lithography. The voltages needed to create sufficient electric fields for electron emission were found to be a few times lower when a CNT is attached to an etched tungsten tip.

For the piezoelectric linear motor, experimental results reveal that the motion characteristics of the linear motor are unlike any other motor. It was found that each individual step consists of a momentary reverse motion followed by a forward motion before completing a step. The step size is highly repeatable with a standard deviation of less than 1.2 nm, and the thermal stability is better than 40 nm/°C. For a light preload force, a simple analytical model shows good agreement with the experimental step size when the experimental threshold voltage is used.

A low thermal drift instrument was designed, constructed, and tested. Initial experiments indicate that the instrument operates properly in scanning tunneling microscope mode with a resolution of less than 2 Å in the direction normal to the sample surface. Based on the analytical and experiment results, the length of the tip mounted at the end of a piezoelectric tube scanner can significantly amplify the lateral displacements of the tube. Thus, it is essential to calibrate the tube scanner. The linearity of the scanner's motion can be improved with a simple technique that uses the preshaping of driving signal. From the vibration isolation analyses, a single-stage vibration isolation system will be sufficient for the instrument.

The major contributions of this dissertation are listed as follow:

1. the development of the key components of the instrument for future research into nanolithographic techniques using field-emitted electron beams;

2. the design of a piezoelectric linear motor that has a low thermal drift using symmetrical design and low coefficients of thermal expansion materials;

3. the experimental studies of the motion characteristics and the thermal stability of the linear piezoelectric motor;

4. a simple method for improving the linearity of piezoelectric actuators using the pre-shaping of driving signal;
5. a new method was developed for extracting the FN parameters that is an improvement over conventional extraction using slope and ordinate intercepts on FN plots; and
6. a technique was developed for characterizing the field emission from one-dimensional (1D) nanostructures at small separation distances.

5.2 Future Work

The instrument should have atomic resolution, but this has not been verified experimentally. This can be verified by obtaining an atomic image of a HOPG sample while operating the instrument in the STM mode. The thermal stability of the instrument needs to be measured. This can be accomplished rather easily by taking several STM images of a sample surface and comparing them for any thermal drift. The ability of the instrument to image a sample surface with a CNT tip is yet to be investigated.

This instrument requires a dedicated controller, a commercial SPM controller is an ideal candidate. It is recommended to calibrate the lateral motions of the piezoelectric tube scanner every time a tip is changed. This can be accomplished by scanning a standard calibration specimen (for the final calibration) that is dedicated for calibrating the piezoelectric tube scanner. Also, the simple method for improving the linearity of the tube scanner with a preshaped input waveform shall be implemented and further investigated.

The frequency response of the tunneling gap (tip-sample) and the dynamic characteristics of the instrument should be determined experimentally. This will help to optimize the performance of the instrument. The frequency response measurement of the tunneling gap is not trivial, one can apply a sweep signal from a dynamics signal analyzer to the z scanner while recording the variation in the tunneling current.

The model for calculating the threshold voltage and step size of the piezoelectric linear motor does not account for the moments generated by the shear-mode piezoelectric

actuators, and hence requires further study. The model shall improve if the moments are taken into consideration. A numerical model or simulation is highly recommended so that the interaction in each of the components can be accounted.

The electrical connectors of the loadable instrument require some revision. The connectors fit too tightly and this could create problem during the load-lock transfer of the instrument into the UHV chamber. Other alternatives should be investigated.

Bibliography

[1] V. V. Mitin, V. A. Kochelap, and M. A. Stroscio. *Introduction to Nanoelectronics*. Cambridge University Press, New York, 2008.

[2] S. A. Campbell. *The Science and Engineering of Microelectronic Fabrication.* Oxford University Press, New York, 2001.

[3] S. Franssila. *Introduction to Microfabrication*. John Wiley & Sons, Hoboken, New Jersey, 2004.

[4] R. R. Vallance, A. M. Rao, and M. P. Menguc. Processes for Nanomachining using Carbon Nanotubes. (US Patent No. 6,660,959), 9 December 2003.

[5] B. T. Wong and M. P. Menguc. *Thermal Transport for Applications in Nanomachining*. Berlin, Springer, 2008.

[6] B. T. Wong. *Thermal Heat Transport at the Nanoscale Level and Its Applications to Nano-Machining*. PhD thesis, University of Kentucky, 2006.

[7] J. A. Sanchez. *Electron Field-Emission from Carbon Nanotubes for Nanomachining Applications*. PhD thesis, University of Kentucky, 2008.

[8] G. Binnig, H. Rohrer, C. Gerber, and E. Weibel. Surface studies by scanning tunneling microscopy. *Physical Review Letters*, 49(1):57–61, July 1982.

[9] C. J. Chen. *Introduction to Scanning Tunneling Microscopy*. Oxford University Press, New York, 1993.

[10] G. Binnig, H. Rohrer, Ch. Gerber, and E. Weibel. Tunneling through a controllable vacuum gap. *Applied Physics Letters*, 40:178–180, 1982.

[11] R. Young, J. Ward, and F. Scire. Observation of metal-vacuum-metal tunneling, field emission, and the transition region. *Physical Review Letters*, 27:922–925, 1971.

[12] R. Young, J. Ward, and F. Scire. The topografiner: An instrument for measuring surface microtopography. *Review of Scientific Instruments*, 43(7):999–1011, July 1972.

[13] E. C. Teague. *Room temperature gold-vacuum-gold tunneling experiments*. PhD thesis, North Texas State University, 1978.

[14] C. Bai. *Scanning Tunneling Microscopy and Its Application*. Springer, New York, 2nd edition, 2000.

[15] D. A. Bonnell. *Scanning Tunneling Microscopy and Spectroscopy: Theory, Techniques, and Applications*. John Wiley & Sons, Hoboken, New Jersey, 1993.

[16] A. A. Tseng, A. Notargiacomo, and T. P. Chen. Nanofabrication by scanning probe microscope lithography: A review. *Journal of Vacuum Science and Technology B*, 23(3):877–894, 2005.

[17] M. A. McCord and R. F. W. Pease. Lift-off metallization using poly(methyl methcrylate) exposed with a scanning tunneling microscope. *Journal of Vacuum Science and Technology B*, 6(1):293–296, 1988.

[18] N. Li, T. Yoshinobu, and H. Iwasaki. Nanofabrication on Si oxide with scanning tunneling microscope: Mechanism of the low-energy electron-stimulated reaction. *Applied Physics Letters*, 74(11):1621–1623, March 1999.

[19] H. Iwasaki, T. Yoshinobu, and K. Sudoh. Nanolithography on SiO_2/Si with a scanning tunnelling microscope. *Nanotechnology*, 14:R55ŰR62, 2003.

[20] N. Ueda, N. Li K. Sudoh, T. Yoshinobu, and H. Iwasaki. Controllable nanopit formation on Si(001) with a scanning tunneling microscope. *Japanese Journal of Applied Physics*, 38:5236–5238, 1999.

[21] K. Sudoh and H. Iwasaki. Nanopit formation and manipulation of steps on Si(001) at high temperatures with a scanning tunneling microscope. *Japanese Journal of Applied Physics*, 39:4621–4623, 2000.

[22] S. Iijima. Helical microtubules of graphitic carbon. *Nature*, 354:56–58, 1991.

[23] W. A. deHeer, A. Chatelain, and D. Ugarte. A carbon field-emission electron source. *Science*, 270(5239):1179–1180, 1995.

[24] W. A. deHeer, W. S. Bacsa, A. Chatelain, T. Gerfin, R. Humphrey-Baker, L. Forro, and D. Ugarte. Aligned carbon nanotube films: Production and optical and electronic properties. *Science*, 268(5212):845–847, 1995.

[25] A. G. Rinzler, J. H. Hafner, P. Nikolaev, P. Nordlander, D. T. Colbert, R. E. Smalley, L. Lou, S. G. Kim, and D. Tomanek. Unraveling nanotubes: Field emission from an atomic wire. *Science*, 269(5230):1550–1553, September 1995.

[26] A. G. Mamalis, L. O. G. Vogtlander, and A. Markopoulos. Nanotechnology and nanostructured materials: trends in carbon nanotubes. *Precision Engineering*, 28:16–30, 2004.

[27] M. J. Fransen. *Towards high-brightness, monochromatic electron sources*. 1999.

[28] W. Zhu, C. Bower, O. Zhou, G. Kochanski, and S. Jin. Large current density from carbon nanotube field emitters. *Applied Physics Letters*, 75(6):873–875, 1999.

[29] A. M. Rao, D. Jacques, R. C. Haddon, W. Zhu, C. Bower, and S. Jin. In situ-grown carbon nanotube array with excellent field emission characteristics. *Applied Physics Letters*, 76(25):3813–3815, June 2000.

[30] Y. C. Choi, Y. M. Shin, D.J. Bae, S.C. Lim, Y.H. Lee, and B.S. Lee. Patterned growth and field emission properties of vertically aligned carbon nanotubes. *Diamond and Related Materials*, 10:1457–1464, 2001.

[31] P. G. Collins and A. Zettl. A simple and robust electron beam source from carbon nanotubes. *Applied Physics Letters*, 69(13):1969–1971, 1996.

[32] K. B. K. Teo, M. Chhowalla, G. A. J. Amaratunga, W. I. Milne, P. Legagneux, G. Pirio, L. Gangloff, D. Pribat, V. Semet, V. T. Binh, W. H. Bruenger, H. Hanssen J. Eichholz, D. Friedrich, S. B. Lee, D. G. Hasko, and H. Ahmed. Fabrication and electrical characteristics of carbon nanotube-based microcathodes for use in a parallel electron-beam lithography system. *Journal of Vacuum Science and Technology B*, 21(2):693–697, 2003.

[33] Y. Saito, S. Uemura, and K. Hamaguchi. Cathode ray tube lighting elements with carbon nanotube field emitters. *Japanese Journal of Applied Physics*, 37:L346–L348, 1998.

[34] Q. H. Wang, A. A. Setlur, J. M. Lauerhaas, J. Y. Dai, E. W. Seelig, and R. P. H. Chang. A nanotube-based field-emission flat panel display. *Applied Physics Letters*, 72(22):2912–2913, 1998.

[35] J. M. Bonard, J. P. Salvetat, T. Stockli, L. Forro, and A. Chatelain. Field emission from carbon nanotubes: perspectives for applications and clues to the emission mechanism. *Applied Physics A*, 69(3):245–254, September 1999.

[36] N. de Jonge and N. J. van Druten. Field emission from individual multiwalled carbon nanotubes prepared in an electron microscope. *Ultramicroscopy*, 95:85–91, 2003.

[37] P. N. Minh, L. T. T. Tuyen, T. Ono, H. Miyashita, Y. Suzuki, H. Mimura, and M. Esahi. Selective growth of carbon nanotubes on Si microfabricated tips and

application for electron field emitters. *Journal of Vacuum Science and Technology B*, 21(4):1705–1709, 2003.

[38] D. Lovall, M. Buss, E. Graugnard, R. P. Andres, and R. Reifenberger. Electron emission and structural characterization of a rope of single-walled carbon nanotubes. *Physical Review B*, 61(8):5683–5691, 2000.

[39] M. J. Fransen, Th. L. van Rooy, and P. Kruit. Field emission energy distributions from individual multiwalled carbon nanotubes. *Applied Surface Science*, 146:312–327, 1999.

[40] Y. Saito, K. Hamaguchi, S. Uemura, K. Uchida, Y. Tasaka, F. Ikazaki, M. Yumura, A. Kasuya, and Y. Nishina. Field emission from multi-walled carbon nanotubes and its application to electron tubes. *Applied Physics A: Materials Science & Processing*, 67(1):95–100, 1998.

[41] K. A. Dean and B. R. Chalamala. Field emission microscopy of carbon nanotube caps. *Journal of Applied Physics*, 85(7):3832–3836, 1999.

[42] C. Jin, J. Wang, M. Wang, J. Su, and L.-M. Peng. In-situ studies of electron field emission of single carbon nanotubes inside the tem. *Carbon*, 43(5):1026–1031, 2005.

[43] W. I. Milne, K. B. K. Teo, M. Chhowalla, G. A. J. Amaratunga, S. B. Lee, D. G. Hasko, H. Ahmed, O. Groening, P. Legagneux, L. Gangloff, J. P. Schnell, G. Pirio, D. Pribat, M. Castignolles, A. Loiseau, V. Semet, and V. T. Binh. Electrical

and field emission investigation of individual carbon nanotubes from plasma enhanced chemical vapour deposition. *Diamond and Related Materials*, 12:422–428, 2003.

[44] J. M. Bonard, K. A. Dean, B. F. Coll, and C. Klinke. Field emission of indivudual carbon nanotubes in the scanning electron microscope. *Physical Review Letters*, 89(19):197602, November 2002.

[45] J. C. She, N. S. Xu, S. Z. Deng, Jun Chen, H. Bishop, S. E. Huq, L. Wang, D. Y. Zhong, and E. G. Wang. Vacuum breakdown of carbon-nanotube field emitters on a silicon tip. *Applied Physics Letters*, 83:2671–2673, 2003.

[46] H. Li, J. Li, and C. Gu. Local field emission from individual vertical carbon nanofibers grown on tungsten filament. *Carbon*, 43(4):849–853, 2005.

[47] H. S. Sim, S. P. Lau, L. K. Ang, G. F. You, M. Tanemura, K. Yamaguchi, M. Zamri, and M. Yusop. Field emission from a single carbon nanofiber at sub 100 nm gap. *Applied Physics Letters*, 93(2):023131, July 2008.

[48] D. G. Walker, W. Zhang, and T. S. Fisher. Simulation of field-emitted electron trajectories and transport from carbon nanotubes. *Journal of Vacuum Science and Technology B*, 22(3):1101–1107, 2004.

[49] H. M. Rosenberg. *The Solid State*. Clarendon Press, Oxford, 2nd edition, 1978.

[50] T. S. Hutchison and D. C. Baird. *The Physics of Engineering Solids*. John Wiley and Sons, Inc., New York and London, 1967.

[51] R. Gomer. *Field Emission and Field Ionization*. American Institute of Physics, New York, 1993.

[52] D. R. Lide. *CRC Handbook of Chemistry and Physics*. CRC Press, 72nd edition, 1991-1992.

[53] A. L. Hughes and L. A. DuBridge. *Photoelectric Phenomena*. McGraw-Hill, New York, 1932.

[54] E. L. Murphy and R. H. Good. Thermionic emission, field emission, and the transition region. *Physical Review*, 102(6):1464–1473, June 1956.

[55] J. Paulini, T. Klein, and G. Simon. Thermo-field emission and the Nottingtham effect. *Journal of Physics D: Applied Physics*, 26:1310–1315, 1993.

[56] S. C. Miller and R. H. Good. A WKB-type approximation to the Schrodinger equation. *Physical Review*, 91(1):174–179, 1953.

[57] G. A. Korn and T. M. Korn. *Mathematical Handbook For Scientists and Engineers*. Dover Publications, Inc., Mineola, New York, 1968.

[58] R. H. Fowler and E. A. Guggenheim. *Statistical Thermodynamics*. Cambridge University Press, New York, 1952.

[59] A. B. El-Kareh, J. C. Wolfe, and J. E. Wolfe. Contribution to the general analysis of field emission. *Journal of Applied Physics*, 48(11):4749–4753, 1977.

[60] R. D. Young. Theoretical total-energy distribution of field-emitted electrons. *Physical Review*, 113(1):110–114, 1959.

[61] S. G. Christov. General theory of electron emission from metals. *Physica Status Solidi*, 17(1):11–26, 1966.

[62] R. H. Fowler and L. W. Nordheim. Electron emission in intense electric fields. *Proceedings of the Royal Society of London A*, 119(781):173–181, 1928.

[63] L. W. Nordheim. The effect of the image forces on emission and reflection of electrons by metals. *Proceedings of the Royal Society of London A*, 121:626–639, 1928.

[64] R. E. Burgess, H. Kroemer, and J. M. Houston. Corrected values of Fowler-Nordheim field emission function $v(y)$ and $s(y)$. *Physical Review*, 90(4):515, May 1953.

[65] P. W. Hawkes and E. Kasper. *Principle of Electron Optics II: Applied Geometrical Optics*. Academic, London, 1996.

[66] R. Gao, Z. Pan, and Z. L. Wang. Work function at the tips of multiwalled carbon nanotubes. *Applied Physics Letters*, 78(12):1757–1759, March 2001.

[67] E. W. Muller. Field emission. *Annual Review of Physical Chemistry*, 18:35–56, Octocber 1967.

[68] K. F. Hii, R. R. Vallance, S. B. Chikkamaranahalli, M. P. Menguc, and A. M. Rao. Characterizing field emission from individual carbon nanotubes at small distances. *Journal of Vacuum Science and Technology B*, 24(3):1081–1087, May/June 2006.

[69] D. Nicolaescu. Physical basis for applying the Fowler-Nordheim $J - E$ relationship to experimental $I - V$ data. *Journal of Vacuum Science and Technology B*, 11(2):392–395, 1993.

[70] K. L. Jensen and E. G. Zaidman. Field emission from an elliptical boss: Exact and approximate forms for area factors and currents. *Journal of Vacuum Science and Technology B*, 12(2):776–780, 1994.

[71] K. L. Jensen and E. G. Zaidman. Analytic expressions for emission characteristics as a function of experimental parameters in sharp field emitter devices. *Journal of Vacuum Science and Technology B*, 13(2):511–515, 1995.

[72] K. L. Jensen and E. G. Zaidman. Analytic expressions for emission in sharp field emitter diodes. *Journal of Applied Physics*, 77(7):3569–3571, 1995.

[73] L. Marton. *Advances in Electronics and Electron Physics*. Academic Press, New York, 1956.

[74] H. C. Miller. Influence of gap length on the field factor β of an electrode projection (whisker). *Journal of Applied Physics*, 55(1):158–161, January 1984.

[75] H. C. Miller. Change in field intensification factor β of an electrode projection (whisker) at short gap lengths. *Journal of Applied Physics*, 38(11):4501–4504, October 1967.

[76] C. J. Edgcombe and U. Valdre. Microscopy and computational modelling to elucidate the enhancement factor for field electron emitters. *Journal of Miscroscopy*, 203:188–194, February 2001.

[77] R. G. Forbes. Field emission: New theory for the derivation of emission area from a Fowler-Nordheim plot. *Journal of Vacuum Science and Technology B*, 17(2):526–533, 1999.

[78] C. A. Spindt, I. Brodie, L. Humphrey, and E. R. Westerberg. Physical properties of thin-film field emission cathodes with molybdenum cones. *Journal of Applied Physics*, 47(12):5248–5263, December 1976.

[79] R. G. Forbes and K. L. Jensen. New results in the theory of Fowler-Nordheim plots and the modelling of hemi-ellipsoidal emitters. *Ultramicroscopy*, 89:17–22, October 2001.

[80] C. A. Trinkle. Fabrication of nanotube-tipped tools and flexural bearing displacement system for field-emission nanomachining. Master's thesis, University of Kentucky, 2003.

[81] S. S. Wong, A. T. Woolley, E. Joselevich, C. L. Cheung, and C. M. Lieber. Covalently-functionalized single-walled carbon nanotube probe tips for chemical force microscopy. *Journal of the American Chemical Society*, 120(33):8557–8558, 1998.

[82] H. J. Dai, N. Franklin, and J. Han. Exploiting the properties of carbon nanotubes for nanolithography. *Applied Physics Letters*, 73(11):1508–1510, September 1998.

[83] P. J. de Pablo, E. Graugnard, B. Walsh, R. P. Andres, S. Datta, and R. Reifenberger. A simple, reliable technique for making electrical contact to multiwalled carbon nanotubes. *Applied Physics Letters*, 74(2):323–325, January 1999.

[84] C. J. Edgcombe and N. de Jonge. Properties of a field emitter deduced from curvature of its Fowler-Nordheim plot. *Journal of Vacuum Science and Technology B*, 24(2):869–873, 2006.

[85] P. Kichambare, K. F. Hii, R. R. Vallance, B. Sadanadan, A. M. Rao, K. Javed, and M. P. Menguc. Growth of tungsten oxide nanorods with carbon caps. *Journal of Nanoscience and Nanotechnology*, 6(2):536–540, February 2006.

[86] K. A Dean and B. R. Chalamala. Experimental studies of the cap structure of single-walled carbon nanotubes. *Journal of Vacuum Science and Technology B*, 21(2):868–871, 2003.

[87] S. T. Smith. *Flexures: Elements of Elastic Mechanisms*. Taylor & Francis, London, 2000.

[88] C. J. Morgan, R. R. Vallance, and E. R. Marsh. Micro machining glass with polycrystalline diamond tools shaped by micro electro discharge machining. *Journal of Micromechanics and Microengineering*, 14(12):1687–1692, December 2004.

[89] K. A. Dean and B. R. Chalamala. Current saturation mechanisms in carbon nanotube field emitters. *Applied Physics Letters*, 76(3):375–377, January 2000.

[90] J. W. Luginsland, A. Valfells, and Y. Y. Lau. Effects of a series resistor on electron emission from a field emitter. *Applied Physics Letters*, 69(18):2770–2772, October 1996.

[91] J. M. Bonard, C. Klinke, K. A. Dean, and B. F. Coll. Degradation and failure of carbon nanotube field emitters. *Physical Review B*, 67:115406, 2003.

[92] R. T. Olson and J. A. Panitz. An instrument for investigating high electric field phenomena at small electrode separations. *Review of Scientific Instruments*, 69(5):2067–2071, May 1998.

[93] W. S. Boyle, P. Kisliuk, and L. H. Germer. Electrical breakdown in high vacuum. *Journal of Applied Physics*, 26(6):720–725, June 1953.

[94] G. C. Kokkorakis, J. A. Roumeliotis, and J. P. Xanthakis. Enhancement factor of open thick-wall carbon nanotubes. *Journal of Applied Physics*, 95(3):1468–1472, February 2004.

[95] D. W. Tuggle, J. Jiao, and L. F. Dong. Field emission current fluctuations from isolated carbon nanotubes. *Surface and Interface Analysis*, 36:489–492, 2004.

[96] A. Roth. *Vacuum Technology*. North-Holland, Amsterdam, 1976.

[97] K. A. Dean, T. P. Burgin, and B. R. Chalamala. Evaporation of carbon nanotubes during electron field emission. *Applied Physics Letters*, 79(12):1873–1875, September 2001.

[98] J. A. Sanchez, M. P. Menguc, K. F. Hii, and R. R. Vallance. Heat transfer within carbon nanotubes during electron field emission. *Journal of Thermophysics and Heat Transfer*, 22(2):281–289, 2008.

[99] M. Ge and K. Sattler. Vapor-condensation generation and stm analysis of fullerene tubes. *Science*, 260(5107):515–518, April 1993.

[100] A. H. R. Palser. Interlayer interactions in graphite and carbon nanotubes. *Physical Chemistry Chemical Physics*, 1:4459–4464, 1999.

[101] W. P. Mason. Piezoelectricity, its history and applications. *J. of Acoustical Society of America*, 70(6), 1981.

[102] M. D. Bryant and R. B. Reeves. Precise positioning problems using piezo-electric actuators with force transmission through mechanical contact. *Precision Engineering*, 6(3):129–134, July 1984.

[103] Y. Okazaki. A micro-positioning tool post using a piezoelectric actuator for diamond turning machines. *Precision Engineering*, 12(3):151–156, July 1990.

[104] T. G. King, M. E. Preston, B. J. M. Murphy, and D. S. Cannell. Piezoelectric ceramic actuators: A review of machinery applications. *Precision Engineering*, 12(3):131–136, July 1990.

[105] T. A. Dow, M. H. Miller, and P. J. Falter. Application of a fast tool servo for diamond turning of nonrotationally symmetric surfaces. *Precision Engineering*, 13(4):243–250, October 1991.

[106] P. Langenbeck. Ultrafine infeed control. *Precision Engineering*, 14(1):43–46, January 1992.

[107] C.-W. Lee and S.-W. Kim. An ultraprecision stage for alignment of wafers in advanced microlithography. *Precision Engineering*, 21(2-3):113–122, September-December 1997.

[108] W. Gao, R. J. Hocken, J. A. Patten, J. Lovingood, and D. A. Lucca. Construction and testing of a nanomachining instrument. *Precision Engineering*, 24(4):320–328, October 2000.

[109] A. Woronko, J. Huang, and Y. Altintas. Piezoelectric tool actuator for precision machining on conventional cnc turning centers. *Precision Engineering*, 27(4):335–345, October 2003.

[110] D. W. Pohl. Dynamic piezoeletric translation devices. *Review of Scientific Instruments*, 58(1):54–57, January 1987.

[111] Ch. Renner, Ph. Niedermann, A.D. Kent, and O. Fischer. A vertical piezoelectric inertial slider. *Review of Scientific Instruments*, 61(3):965–967, 1990.

[112] Inchworm is a registered trademark of Burleigh Inst. Inc., Fisher, NY 14453.

[113] S. H. Pan. Piezoelectric Motor, International Patent Publication Number WO 93/19494 (International Bureau, World Intellectual Property Organization), 30 September 1993.

[114] A. K. Gupta and K.-W. Ng. Compact coarse approach mechanism dor scanning tunneling microscope. *Review of Scientific Instruments*, 72(9):3552–3555, 2001.

[115] G. Mariotto, M. D'Angelo, and I.V. Shvets. Dynamic behavior of a piezowalker, inertial and frictional configirations. *Review of Scientific Instruments*, 70(9):3651–3655, 1999.

[116] K. Kwon, N. Cho, and W. Jang. The design and characterization of a piezo-driven inchworm linear motor with a reduction-lever mechanism. *JSME International Journal Series C*, 47(3):803–811, 2004.

[117] S. H. Pan, E. W. Hudson, and J. C. Davis. ^{3}He refrigerator based very low temperature scanning tunneling microscope. *Review of Scientific Instruments*, 70(2):1459–1463, 1999.

[118] G. Binnig and D.P.E. Smith. Single-tube three-dimensional scanner for scanning tunneling microscopy. *Review of Scientific Instruments*, 57(8):1688–1689, August 1986.

[119] F. Mugele, Ch. Kloos, P. Leiderer, and R. Muller. A simple, ultrahigh vacuum compatible scanning tunneling microscope for use at variable temperatures. *Review of Scientific Instruments*, 67:2557–2559, 1996.

[120] Picomotor is a registered trademark of New Focus™, a division of Bookham, 2584 Junction Avenue, San Jose, CA 95134, USA.

[121] Chr. Wittneven, R. Dombrowski, S. H. Pan, and R. Wiesendanger. A low-temperature ultrahigh-vacuum scanning tunneling microscope with rotatable magnetic field. *Review of Scientific Instruments*, 68(10):3806–3810, 1997.

[122] R. Euler, U. Memmert, and U. Hartmann. Fiber interferometer-based variable temperature scanning force microscope. *Review of Scientific Instruments*, 68(4):1776–1778, 1997.

[123] H. Zhang, U. Memmert, R. Houbertz, and U. Hartmann. A variable-temperature ultrahigh vacuum scanning tunneling microscope. *Review of Scientific Instruments*, 72(6):2613–2617, 2001.

[124] G. Mariotto, M. D'Angelo, J. Kresnin, and I.V. Shvets. Study of the dynamic behaviour of a piezo-walker. *Applied Surface Science*, 144-145:530–533, 1999.

[125] D. L. Blanding. *Exact Constraint: Machine Design Using Kinematic Principles*. New York: ASME Press, 1999.

[126] A. H. Burr and J. B. Cheatham. *Mechanical Analysis and Design*. Prentice Hall, Englewood Cliffs, NJ 07632, 2nd edition, 1995.

[127] E. R. Hnatek. *Applications of Linear Integrated Circuits*. Wiley-Interscience, 1975.

[128] R. F. Graf and W. Sheets. *Encyclopedia of Electronic Circuits*, volume 7. McGraw-Hill, New York, NY 10011, 1999.

[129] M. S. Colclough. A fast high-voltage amplifier for driving piezoelectric positioners. *Review of Scientific Instruments*, 71(11):4323–4324, November 2000.

[130] S. Koganezawa and T. Hara. Development of shear-mode piezoelectric microactuator for precise head positioning. *FUJITSU Scientific & Technical Journal*, 37(2):212–219, December 2001.

[131] A. E. Holman, P. M. L. O. Scholte, W. Chr. Heerens, and F. Tuinstra. Analysis of piezo actuators in translation constructions. *Review of Scientific Instruments*, 66(5):3208–3215, May 1995.

[132] L. E. C. van de Leemput, P. H. H. Rongen, B. H. Timmerman, and H. van Kempen. Calibration and characterization of piezoelectric elements as used in scanning tunneling microscopy. *Review of Scientific Instruments*, 62(4):989–992, April 1991.

[133] J. Akila and S. S. Wadhwa. Correction for nonlinear behavior of piezoelectric tube scanners used in scanning tunneling and atomic force microscopy. *Review of Scientific Instruments*, 66(3):2517–2519, March 1995.

[134] Commercially available from various manufacturers such as Physik Instrumente, Park Systems, and Wye Creek Instruments.

[135] M. Gehrtz, H. Strecker, and H. Grimm. Scanning tunneling microscopy of machined surfaces. *Journal of Vacuum Science and Technology A*, 6(2):432–435, March 1998.

[136] S. Okayama, M. Komuro, W. Mizutani, H. Tokumoto, M. Okano, K. Shimizu, Y. Kobayashi, F. Matsumoto, S. Wakiyama, M. Shigeno, F. Sakai, S. Fujiwara, O. Kitamura, M. Ono, and K. Kajimura. Observation of microfabricated patterns by scanning tunneling microscopy. *Journal of Vacuum Science and Technology A*, 6(2):440–444, March 1988.

[137] M. Locatelli and G. Lamboley. Easy method to characterize a piezoelectric ceramic tube as a displacer. *Review of Scientific Instruments*, 59(4):661–663, April 1988.

[138] T. Tiedje and A. Brown. Performance limits for the scanning tunneling microscope. *Journal of Applied Physics*, 68(2):649–654, July 1990.

[139] C. J. Chen. Electromechanical deflections of piezoelectric tubes with quartered electrodes. *Applied Physics Letters*, 60(1):132–134, January 1992.

[140] C. Wei, H. Zhang, L. Tao, W. Li, and H. Shi. A circular arc bending model of piezoelectric tube scanners. *Review of Scientific Instruments*, 67(6):2848–2852, June 1996.

[141] S. Yang and W. Huang. Three-dimensional displacements of a piezoelectric tube scanner. *Review of Scientific Instruments*, 69(1):226–229, January 1998.

[142] R. G. Carr. Finite element analysis of PZT tube scanner motion for scanning tunneling microscopy. *Journal of Microscopy*, 152(2):379–385, November 1988.

[143] S. Hudlet, M. S. Jean, D. Royer, J. Berger, and C. Guthmann. In situ measurement of large piezoelectric displacements in resonant atomic force microscopy. *Review of Scientific Instruments*, 66(4):2848–2852, April 1995.

[144] C. Wei, H. Zhang, L. Tao, W. Li, and H. Shi. Compensation method based on formularizing hysteresis of piezoelectric tube scanners. *Review of Scientific Instruments*, 67(10):3594–3598, October 1996.

[145] K. G. Vandervoort, R. K. Zasadzinskiand G. G. Galicia, and G. W. Crabtree. Full temperature calibration from 4 to 300 K of the voltage response of piezoelectric tube scanner PZT-5A for use in scanning tunneling microscopes. *Review of Scientific Instruments*, 64(4):896–899, April 1993.

[146] K. G. Vandervoort, R. K. Zasadzinskiand G. G. Galicia, and G. W. Crabtree. Further measurements of the temperature dependence of the voltage response of piezoelectric tube scanner PZT-5A for use in scanning tunneling microscopes. *Review of Scientific Instruments*, 65(12):3862–3863, December 1994.

[147] M. E. Taylor. Dynamics of piezoelectric tube scanners for scanning probe microscopy. *Review of Scientific Instruments*, 64(1):154–158, January 1993.

[148] L. Tao and J. Maps. Simple determination of the frequency response of piezoelectric tubes. *Review of Scientific Instruments*, 64(5):1367–1368, May 1993.

[149] D. Croft and D. McAllisterand S. Devasia. High-speed scanning of piezoprobes for nano-fabrication. *Journal of Manufacturing Science and Engineering*, 120:617–622, August 1998.

[150] B. Jaffe, W. R. Cook, and H. Jaffe. *Piezoelectric Ceramics*. Academic Press, New York, 1971.

[151] C. V. Newcomb and I. Flinn. Improving the lineaity of piezoelectric ceramics actuators. *Electronics Letters*, 18(11):442–443, May 1982.

[152] J. A. Main, E. Garcia, and D. V. Newton. Precision position control of piezoelectric actuators using charge feedback. *Journal of Guidance, Control, and Dynamics*, 18(5):1068–1073, 1995.

[153] A. H. Slocum. *Precision Machine Design*. Society of Manufacturing Engineers, Dearborn, Michigan, 1992.

[154] M. Okano, K. Kajimura, S. Wakiyama, F. Sakai, W. Mizutani, , and M. Ono. Vibration isolation for scanning tunneling microscopy. *Journal of Vacuum Science and Technology A*, 5(6):3313–3320, 1987.

[155] W. T. Thomson and M. D. Dahleh. *Theory of Vibration with Applications*. Prentice Hall, Upper Saddle River, New Jersey, 1998.

[156] J. P. Den Hartog. *Mechanical Vibrations*. Dover Publications, Inc, New York, 1985.

VITA

King-Fu Hii was born July 9, 1976 in Sibu, Sarawak, Malaysia. He received a B.S. in Mechanical Engineering with minor in mathematics from the University of Kentucky in 1999 and a M.S. in Mechanical Engineering from the University of Kentucky in 2002. King-Fu has attained several honors throught his academic career, including: Tau Beta Pi Engineering Honor Society and the Golden Key Honor Society. King-Fu is a member of the American Society of Mechanical Engineers and the American Society of Precision Engineering.

Publications:

K. -F. Hii , R. R. Vallance, R. D. Grejda, and E. R. Marsh, "Error Motion of a Kinematic Spindle", *Precision Engineering*, 28(2), 204-217, 2004.

K. -F. Hii, R. R. Vallance, S. B. Chickkaramanahalli, M.P. Menguc, and A. Rao, "Characterizing Field Emission from Individual Carbon Nanotubes at Small Distances", *Journal of Vacuum Science and Technology B*, 24(3), 1081-1087, 2006.

P. Kichambare, K. -F. Hii, R. R. Vallance, B. Sadanadan, A. M. Rao, K. Javed, and M. P. Menguc, "Growth of Tungsten Oxide Nanorods with Carbon Caps", *Journal of Nanoscience and Nanotechnology*, 6(12), 536-540, 2006.

J. A. Sanchez, M. P. Menguc, K. -F. Hii, and R. R. Vallance, "Heat Transfer within Carbon Nanotubes during Electron Field Emission", *Journal of Thermophysics and Heat Transfer*, 22(2), 281-289, 2008.

K. -F. Hii, R. R. Vallance, and M. P. Menguc, "Design, Operation, and Motion Characteristics of a Piezoelectric Linear Motor", *Precision Engineering*. (in progress)

K. -F. Hii, R. R. Vallance, and M. P. Menguc, "A Thermally Stable and Ultra-High-Vacuum Compatible Translation Piezoelectric Linear Motor for Scanning Probe Microscopy", *Review of Scientific Instruments*. (in progress)

King-Fu Hii